

UNIVERSITY OF TWENTE.

MASTER THESIS

Applied Mathematics & Applied Physics
Applied Analysis & Mathematical Physics
Physics of Fluids

On Faraday Waves and Jets

March 24, 2012

Author:
I.A.M. van der Kroon

Graduation Committee:
Prof. dr. S.A. van Gils
Prof. dr. E. van Groesen
Prof. dr. D. Lohse
Dr. D. van der Meer
Prof. dr. ir. H.J.W. Zandvliet

Abstract

This thesis is an overview of our investigation of Faraday waves and jets on free surfaces. Faraday waves are standing waves generated by a parametric oscillation. We will consider the parametric oscillation of gravity in this study.

A cylinder containing the fluid of interest is mounted on a vibration device which shakes the entire setup vertically. In this way the effective gravity is modified which generates period-doubled standing waves in the fluid. Continuous excitation leads to very large amplitudes. The surface of the fluid becomes unstable and collapses symmetrically. This singularity, caused by inertial focusing, leads to jet formation.

High speed imaging techniques are used to capture the surface profiles of the standing waves, cavities and jets. The maximum tip velocity found in our setup was 22ms^{-1} .

The dynamics of the bulk flow, the boundary layers and the contact line are treated separately. Their contributions are combined in a single model by considering the mechanical energy.

Contents

Abstract	4
1 Introduction	7
1.1 Background and motivation	7
1.2 Faraday waves	8
1.3 Research questions	9
2 Theoretical Aspects	11
2.1 Parametric oscillations	12
2.1.1 Mathieu function	12
2.1.2 Solutions	13
2.1.3 Fourier series	15
2.1.4 Friction	17
2.1.5 The Sturm-Liouville Operator	18
2.1.6 Faraday waves	19
2.2 Gravity Waves	20
2.2.1 The Navier Stokes Equation	20
2.2.2 Surface dynamics	22
2.2.3 Boundary conditions	22
2.2.4 Equations of Motion	25
2.2.5 Irrotational Flow	26
2.2.6 Airy theory	30
2.2.7 Boundary layers	31
2.2.8 Meniscus Waves	34
2.2.9 Wetting effects	37
2.3 Cavities and Jets	43
2.3.1 Introduction	44
2.3.2 Similarity solutions	45
2.3.3 Other solutions	46
2.3.4 The jetting state	47
2.3.5 Surface irregularities	48
3 Experimental Aspects	49
3.1 Setup	49
3.1.1 Components	49
3.1.2 Faraday excitation	50
3.2 High speed imaging	53
3.3 Automation	55

3.4	Surface tension measurements	56
4	Analysis and Results	59
4.1	Qualitative observations	59
4.2	Solid-body state	61
4.2.1	Meniscus waves in water	61
4.2.2	Meniscus waves in sunflower oil	63
4.2.3	Transition to the Faraday waves	64
4.3	Standing wave state	66
4.3.1	Mathieu function	68
4.3.2	Parameter sweeps	69
4.3.3	Transitions and Hysteresis	74
4.4	Dissipation	78
4.4.1	Surface tension measurements	78
4.4.2	Flow dissipation	79
4.4.3	Dissipation experiments	80
4.4.4	Wetting effects	82
4.5	Cavities and Jets	83
4.5.1	Transitions to jets	83
4.5.2	Morphology of collapsing cavities	85
4.5.3	Tip velocity	86
5	Numerical Aspects	95
5.1	Introduction	95
5.2	Transformations	96
5.2.1	Implementation	96
5.2.2	Testing	98
5.3	A simple system	99
5.4	Coordinate transformations	100
6	Conclusion	103
6.1	Discussion	103
6.2	Conclusion	104
6.3	Recommendations	105
	Acknowledgments	109

Chapter 1

Introduction

1.1 Background and motivation

When being in an elevator, a fairground attraction or an airplane one has the experience as if gravity is not constant anymore. While the origin of this feeling is of course some non-gravitational force acting on the human body leading to a different acceleration, the sensation of a modified gravity is obvious. It is so natural that all such loads are expressed as a factor times the gravitational constant, denoted as g-forces. For instance centrifugal forces, the acceleration of a car or the shock resistance of wrist watches are measured in this unit. All contributions can be added as vectors to find the effective gravity experienced.

A small vertical vibration seems to be a less exciting version of this concept but when applied long enough the effects can be devastating. Heavy earthquakes only reach one to two times the gravitational constant [88] which suggests the ongoing trembling of the earth's surface is critical for the result. Other examples of systems that change the total acceleration continuously are found in transportation, industrial and household machinery, children's swings and music instruments. To investigate the nature of these phenomena, one could design a system that vibrates along the direction of gravity such that the direction of the effective gravity does not change. In this study we use the potential strength of oscillating gravity as an external exciter for waves on liquid surfaces.

On large scales, like the ocean, waves are mostly generated by wind, the moon, thermal convection, ship movement, etc. However, wave traveling is generally of a diverging nature. The inertia they carry is distributed and exceptional effects are rare. Very high waves, known as freak waves like the New Year's wave [85] are legendary. In practice wave breaking only occurs at beaches, when the sloping bottom causes most waves to grow in size while slowing down. The critical amplitude for wave breaking is usually in the order of its wavelength. Another effective way of creating breaking waves is with the following experiment. A solid container filled with the liquid of interest is mounted on a vibration system which is a driver for surface waves. Considering the long build-up time for our excitation mechanism we need to retain the inertia of the fluid in order to investigate high amplitudes. Standing waves a particular suitable for this pur-

pose and they are generated for favorable parameters, which we will discuss. The largest differences with an open domain are the effects of reflection and dissipation near the edges. Movement along the walls and wetting dynamics may be involved as well. This complicates the investigation of the system significantly. When the system is overdriven, the wave becomes so large that the surface profile becomes unstable and collapses, which is the equivalence of wave breaking for traveling waves. This results in a singularity where the inertia is concentrated and a jet is formed under favorable circumstances. This phenomenon is known as self-focusing as the fluid focuses its inertia while the entire system is excited [47]. Surface-waves in closed basins are intensively investigated.

Jets are extensively studied and not so uncommon in everyday life as one might expect; actually all unstable cavities produce jets, like impacts on surfaces such as rain drops or a dive in a pool. Applications are for instance in ink-jet printing. A high speed jet can also be used to penetrate the human skin which can be exploited as a drug delivery system. Jets can cause undesired damage as well. For example, underwater propellers or hydraulic pumps can produce cavitation bubbles which in turn create jets that can even wear down metals. In the lab they can be produced with various other methods. The jets in our setup are unique in the way that they evolve from standing waves, which is a consequence of the driving mechanism. The cavities and jets are extreme instances of the troughs and crests of the wave. Their evolution and transition is particularly interesting. In addition, their generation takes time, whereas the jets in aforementioned examples can be created almost instantaneously. In very short times large forces are required, while this setup creates extreme phenomena for very modest parameters.

1.2 Faraday waves

Parametric excited surface waves are named after Michael Faraday for his famous work, titled "*On the forms and states assumed by fluids in contact with vibrating elastic surfaces*" [39]. Our investigation is as this title describes with the complement that we consider standing waves in confined, non-elastic containers and their over excitation as to generate jets in particular. In this graduation assignment we will examine the (nonlinear) standing waves in a vertically vibrated container. The dimensions are such that wall effects are not dominant and the fluid is not in the shallow regime. In fact, we will especially emphasize on the cylindrical symmetric ground state, which implies the wavelength corresponds to the container's dimension. Overdriving of the standing wave will shape its trough as a cavity, resulting in a jet upon collapse.

The layout of this report is as follows. In the second chapter, Theoretical Aspects, we will consider the parametric forcing, the dynamics of surface waves and cavities and jets. The experimental facilities and procedures are described in the following chapter, where we will discuss the equipment used to capture the dynamics of the fluid in the lab. We continue with the analysis and results of the experiments and, whenever possible, compare them with the model. In the numerical chapter we consider various methods to exploit the model. Finally, a conclusion and discussion are provided.

1.3 Research questions

In this thesis we will focus on to the following research questions.

- i) Which contributions have to be taken into account to design a satisfactory model, that adequately describe experimental observations?
- ii) How do we design an experiment that obtains accurate data for a considerably large parameter range?
- iii) What kind of jets can be generated in this setup and are the available descriptions sufficiently adequate?
- iv) Can we design an accurate model describing the whole range of dynamics, to bridge the gap between wave and jet modeling?

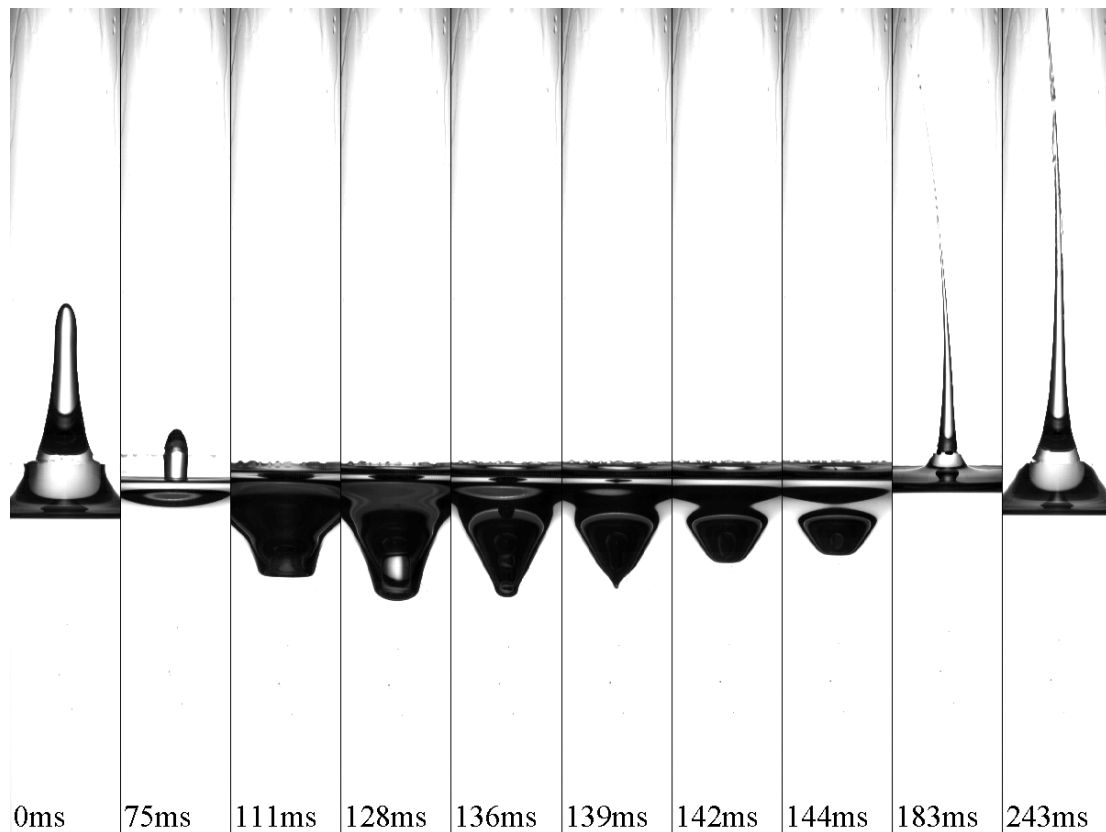


Figure 1.1: A standing wave in sunflower oil transitioning in a cavity and jet formation.

Chapter 2

Theoretical Aspects

For the theoretical aspects we will consider a similar outline as in the Introduction. First the forcing mechanism is investigated. Vibration of the container is a parametric oscillations that leads to equations of the Mathieu type. The excitation is a specified function of time and corresponds to uniform motion of the cylinder containing the fluid. Hence, we consider the harmonic oscillator before we evaluate the equations of motion of the fluid. This one-dimensional description of parametric oscillations is a good starting point to examine the properties of Faraday excitation.

Secondly, the dynamics of surface waves are considered. We will start from the incompressible Navier Stokes equations and treat two boundary conditions. We require impermeability and no-slip at solid interfaces and the kinematic and no-stress conditions at the air-fluid interface. Physical arguments allow us to distinguish the bulk flow in this problem and corrections are later added to repair the neglected contributions. The largest part of the flow is irrotational because inertia is dominant and it initially rotational free. The fluid is restricted by the container and its surface, so the impermeability and kinematic boundary conditions are more important. We have to select one boundary condition to prevent an overdetermined system.

The other conditions are met by rotational flow fields which are denoted as boundary layers because they are only significant close to the boundaries. The concept of these layers is well-known, but their influence on the total flow is not often considered. To do so in this study, we calculated the mechanical energy of the flow field. Finally, wetting dynamics like contact line movement and pinning are treated. We assumed that dissipation arising from these effects are at the expense of the mechanical energy of the fluid.

In the third part cavities and jets are investigated. Several known solutions and methods describing these phenomena are offered. We will treat various examples of jets and cavities in other systems, because their dynamics is universal in specific cases. Often jet creation is preceded by a singularity, which is the collapse of the cavity in our case. Moreover, a mechanism is needed to concentrate enough inertia in a small volume to produce the jet. In many systems the forcing needs to be designed specifically for this purpose, whereas Faraday

waves are characteristic for their self-focusing. The standing waves accumulate inertia until the surface becomes unstable and a cavity collapse follows. The surface of the crest before jetting can be unstable as well, e.g. droplet pinch-off, which may potentially lead to very irregular but beautiful jets.

We would like to make a few notions on possibly uncommon conventions in this chapter. An integral is often written with for a general variable of integration, i.e. $\int dx$. x should be interpreted as a general coordinate or coordinates and it will be clearly stated what the domain and variable of integration specifically is. Often it is written as a subscript with the integration sign, e.g. $\int_F dx$ is an integration over F and the integrand should be evaluated for variables that are in F . Other subscript denote indices, e.g. u_r is the velocity in the r direction. Derivatives will always be written with a clear differentiation sign, like ∂ or a dot over the symbol. We often use kinematic constants in this report. Surface tension and viscosity are denoted by γ and μ respectively, while divided over the density they are $\bar{\gamma}$ and ν .

2.1 Parametric oscillations

Oscillations occur in many physical systems. Engines, electrical circuits or planetary orbits are all examples. In most of the cases some variable, temperature, potential, displacement, oscillates around a semi stable state. The period and amplitude of such motions are depended of certain parameters, like conductivity, gravity, density, etc. They are normally a constant in the system under consideration, like the length of a pendulum's rod but certain systems impose an oscillation on those values, hence parametric oscillations. In the case of the pendulum one can design the rod such that its length changes over time. Oscillatory parameters can drive the system. For instance, a person's change in angular momentum drives the motion of a swing.

In this section we will limit ourselves to one dimensional, (semi-)linear undamped systems of the Mathieu type. The variable of interest is denoted by x as a function of t . We start out with the equation of motion and consider solutions from an intuitive description towards Fourier decomposition. Next we will include friction and limited nonlinearities. We finish with a notion on the operator involved in these systems.

2.1.1 Mathieu function

Consider a simple harmonic oscillator. Its acceleration is negatively proportional to this displacement from its equilibrium, in formula;

$$\ddot{x} + \Omega^2 x = 0, \quad (2.1)$$

with Ω the eigenfrequency of the system, which generally depends on the gravitational constant g as well as on the system dimensions. This parameter is now harmonically perturbed with dimensionless amplitude f such that eq.(2.1) will change to

$$\ddot{x}' + \Omega^2 (1 - f \cos \omega_0 t) x' = 0, \quad (2.2)$$

where ω_0 is the driving frequency. It is known as a Mathieu system because of the harmonic oscillation of the perturbation. A new time coordinate, $t' = \omega_0 t/2$, will help one understand its behavior. The following relation is known as the canonical form of Mathieu's differential equation [67].

$$\left(\frac{\partial^2}{\partial t'^2} + p - 2q \cos 2t' \right) x' = 0, \quad (2.3)$$

with frequency detuning $p = 4\Omega^2/\omega_0^2$ and external action $q = 2f\Omega^2/\omega_0^2$. Although q is zero when p is as well, hypothetically the last case with $q \neq 0$ corresponds to an ideal pendulum. The solutions are known as Mathieu functions and are inseparable from Faraday excitation. They were first related with one another by Benjamin and Ursell [6] and are known for their characteristic period doubling. This is because $p = 1$ is the fastest growing mode and the harmonicity (the motion being period doubled, isochronous or super-harmonic) generally depends on the ratio $\Omega/\omega_0 = \sqrt{p}/2$. A phase chart is plotted in figure 2.1, in which one can observe a qualitative amplitude response [67]. One observes other unstable regions around $p = 4, 9, 16, \dots$, although very narrow for small q . We will focus our attention on the region around $p = 1$.

2.1.2 Solutions

We will first show how this period doubling can intuitively be understood. We drop the accents on the variables, substitute $x = a(t) \cos \omega_1 t$ in eq.(2.3) and obtain

$$\begin{aligned} x(p - \omega_1^2) &= a(p - \omega_1^2) \cos \omega_1 t = \\ 2aq \cos 2t \cos \omega_1 t &= aq [\cos(2 - \omega_1)t + \cos(2 + \omega_1)t], \end{aligned}$$

where a is assumed to vary slowly, i.e. its temporal derivatives are neglected. The system now appears as a forced harmonic oscillator such that solutions with $\omega_1 = \pm 1$ are in resonance, whereas the other cosine with a frequency of three is off-resonance. Moreover the driving amplitude is proportional to the function own amplitude suggesting exponential growth, especially when p is close to ω_1^2 . A solution of eq.(2.3) is plotted in figure 2.2 showing this behavior. Let us now look at a more exact solution. Put $x = a(t) \cos(t - \varphi(t))$, such that its second derivative can be approximated as

$$\begin{aligned} \ddot{x} &\approx -2\dot{a}(1 - \dot{\varphi}) \sin(t - \varphi) - a(1 - \dot{\varphi})^2 \cos(t - \varphi) \\ &\approx -2\dot{a} \sin(t - \varphi) - a(1 - 2\dot{\varphi}) \cos(t - \varphi), \end{aligned}$$

neglecting second order derivatives and terms quadratic in the first derivative, because we still assume slowly varying amplitudes and small q . Next we drop the off-resonance term by approximating

$$2x \cos(2t) \approx a \cos(t + \varphi) = a \cos(2\varphi) \cos(t - \varphi) - a \sin(2\varphi) \sin(t - \varphi) \quad (2.4)$$

and substitute the results in eq.(2.3), which we regroup in a term proportional to $\sin(t - \varphi)$ and one proportional to $\cos(t - \varphi)$. Both terms should be zero,

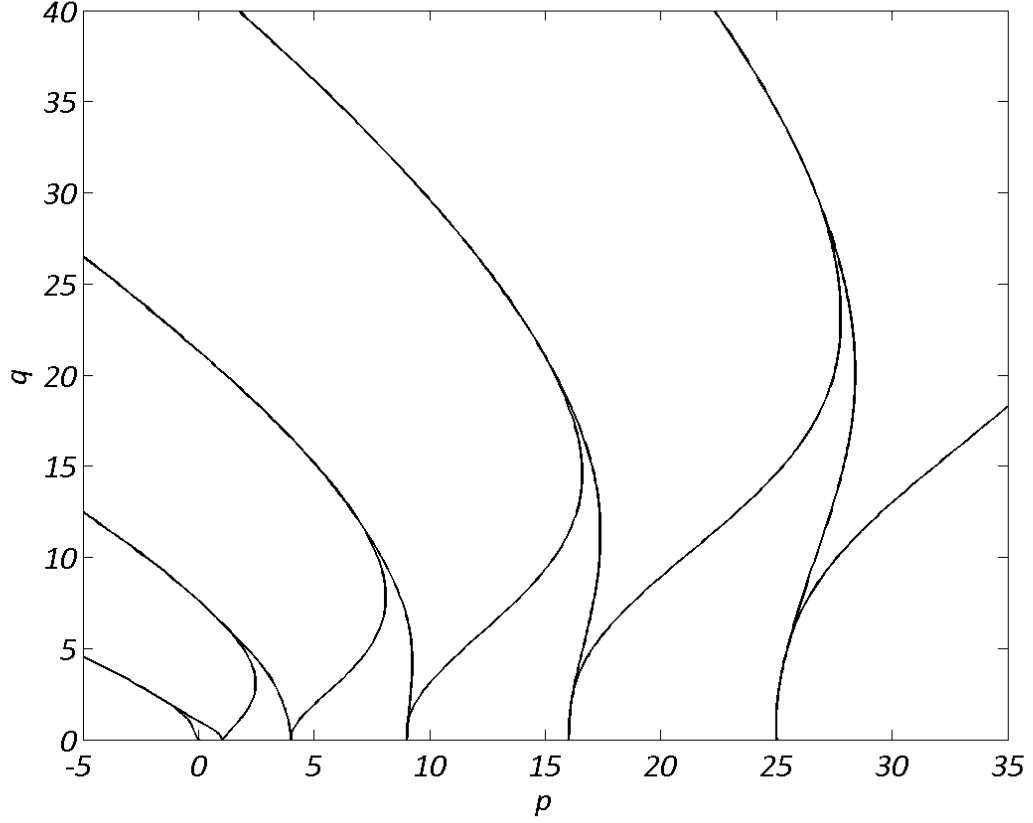


Figure 2.1: Stability chart for Mathieu's equation [67]. The lines denote the transition from stable to unstable (growing) solutions. The stable regime are the areas between the horizontal axis and these lines, also known as Arnold tongues.

such that one yields for the latter

$$\begin{aligned} 2\dot{\phi} &= q \cos 2\varphi + 1 - p = q [\cos 2\varphi - \cos 2\varphi_0] \\ &= -2q \sin(\varphi + \varphi_0) \sin(\varphi - \varphi_0). \end{aligned}$$

We defined $\cos 2\varphi_0 = (p - 1)/q$. The phase does not depend on the amplitude and one sees it is stationary and stable for $\phi = \phi_0$. Hence, the phase of the signal will lock itself relative to the excitation. For the sine part of the equation one has $2\dot{a} = aq \sin(2\varphi)$. When the phase reached its equilibrium, i.e. $\phi = \phi_0$ we find

$$2\dot{a} = aq \sin \left(\cos^{-1} \left(\frac{p-1}{q} \right) \right) = a\sqrt{(q^2 - (p-1)^2)}, \quad (2.5)$$

using trigonometric relations. We find the exponential growth rate

$$\alpha = \frac{1}{2} \sqrt{(q^2 - (p-1)^2)}. \quad (2.6)$$

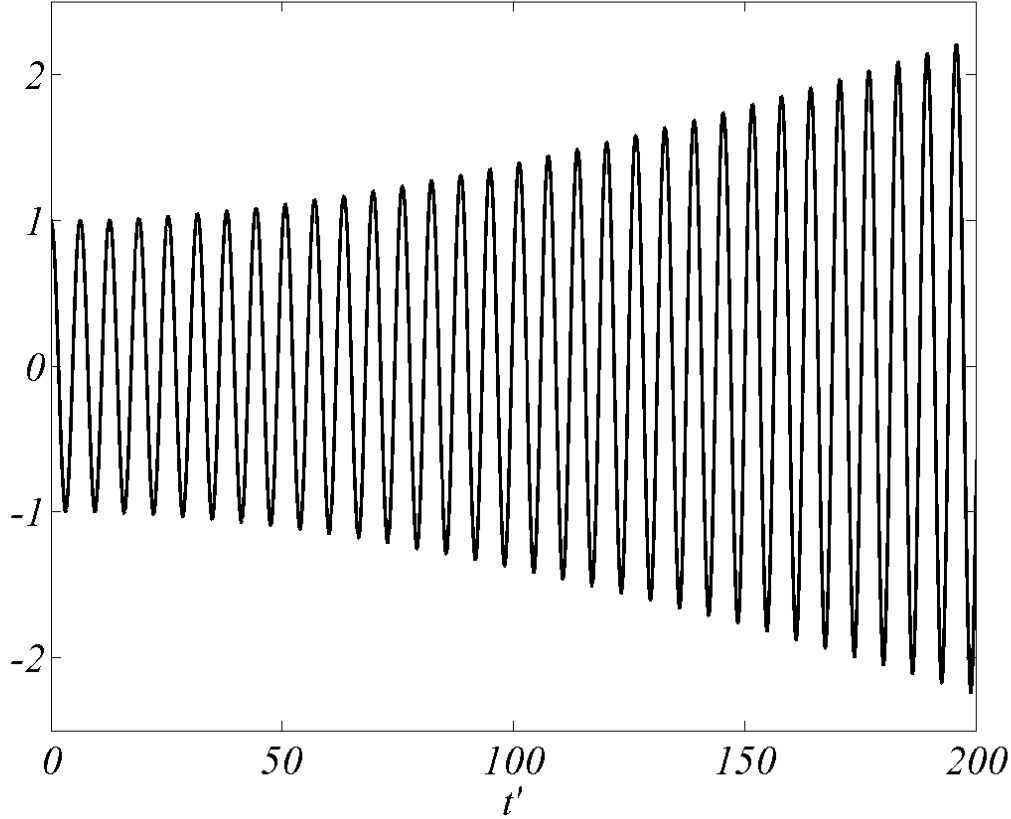


Figure 2.2: Unstable Mathieu function for $p = 0.992$ and $q = 10^{-2}$.

The solution grows for real α , i.e. $|p - 1| < |q|$. For example the rate is $|q|/2$ for p unity. Imaginary α implies the amplitude oscillates. In figure 2.3 a solution is plotted for $2\pi\alpha^{-1} = -200i$. There are large frequency components around $\pm(1 \pm i\alpha)$ as expected. Their magnitude is not equal though which can be explained by complications with the relation for φ now α is imaginary. Their nature is described using Fourier theory.

2.1.3 Fourier series

A Laplace series expansion of Mathieu functions seems natural as one expects growing oscillations. However as the exponential growth rate is predicted to be of a single unique argument, we can divide the motion and investigate the oscillations. We use the notation for transformations according to $x(t) \hat{=} \hat{x}(\omega)$, with $\hat{=}$ denoting the Fourier transform. In the frequency space eq.(2.3) is

$$(-\omega^2 + p - q \{\delta(\omega - 2) + \delta(\omega + 2)\} *) \hat{x}(\omega) = 0, \quad (2.7)$$

which leads to

$$(p - \omega^2)\hat{x}(\omega) - q \{\hat{x}(\omega - 2) + \hat{x}(\omega + 2)\} = 0. \quad (2.8)$$

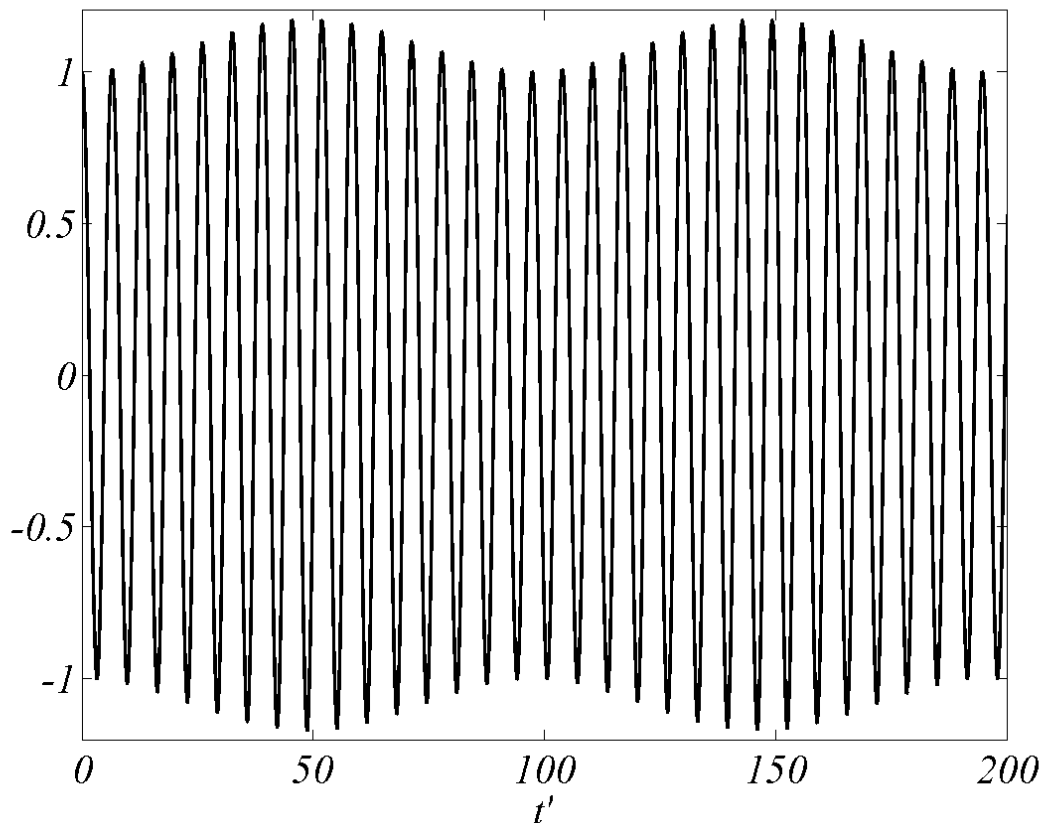


Figure 2.3: Stable Mathieu function for $p = 0.936$ and $q = 10^{-2}$.

In here δ is the Dirac delta function and $*$ denotes convolution. We now have a recursive series for the frequency components of the Mathieu function. A first try would be frequencies at $\omega = \pm 1, \pm 3, \pm 5, \dots$, like

$$\hat{x}(\omega) = \sum_{n=-\infty}^{\infty} a_{2n-1} \delta(\omega - [2n - 1]), \quad (2.9)$$

with a an array obeying $a_{n+2} = a_n(p - n^2)/q - a_{n-2}$ due to eq.(2.8). However, this can be a diverging series as real solutions require $\hat{x}(\omega)^* = \hat{x}(-\omega)$ or $a_n^* = a_{-n}$. Hence it is sufficient in the growing region of approximately $|p - 1| < |q|$, e.g. the signal in figure 2.2. A more general solution can be found in

$$\hat{x}(\omega) = \sum_{n=-\infty}^{\infty} [a_{2n-1} \delta(\omega - [2n - 1 - d]) + a_{-2n+1}^* \delta(\omega - [2n - 1 + d])], \quad (2.10)$$

with another form of the detuning, d . In figure 2.4 the spectrum of the signal in figure 2.3 is plotted. The peaks obey relation eq.(2.10) while we neglect the rest of the signal which is due to artifacts of the discrete Fourier transform and the

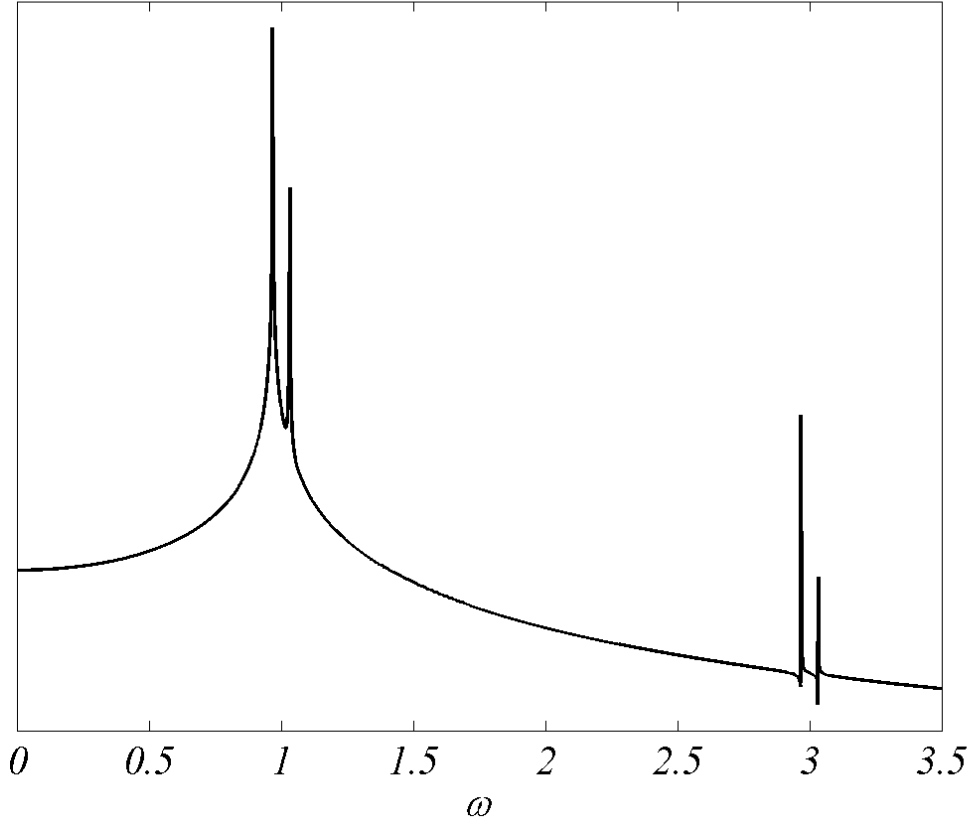


Figure 2.4: Logarithmic scaling of $|\hat{x}|$ (arbitrary units) for $p = 0.936$ and $q = 10^{-2}$.

logarithmic plotting. A phase diagram is obtained after numerical integrating eq.(2.3) and fitting it to $x \exp(-\beta t + \beta_0)$ in a least square sense. In figure 2.5 d and β are plotted for a limited range of p and q . The area where β is non-zero, is similar to the unstable regime in fig.2.1. Also, the detuning d is zero here, following the series in eq(2.9). Also, in figure 2.6 the difference with α from eq.(2.6) is plotted. The shows our prior analysis was reasonable accurate. The error is mainly due to the symmetry of α in $p = 1$ which is an oversimplification for significant q . This can also be observed from the phase chart in figure 2.1.

2.1.4 Friction

Dissipation is straight-forward to include in the original relation of eq.(2.3).

$$\ddot{x} + \beta \dot{x} + (p - 2q \cos 2t) x = 0, \quad (2.11)$$

with known function $\beta(t)$. A solution can be transformed to $x = x' \exp(-B(t))$ with

$$B(t) = \beta_0 + \frac{1}{2} \int_0^t \beta d\tau \quad (2.12)$$

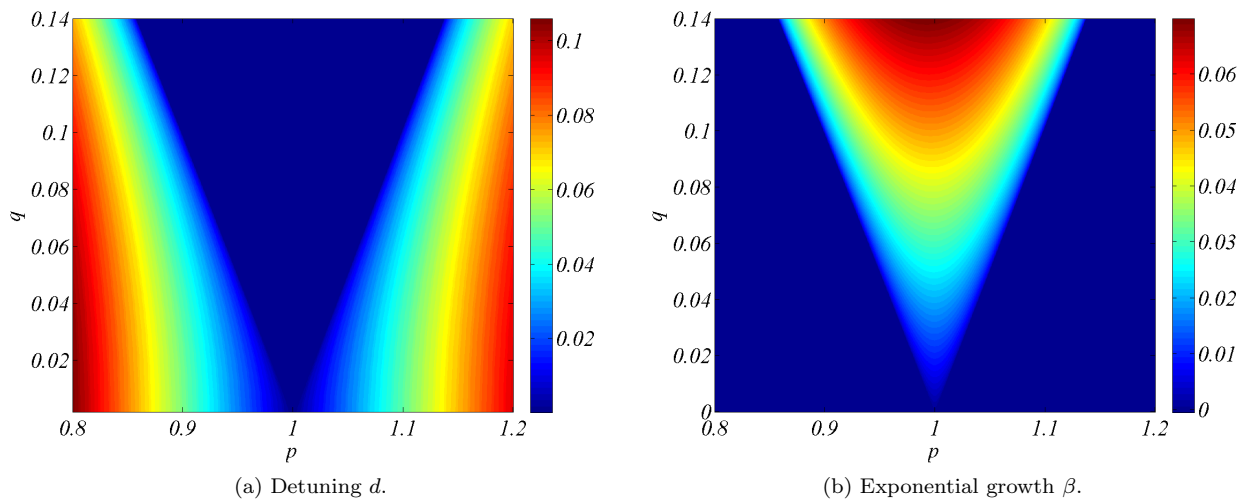


Figure 2.5: Phase diagrams by numerical integration of eq.(2.3).

and β_0 a constant, such that

$$\ddot{x}' + \left(p - \frac{1}{4}\beta^2 - \frac{1}{2}\dot{\beta} - 2q \cos 2t \right) x' = 0 \quad (2.13)$$

is our new differential equation. It is a more general parametric oscillation and only Mathieu like for linear damping, i.e. constant β . Combined with the unstable solutions from the previous section, one can find a larger region of (semi-)stable solutions since one may add the contributions of growth (eq.(2.6)) and decay to find the effective exponential argument $\alpha t - B(t)$.

2.1.5 The Sturm-Liouville Operator

Another way to describe the system is to define the Mathieu operator

$$M_q x = 2q \cos 2t' - \frac{\partial^2}{\partial t'^2}, \quad (2.14)$$

such that Mathieu functions are eigenfunctions of

$$M_q x = p x, \quad (2.15)$$

with real eigenvalues p . The Mathieu function is a special case of the Sturm-Liouville operator, $S : L_w^2(0, \infty) \rightarrow L_w^2(0, \infty)$ by

$$Sx = \frac{1}{w(t)} [-\partial_t(s(t)\partial_t x) + r(t)x] \quad (2.16)$$

on domain $D(S) = \{x \in L_w(0, \infty) \mid \partial_t(s(t)\partial_t x) \in L_w(0, \infty)\}$. The weight functions, s and w equal unity in our case whereas $r = 2q \cos 2t'$ for Mathieu solutions. With appropriate boundary conditions it is a self-adjoint operator as can be shown by integration by parts, although real eigenvalues were the only

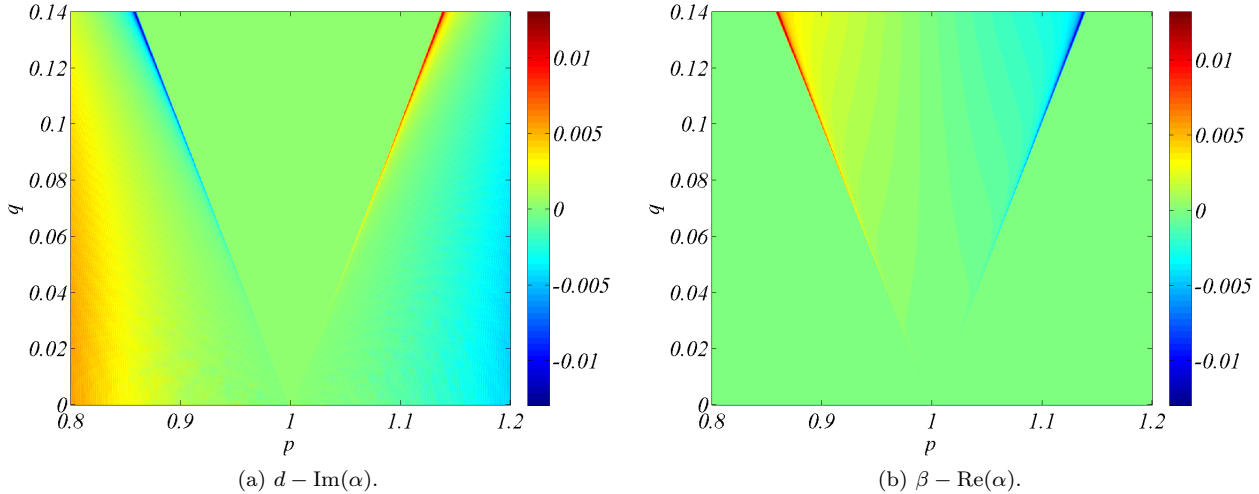


Figure 2.6: Difference between phase diagrams in figure 2.5 and eq.(2.6).

interest in the first place. However if we can construct the domain such that it is, the Sturm-Liouville operator, and therefore the Mathieu operator is densely defined and closed as well. Sturm-Liouville problems are deeply studied [65].

2.1.6 Faraday waves

Let us now look how parametric instabilities occur in fluid mechanical systems. Faraday describes wave patterns of fluids in vibrating containers [39]. There are two driving mechanisms. First, vibrations of the wall itself leading to the so-called singing wineglass. A recent study, including a historical and publication overview, was done by Voges [91]. The other approach is a vertical oscillation the entire container. In this report we will exploit the latter method. Although the reader may intuitively understand the origin of the modified acceleration, we will briefly explain the coordinate transformation involved.

Finding the equations of motions prove to be easier after a transformation of coordinates. In earth's reference frame the boundaries are moving according to a known function, i.e. the configured forcing of the container. It follows that the fluid locally matches the velocity of the walls. One can simplify the boundary condition by describing the motion in the container's frame of reference. However this is at the costs of d'Alembert acceleration. Intuitively, one understands the acceleration will be opposite to the acceleration of the motion. Here we will lay out a framework using covariant differentiation such that the equation hold in all coordinate systems [29].

Now, suppose earth's vertical coordinate (z') relates to the containers vertical coordinate $z = z' + r(t)$ with r the container movement and $t = t'$ the temporal coordinates in the container's and earth's frame respectively. The

invariant distance in this two-dimensional system is

$$ds^2 = dt'^2 - dz'^2.$$

The 'four-velocity' field, $u^{\alpha'}$ is subject to the acceleration

$$a^{\alpha'} = u^{\beta'} u_{,\beta'}^{\alpha'}.$$

For instance, the acceleration in the vertical direction here is $u_{t'} \partial_{t'} u_{z'} + u_{z'} \partial_{z'} u_{z'}$ where summation over indices occurring both in sub- and superscript within a term is implied. This acceleration equals to the material derivative for unit $u_{t'}$, i.e. for non-relativistic lateral velocities. One reads off the metric: $g_{\alpha'\beta'} = \text{diag}(1, -1)$ for $x^{\alpha'} = (t', z')$. In the new system $x^\alpha = (t, z)$ and

$$g_{\delta\gamma} = g_{\alpha'\beta'} x_{,\delta}^{\alpha'} x_{,\gamma}^{\beta'} = \begin{bmatrix} 1 - \dot{r}^2 & -\dot{r} \\ -\dot{r} & -1 \end{bmatrix}, \quad (2.17)$$

with a dot denoting differentiation. In these coordinates the acceleration in the vertical direction is

$$u_t \partial_t u_z + u_t^2 \ddot{r} + u_z \partial_z u_z.$$

Now put $r \sim f \cos \omega t$ such that we can motivate relations like eq.(2.2).

A note can be made on the flatness of this space. Normally gravity has to be included in the metric. As our system does not experience relativistic speeds and has a single gravitational constant we can write the gravitational potential as $-gz$. Then one modifies the metric $g_{t't'} = 1 + 2gz$. This is known as the Newtonian approximation of the space at the earth's surface. One may also modify the metric by choosing new coordinates that accelerate upwards, e.g. $z = z' + gt'^2/2$. Locally this will result in the same acceleration. Another note is on the invariant distance in the new frame of reference. It 'feels' unnatural that there are off-diagonal elements in the metric because it suggests that the new coordinates are not curvilinear. Well, they are not. It accounts for an infinitesimal displacement if we added up the contribution of the container's movement.

2.2 Gravity Waves

Until now we did not go into the fluid dynamics of our system. First a general overview of the configuration is presented. We will describe the system, its governing equations of motion, the basics of surface dynamics and the imposed boundary conditions. Then we will propose a model based on irrotational bulk flow with boundary layers. Finally, we will evaluate the mechanical energy of our system.

2.2.1 The Navier Stokes Equation

An incompressible fluid is located in vertically oriented cylinder. The coordinate system is initially fixed to the center of the undisturbed fluid surface. Its coordinates are (t, r, θ, z) corresponding to the temporal, radial, azimuthal and vertical coordinates respectively. We often assume radial symmetry, hence

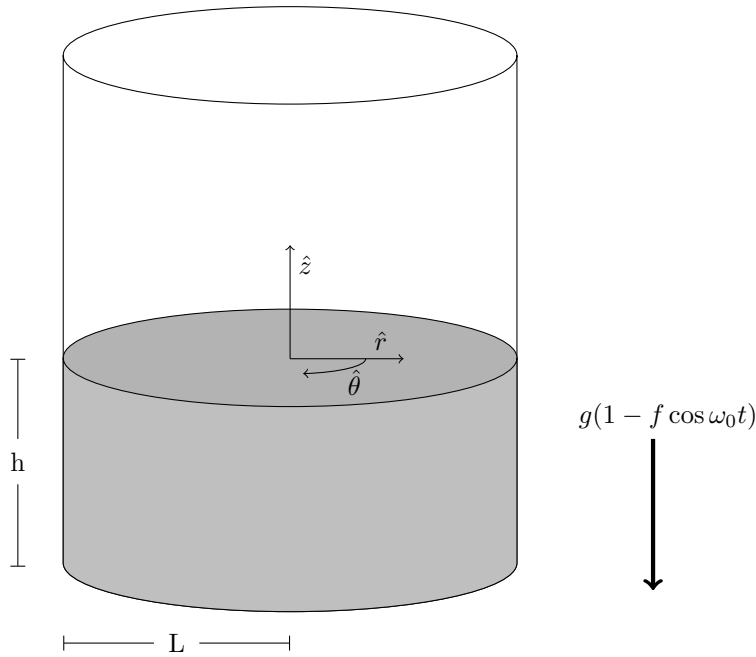


Figure 2.7: Faraday excitation in the cylinder frame of reference

θ is only considered occasionally, e.g. for integration. As the cylinder is vibrated vertically the system experiences a modified gravitational acceleration, $\bar{g} = g(1 - f \cos(\omega_0 t))$. The control volume \mathcal{V} remains constant over time and since the cylinder has radius L , the fluid has a mean depth of $h = \mathcal{V}/\pi L^2$. The surfaces containing \mathcal{V} are $\partial\mathcal{V}$ containing the free surface, S , the wetted boundary of the cylinder, W and the bottom, B . The contact line, Γ , is the intersection of S and W . See figure 2.7.

The fluid is also of the Newton type such that we start with the incompressible Navier-Stokes equation. The flow field \mathbf{u} is subject to

$$\nabla \cdot \mathbf{u} = 0, \quad (2.18)$$

$$\begin{aligned} \mathbf{N} &= D_t \mathbf{u} - \mathbf{g} - \frac{1}{\rho} \nabla \cdot \boldsymbol{\tau} \\ &= (\partial_t + \mathbf{u} \cdot \nabla) \mathbf{u} - \mathbf{g} + \frac{1}{\rho} \nabla p - 2\nu \nabla^H \mathbf{u} = 0, \end{aligned} \quad (2.19)$$

with body force $\mathbf{g} = -\bar{g}\hat{z}$, density ρ , viscosity $\mu = \rho\nu$, stress tensor $\boldsymbol{\tau}$ and pressure p . It seems trivial to introduce the vector \mathbf{N} as it is zero, but it will be convenient later in this section. Sometimes it is convenient to write the

equations in tensor form.

$$u_{;\alpha}^{\alpha} = 0, \quad (2.20)$$

$$N^{\beta} = u^{\alpha} u_{;\alpha}^{\beta} - \frac{1}{\rho} \tau_{;\alpha}^{\alpha\beta} = 0. \quad (2.21)$$

Gravity is included in the coordinates and covariant differentiation is implied as in section 2.1.6.

2.2.2 Surface dynamics

In this section we will present a brief overview of free surface relations. In the (r, z) -plane, the outward normal and tangential unit vectors are $\hat{\mathbf{n}}$ and $\hat{\mathbf{t}}$. In absence of a hat they are not assumed to be normalized. Note that because of the cylindrical symmetry the normal vector is always in this plane and that the other tangential vector or binormal vector ($\hat{\mathbf{b}}$) is perpendicular to it, i.e. aligned with $\hat{\theta}, \hat{\mathbf{b}} = \hat{\mathbf{t}} \times \hat{\mathbf{n}}$.

The upper boundary or free surface can locally be expressed by its curvature k , arclength ξ , tangent angle α or profile $F(r, z) = 0$, see figure 2.8. They can be related as

$$\hat{\mathbf{n}} = \frac{\partial \hat{\mathbf{t}}}{\partial \alpha} = \begin{bmatrix} -\sin \alpha \\ 0 \\ \cos \alpha \end{bmatrix} = \frac{\nabla F}{|\nabla F|}, \quad (2.22)$$

$$\hat{\mathbf{t}} = -\frac{\partial \hat{\mathbf{n}}}{\partial \alpha} = \begin{bmatrix} \cos \alpha \\ 0 \\ \sin \alpha \end{bmatrix} = \partial_{\xi} \begin{bmatrix} r \\ \theta \\ z \end{bmatrix}, \quad (2.23)$$

$$k = \frac{\partial \alpha}{\partial \xi} = \left| \frac{\partial \hat{\mathbf{t}}}{\partial \xi} \right| = -\nabla \cdot \hat{\mathbf{n}} = -\nabla \cdot \frac{\nabla F}{|\nabla F|}. \quad (2.24)$$

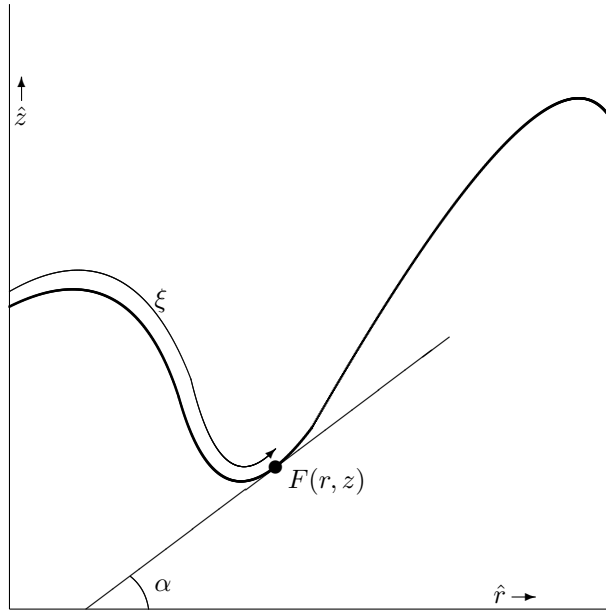
The first relation in eq.(2.24) is known as the Cesàro equation. Also, note that in general $k \partial_{\alpha} = \partial_{\xi}$ and $\partial_{\alpha}^2 = -1$. One can find the relationship between the curvature and the normal vector by

$$k = \frac{\partial \alpha}{\partial \xi} = \frac{\partial \alpha}{\partial x^j} \frac{\partial x^j}{\partial \xi} = \frac{\partial \alpha}{\partial x^j} \hat{t}^j = -\frac{\partial \alpha}{\partial x^j} \frac{\partial \hat{n}^j}{\partial \alpha} = -\frac{\partial \hat{n}^j}{\partial x^j}.$$

In literature an alternative definition of the curvature is occasionally used [35, 80]. Also, the arclength can be viewed as one of the surface coordinates in the surface description of Sriven [80].

2.2.3 Boundary conditions

The kinematic surface condition states the flow is contained in its boundaries; the fluid has the same velocity as its surfaces. For the solid cylinder walls and bottom this condition is straightforward as they are stationary in the conveniently defined coordinate system, stated $\mathbf{u} \cdot \hat{\mathbf{n}} = 0$. Nevertheless, we will not

Figure 2.8: Surface variables in the (r, z) -plane

consider the bottom boundary anymore as the fluid is assumed very deep, such that it is not 'felt' by the surface motion. In section 2.2.5 we will show that it indeed the case.

As for the free surface, one notes the Lagrangian derivative of F should be zero.

$$0 = D_t F = \partial_t F + \mathbf{u} \cdot \nabla F. \quad (2.25)$$

The mathematical distinctions between boundaries can be omitted if F is defined as the boundary of the fluid, i.e. $F = \partial \mathcal{V}$. At the stationary walls, $\partial_t F = 0$ so $\mathbf{u} \cdot \hat{\mathbf{n}} = \mathbf{u} \cdot \nabla F$. The kinematics condition for all boundaries are now given by eq.(2.25). The parameterization of F can be utilized. Often there is unique relation of the profile in one of the coordinates, say $F = \eta(t, r) - z$, e.g. fig 2.8, such that

$$0 = \partial_t \eta + u_r \partial_r \eta - u_z. \quad (2.26)$$

This can be especially be convenient in momentum equations, as the local gravitational pressure is proportional to η . It also allows to conveniently express the fluid domain, which will be contained in $0 \leq r \leq L, -h \leq z \leq \eta(r, t)$.

For solid boundaries the tangential velocity component is zero along the walls, the no-slip condition or $\mathbf{u} \cdot \hat{\mathbf{t}} = 0$. As a consequence the derivative of this component in the same direction is zero as well, i.e. $\hat{\mathbf{t}} \cdot \nabla \mathbf{u} \cdot \hat{\mathbf{t}} = 0$. Because of continuity this also results in $\hat{\mathbf{n}} \cdot \nabla \mathbf{u} \cdot \hat{\mathbf{n}} = 0$. In fact the only non-vanishing term is $\hat{\mathbf{n}} \cdot \nabla \mathbf{u} \cdot \hat{\mathbf{t}}$. At the free surface there is of course a no-slip condition too, but it is relative to the surrounding air. We assume that the air flow will follow the liquid motion without influencing nor disturbing it significantly. This can be explained as follows. If we denote $\delta(\cdot)$ as the difference in any quantity of

both media along the interface, the above relations hold for $\delta\mathbf{u}$ as well. This can have a large influence on the dynamics. For instance, the densities are added to find inertia but subtracted to find restoring forces like buoyancy. The stress tensor has to be evaluated for a difference in properties as well [55]. In our experiments we will use air as the fluid on top of our liquid. At room temperatures air has the following density $\rho = 1.23\text{kgm}^{-3}$ and viscosity $\mu = 17.8\mu\text{kgm}^{-1}\text{s}^{-1}$. This will be small compared to the properties of the liquid so will neglect this effect. Turning around, a system where wind is the driving force couples the motion of the air to the fluid. In many cases the air flow high above the liquid is known. The investigation then limits to region around the surface that matches both flow fields. The influence of the wind can be approximated in this way [69, 13, 16].

In this region not only the no-slip condition has to be met but the surface forces need to be balanced as well. Any deformation of a free surface generates viscous stress, hence we have other boundary conditions to account for on the free surface. The reader probably is familiar with the pressure jump caused by the curvature of the surface. Tangential forces have to be continuous for continuous flow fields as well[17]. We would like to summarize the derivation as proposed by Scriven [80], because it describes the origin of the stresses very well. The forces on a two-dimensional surface are balanced assuming it is Newtonian interface. It means the stresses are linear with the the strain rate and all tensors are isotropic such that only three coefficients are needed to describe the stress on the surface¹. Those are the surface tension $\bar{\gamma}$, the dilatation viscosity κ_s and the shear viscosity ϵ_s . For clean surfaces its only relevant result is the aforementioned pressure jump of $\bar{\gamma}k$. However for an interface with surface active elements $\bar{\gamma}$ might depend on the lateral coordinates and the viscosities can be of significant value. Marangoni effects are examples of these dynamics. We found negligible interfacial viscosities such that the following conditions holds for the normal and tangential directions.

$$0 = \hat{\mathbf{n}} \cdot \boldsymbol{\tau} \cdot \hat{\mathbf{n}} + \bar{\gamma}k, \quad (2.27)$$

$$0 = (\hat{\mathbf{n}} \cdot \boldsymbol{\tau} - \nabla\bar{\gamma}) \cdot \hat{\mathbf{t}}. \quad (2.28)$$

Solutions are proposed by using the diffusion relation to relate $\bar{\gamma}$ to the flow field [60, 35]. One finds $\hat{\mathbf{n}} \cdot (\nabla^H + \lambda_s)\mathbf{u} \cdot \hat{\mathbf{t}} = 0$ in eq.(2.28) with λ_s a complex contamination length depending on surfactant properties [72, 46]². A clean surface corresponds to a very small value whereas the opposite limit means the interface actually is an inextensible film.

In our experiments we found that the surface tension of our fluids was close to value for pure liquids in literature. Furthermore, it did not vary over very large time intervals (months). Therefore, we will put $\nabla\bar{\gamma} = 0$ in this report. This brief analysis was included since we looked for possible surface effects. If one suspects an significant contribution from surface stresses, useful experimental procedures for determining their contribution are suggested, e.g. frequency analysis of waves in the fluid of interest [35].

¹Note the analogy with the stresses for a (three-dimensional) Newtonian fluid, e.g. §4.10 in [56].

²These authors define a length as the reciprocal of λ_s .

2.2.4 Equations of Motion

We briefly summarize this section in a system of equations. The flow field \mathbf{u} is subject to

$$\nabla \cdot \mathbf{u} = 0 \quad \text{in } \mathbb{V}, \quad (2.29)$$

$$D_t \mathbf{u} - \mathbf{g} - \frac{1}{\rho} \nabla \cdot \boldsymbol{\tau} = 0 \quad \text{in } \mathbb{V}, \quad (2.30)$$

$$\frac{D}{Dt} F = 0, \quad \text{on } F, \quad (2.31)$$

$$\hat{\mathbf{n}} \cdot \boldsymbol{\tau} \cdot \hat{\mathbf{n}} = -\gamma k, \quad \text{on } S, \quad (2.32)$$

$$\hat{\mathbf{n}} \cdot \boldsymbol{\tau} \cdot \hat{\mathbf{t}} = 0, \quad \text{on } S, \quad (2.33)$$

$$\mathbf{u} \cdot \hat{\mathbf{t}} = 0, \quad \text{on } W \cup B. \quad (2.34)$$

Considering the discussion in 2.1 we would like to work towards a temporal ordinary differential equation. This means that we have to make ansatzes for the spatial dependences of the flow considering the previous equations. One may then substitute those in the temporal relations, eq.(2.30)-(2.31) and drop equal spatial dependences as those relations should hold in the entire domain. Here we prefer making a projection of Navier-Stokes onto the states of interest. Later we make physical motivated ansatzes for the flow field, hence we will take the inner product of Navier-Stokes with the velocity field and integrate it over the entire domain. In fact, the quantity evaluated is the mechanical power [89, 56]. For convenience we introduce $(\mathbf{v1}, \mathbf{v2}) = \int_{\mathbb{V}} (\mathbf{v1} \cdot \mathbf{v2}) dx$. Then, $(\mathbf{u}, \mathbf{N}) = 0$ and let us evaluate the terms separately. First the kinetic energy

$$(\mathbf{u}, D_t \mathbf{u}) = \frac{1}{2} \partial_t (\mathbf{u}, \mathbf{u}) - \int_F \frac{1}{2} |\mathbf{u}|^2 \mathbf{v}_F \cdot \hat{\mathbf{n}} dx + \frac{1}{2} (\nabla \cdot \mathbf{u} |\mathbf{u}|^2) \quad (2.35)$$

$$= \partial_t K - \frac{1}{2} \int_F |\mathbf{u}|^2 (\mathbf{v}_F - \mathbf{u}) \cdot \hat{\mathbf{n}} dx, \quad (2.36)$$

where we used Leibniz integral rule with \mathbf{v}_F the velocity of the boundary. As it equals the fluid velocity at the boundary the second term in eq.(2.36) equals zero and the kinetic energy is defined as $K = \frac{1}{2} (\mathbf{u}, \mathbf{u})$.

The body force contributes

$$(\mathbf{u}, -\mathbf{g}) = \bar{g} \int_F z \mathbf{u} \cdot \hat{\mathbf{n}} dx \quad (2.37)$$

and the stresses

$$(\mathbf{u}, -\nabla \cdot \boldsymbol{\tau}) = \int_{\mathbb{V}} \nabla \mathbf{u} : \boldsymbol{\tau} dx - \int_F \mathbf{u} \cdot \boldsymbol{\tau} \cdot \hat{\mathbf{n}} dx. \quad (2.38)$$

On the right hand side the second term increases the kinetic energy while the first term is dissipative, i.e. it increases the thermal or internal energy. This

term shows up with another sign in the heat equation,

$$\partial_t U + \int_{\mathcal{V}} [\nabla \cdot \mathbf{q} - \nabla \mathbf{u} : \boldsymbol{\tau}] dx = 0, \quad (2.39)$$

with \mathbf{q} the heat flux out of the system, such that the sum of stored energy ($K+U$) changes at the rate of work and heat addition. This is known as the first law of thermodynamics. The second term in eq.(2.38) is indeed conservative. Put $\sigma = 2\nu \nabla^H \mathbf{u} = \tau + pI$,

$$\begin{aligned} - \int_F \mathbf{u} \cdot \boldsymbol{\tau} \cdot \hat{\mathbf{n}} dx &= \int_F [u p - \mathbf{u} \cdot \boldsymbol{\sigma}] \cdot \hat{\mathbf{n}} dx = \\ &= \int_F [\mathbf{u} \gamma k + \mathbf{u} (\hat{\mathbf{n}} \cdot \boldsymbol{\sigma} \cdot \hat{\mathbf{n}}) - (\mathbf{u} \cdot \hat{\mathbf{n}}) (\hat{\mathbf{n}} \cdot \boldsymbol{\sigma}) - (\mathbf{u} \cdot \hat{\mathbf{t}}) (\hat{\mathbf{t}} \cdot \boldsymbol{\sigma})] \cdot \hat{\mathbf{n}} dx. \end{aligned}$$

We substituted eq.(2.32) and by (2.33) only the first term remains. Divide it by the density and add the body force (eq.(2.37))

$$P_C = \int_F (\bar{g}z + \bar{\gamma}k) (\mathbf{u} \cdot \hat{\mathbf{n}}) dx. \quad (2.40)$$

When the curvature is the main carrier of potential energy the waves are actually known as capillary waves instead of gravity waves. For the second term in eq.(2.38)

$$P_D = \int_{\mathcal{V}} \nabla \mathbf{u} : \boldsymbol{\tau} dx = \int_{\mathcal{V}} [-p \nabla \cdot \mathbf{u} + \nabla \mathbf{u} : \boldsymbol{\sigma}] dx \quad (2.41)$$

$$= 2\nu \int_{\mathcal{V}} [\nabla u : \nabla^S \mathbf{u} + \nabla \mathbf{u} : (\nabla \mathbf{u})^*] dx$$

$$= \nu \int_{\mathcal{V}} [(\nabla \times \mathbf{u})^2 + 2\nabla \cdot (\mathbf{u} \cdot (\nabla \mathbf{u})^*)] dx$$

$$= \nu \int_{\mathcal{V}} |\boldsymbol{\omega}|^2 dx + 2\nu \int_F \mathbf{u} \cdot \nabla \mathbf{u} \cdot \hat{\mathbf{n}} dx \quad (2.42)$$

$$= \nu(\boldsymbol{\omega}, \boldsymbol{\omega}) + 2\nu \int_F \mathbf{u} \cdot \nabla (\mathbf{u} \cdot \hat{\mathbf{n}}) dx. \quad (2.43)$$

We used the incompressibility condition on the third step and the no-slip condition on the last step. Note that Lamb ([57], §329) finds the same terms although he expands the second integrand in eq.(2.43) as $\hat{\mathbf{n}} \cdot (2\mathbf{u} \times \boldsymbol{\omega} - \nabla \mathbf{u}^2)$.

We modified Navier-Stokes to a mechanical power equation, rearranged in inertial, conservative and dissipative terms:

$$\partial_t K + P_C + P_D = 0. \quad (2.44)$$

2.2.5 Irrotational Flow

It is still difficult to find a specific flow field from these equations. Fortunately, we may use some physical arguments as a kick-start for our model. The flow will

be highly irrotational because inertial forces are larger than viscous forces. This ratio is quantified by the Reynolds number, defined as $\text{Re} = UL/\nu$, is always large in this study. The characteristic velocity and length will be $U \approx 10^0$, $L \approx 10^{-1}$ while the viscosity is $10^{-4} < \nu < 10^{-6}$. This shows that the majority of the field can be approximated by a potential:

$$\mathbf{u} = \nabla\Phi. \quad (2.45)$$

Combined with the incompressibility condition (eq.(2.29)) this leads to the Laplace equation for the potential [56].

However, if the fluid is solely irrotational the system (eq.(2.29)-(2.34)) is overdetermined. Laplace's equation is a second order differential equation so we need only one boundary condition on the entire boundary, whereas there are in fact two on every boundary at least (remember $F = S \cup W \cup B$). One can hold on to the potential in the bulk and allow a complete field close to the boundaries. These regions are called boundary layers. One way to solve is to solve the potential in the bulk and the complete flow with boundary conditions in the layer followed by matching the flows. The matching parameters are the size of the layer and magnitudes of the flows. Another method is to fix the potential to a single boundary condition and add a rotational flow to meet the remaining boundary conditions. We will exploit the latter, although it seems that we are excluding a collection of solutions, i.e. finding the sufficient but non-necessary ones). We will later show that this is not the case. The flow may be decoupled

$$\mathbf{u} = \nabla\Phi + \nabla \times \Psi. \quad (2.46)$$

We now only have to decide which boundary condition should apply to the irrotational bulk flow. It is the kinematic one (eq.(2.31)), because constraining the fluid in the cylinder is more important. The potential flow without boundary layers is still a good approximation in that case, especially away from the boundaries.

Let us first look at the potential part of the flow field. A standing wave ansatz leads to separation of variables

$$\Phi = \phi(t)R(r)\Theta(\theta)Z(z). \quad (2.47)$$

The Laplacian yields

$$\frac{1}{rR}\partial_r(r\dot{R}) + \frac{\ddot{\Theta}}{r^2\Theta} + \frac{\ddot{Z}}{Z} = 0, \quad (2.48)$$

$$\ddot{R} + \frac{1}{r}\dot{R} + \left(\kappa^2 - \frac{s^2}{r^2}\right)R = 0, \quad (2.49)$$

$$\ddot{\Theta} + s^2\Theta = 0, \quad (2.50)$$

$$\ddot{Z} - \kappa^2 Z = 0, \quad (2.51)$$

where κ and s are the radial and azimuthal wavenumbers, which are constants with respect to the coordinates. This formulations allows to eventually sum

s	$\kappa_1 L$	$\kappa_2 L$	$\kappa_3 L$	$\kappa_4 L$	$\kappa_5 L$
0	3.83	7.02	10.17	13.32	16.47
1	1.84	5.33	8.54	11.71	14.86
2	3.05	6.71	9.97	13.17	16.35
3	4.20	8.02	11.35	14.59	17.79

Table 2.1: Zeros of eq.(2.53).

over all allowed values of κ and s , which are found by evaluating the boundary conditions.

The fluid is at rest for $z \rightarrow -\infty^3$ such that κ is real and

$$Z(z) = e^{\kappa z}. \quad (2.52)$$

For the azimuthal dependence one finds harmonic functions as hyperbolic functions are not allowed because of symmetry and continuity, i.e. $\Theta(0) = \Theta(2\pi)$ and $\dot{\Theta}$ must be finite. Hence s is real for the signs in eq.(2.49),(2.50). Moreover they are integers since we require continuity at $\phi(t, r, 0, z) = \phi(t, r, 2\pi, z)$. We select $\Theta = \cos s\theta$ because one can always rotate the coordinates system to align with the motion. The convenience of the cosine is that there are non-trivial solutions for $s = 0$ too and that we can limit ourselves to $s \geq 0$ without loss of generality. At $r = 0$ one requires a finite solution and $R_r = 0$ due to symmetry, so $R \sim J_s(\kappa r)$ with real κ and J_n the n^{th} order Bessel function of the first kind. Although we allow flow along the wall, it cannot flow through it, hence

$$\dot{J}_s(\kappa L) = \frac{s}{L} J_s(\kappa L) - \kappa J_{s+1}(\kappa L) = 0. \quad (2.53)$$

Although this condition has to be met by the total flow, this relation has to be true for all radial wavenumbers independently as they have different vertical dependences, c.q. eq.(2.52). The zeros for a number of modes are listed in table 2.1. By convention one denotes modes by two integers between brackets separated between a comma, the first for the index of the allowed s numbers and the second for κ , both starting at zero. This is convenient because s will equal its index. (n,m) is then the state corresponding to $s_n = n$ and κ_m . For example the so-called slogging state is denoted by $(1,1)$ and the solid body state by $(0,0)$ (or any $(n,0)$ mode). Other examples are visualized in figure 2.9.

³For an impregnable and stationary bottom at $z = -h$ it is $Z(z) = \cosh \kappa(z+h)/\kappa \sinh \kappa h$. A fluid is deep for $\kappa h \geq \pi$ as $\tanh(\pi) = 0.996$.

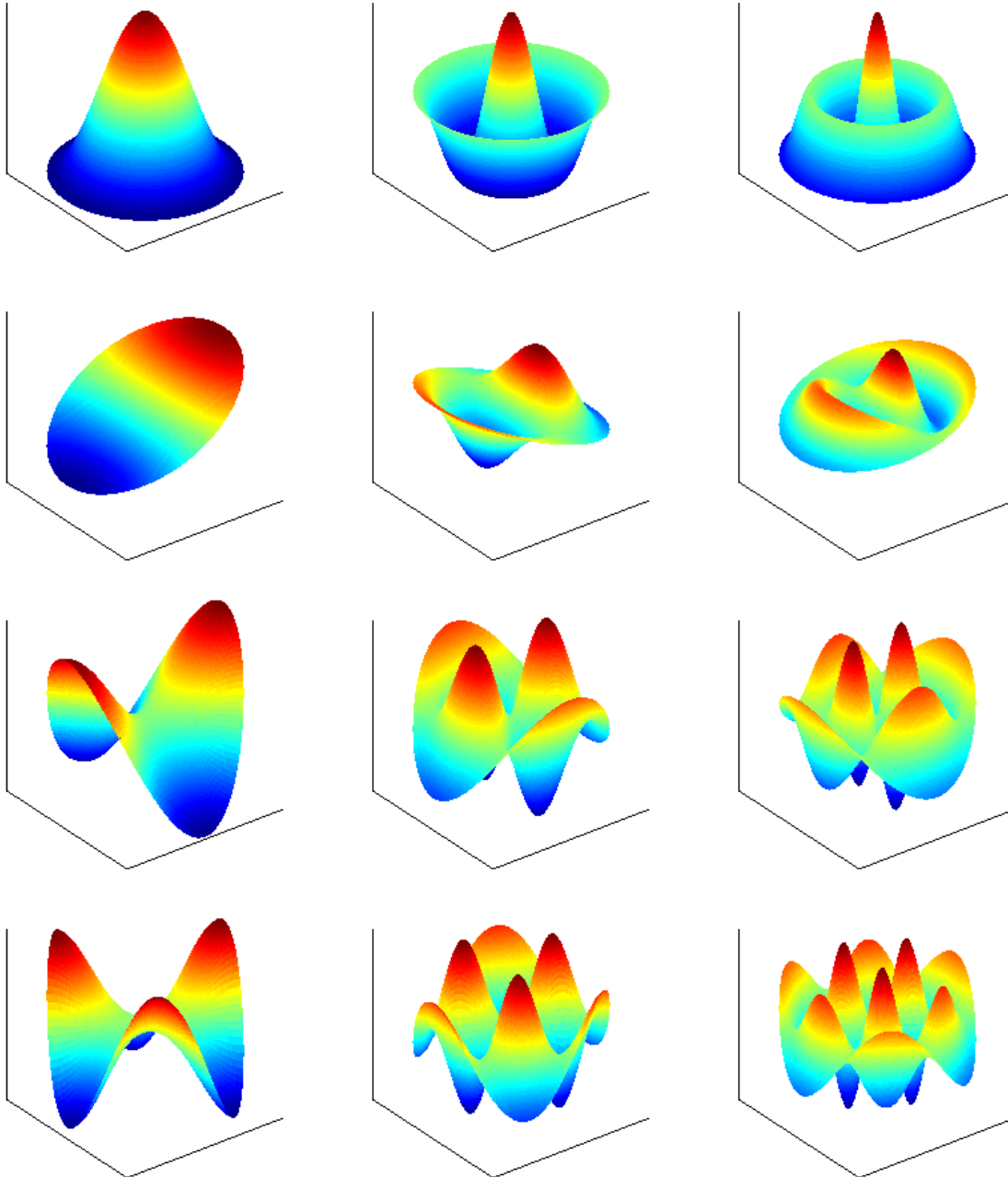


Figure 2.9: Surface wave modes. Top left is mode $(0,1)$ while the bottom right is $(3,3)$.

Moreover Bessel functions are often orthogonal and this is true in the special

case of the zeros defined by eq.(2.53), as long as $s > -1$ [11].

$$\int_0^L J_s(\kappa_n r) J_s(\kappa_m r) r dr = \delta_{nm} \frac{\kappa_n^2 L^2 - s^2}{2\kappa_n^2} J_s^2(\kappa_n L). \quad (2.54)$$

With this in mind we normalize R ,

$$R = \sqrt{\frac{2}{\kappa^2 L^2 - s^2}} \frac{\kappa J_s(\kappa r)}{J_s(\kappa L)}. \quad (2.55)$$

We can also construct Fourier-Bessel series exploiting the orthogonality [11]. Considering the possibility of summation over the wavenumbers and the energy projection this may be a very convenient tool.

2.2.6 Airy theory

The linear approach in the description of gravity waves is commonly known as Airy wave theory named after G.B. Airy [1, 20]. It assumes the contributions of viscosity are small, such that the flow is indeed highly irrotational. We use the surface profile from eq.(2.26) and assume infinitesimal surface elevations such that surface properties and integrals can be evaluated for $z = 0$ instead of $z = \eta$. This also implies vertical normal vectors at the surface, hence $k = -\nabla \cdot \hat{\mathbf{n}} = -\nabla^2 \eta$. In fact, eq.(2.26) itself linearizes to $\hat{T} = \kappa \phi$. Although the surface elevation is small, it should conserve volume because of incompressibility, so we choose the same separation as for the potential.

$$\eta = T(t)R(r)\Theta(\theta), \quad (2.56)$$

where T has dimensions of length and carries the amplitude information of the wave. This also implies that the mode in figure 2.9 correspond to surface profiles. Volume conservation checks out;

$$\int_0^{2\pi} \int_0^L \eta r dr d\theta = 0, \quad (2.57)$$

because the azimuthal integral yields zero except for $s = 0$ when $\int J_0 r dr = 0$ by eq.(2.53). We will now use eq.(2.44) to yield a equation depending on time

only. For $s=0$,

$$K = \frac{1}{2}(\mathbf{u}, \mathbf{u}) = \frac{1}{2}(\nabla\Phi, \nabla\Phi) = \pi\kappa\phi^2, \quad (2.58)$$

$$\begin{aligned} P_C &= \int_F (\bar{g}z + \gamma k)(\mathbf{u} \cdot \hat{\mathbf{n}}) dx \\ &= \int_S (\bar{g} + \kappa^2\bar{\gamma})\eta\partial_z\Phi dx = 2\pi(\bar{g} + \kappa^2\bar{\gamma})\kappa T\phi, \end{aligned} \quad (2.59)$$

$$\begin{aligned} P_D &= 2\nu \int_F \mathbf{u} \cdot \nabla(\mathbf{u} \cdot \hat{\mathbf{n}}) dx \\ &= 2\nu \int_S [\partial_{rz}\Phi\partial_r\Phi + \partial_{zz}\Phi\partial_z\Phi] dx = 8\pi\nu\kappa^3\phi^2, \end{aligned} \quad (2.60)$$

$$(\mathbf{u}, \mathbf{N}) = 2\pi\phi \left(\kappa\dot{\phi} + \bar{\Omega}^2 T + 4\nu\kappa^3\phi \right) = 2\pi\phi \left(\ddot{T} + \bar{\Omega}^2 T + 4\nu\kappa^2\dot{T} \right) = 0, \quad (2.61)$$

where the Mathieu forcing of the dispersion is

$$\bar{\Omega}^2 = (\bar{g} + \kappa^2\bar{\gamma})\kappa. \quad (2.62)$$

When defining detuning and forcing according to section 2.1 one finds the later does not depend on the surface tension, because this parameter is not oscillated.⁴ The terms within brackets in eq.(2.61) may be put to zero and become the governing equation of the system. Note that the linear kinematics are not necessary as one can construct a coupled ordinary differential system. In that case η is not substituted for and eq.(2.19) is then the second equation.

2.2.7 Boundary layers

We will now examine the boundary layers in some detail. We substitute the decomposition eq.(2.46) in the Navier-Stokes (eq.(2.19)). Here we will neglect the convective term in the rotational part because it is small with respect to the temporal derivative, because we expect oscillatory motion due to Mathieu's equation.

$$\nabla \left(\partial_t\Phi + \frac{1}{2}|\mathbf{u}|^2 + \bar{g}z + \frac{p}{\rho} \right) + \nabla \times (\partial_t\Psi - \nu\nabla^2\Psi) = 0. \quad (2.63)$$

Both terms now have to be zero by Hodge theory, hence the terms within brackets have to equal a constant. However, we can always add constants to both potentials with no consequences for the velocity field. Note that the potential part is also known as Bernoulli's equation. We find the rotational differential equation

$$\frac{1}{\nu}\partial_t\Psi = \nabla^2\Psi. \quad (2.64)$$

⁴One could design such a system for example by rapidly varying the temperature, as the surface tension depends strongly on it.

It is also known as the unsteady boundary layer equation. For cylindrical symmetry, separation of variables then gives

$$\Psi = C\psi \exp(\alpha t + \zeta z) J_1(\xi r),$$

with wavenumbers obeying $\alpha/\nu = \zeta^2 - \xi^2$. The real part has physical meaning. $C = \sqrt{2}/L J_0(\kappa L)$ is chosen for easier comparison of the flows, while ψ is a constant yet to be determined. Compare this to eq.(2.47). This will lead to the following velocities following eq.(2.46).

$$\mathbf{u} = C \begin{bmatrix} -\kappa\phi J_1(\kappa r)e^{\kappa z} - \zeta\psi J_1(\xi r)e^{\alpha t + \zeta z} \\ 0 \\ \kappa\phi J_0(\kappa r)e^{\kappa z} + \xi\psi J_0(\xi r)e^{\alpha t + \zeta z} \end{bmatrix}. \quad (2.65)$$

We will first look at the layer at the side wall W , then at the surface layer S . The layer at the bottom is neglected completely. This is allowed if the fluid is deep enough such that the flow is not significant there. We already used this assumption in eq.(2.52). If both boundary layers are significant we of course had to adapt one for the other, as they may disturb each other's boundary conditions.

The problem of a fluid at rest stressed by a infinite oscillating plate is known as Stokes's second problem [79]. Since the coordinate transformation to form this system is only in the (t, z) -plane it will only result in an Alembert correction, but gravity has no influence on the rotational flow (eq.(2.63)). However, this problem does not allow vertical dependence of the flow. From eq.(2.65) we clearly see this dependence in the velocities at the wall. Putting $\zeta = \kappa$ makes sure this dependence is the same. Next, we meet the impermeable condition $J_1(\xi L) = 0$, which restricts ξ . Finally, we solve for the no-slip condition $\mathbf{u} \cdot \hat{\mathbf{z}} = 0$ at $r = L$ (or $x \in W$).

$$\begin{aligned} & [\kappa\phi J_0(\kappa L) + \xi\psi J_0(\xi L)e^{\alpha t}] e^{\kappa z} = 0, \\ \psi e^{\alpha t} &= -\frac{\kappa J_0(\kappa L)}{\xi J_0(\xi L)} \phi. \end{aligned} \quad (2.66)$$

As ϕ is the only function on the right hand side it can be approximated by the (complex) exponential of the rotational flow. As we know from Mathieu analysis there often is a single dominant frequency component in solution for ϕ . However, the boundary layer will influence the potential in turn because it contributes to the mechanical energy equation, eq.(2.44). Also, a Fourier expansion can be made where α is restricted by the allowed values for ξ . In most cases $\alpha/\nu \gg \kappa^2$ and $\alpha \approx i\Omega$ such that the boundary layer wavenumber in the lowest order is $\xi \approx (1+i)\sqrt{\Omega/2\nu}$. Five times the real part of the reciprocal is about 1.4mm for water and $L = 54mm$, see figure 2.10. This is indeed a real boundary layer as it is very small, although innegligible.

As shown in section 2.2.3 another inconsistency with potential flow is that it allows viscous stresses along the free surface. Since the fluid has more inertia than the surrounding air, one can expect a boundary layer of air and liquid surrounding the interface matching the interfacial stresses [13, 14]. We show that the layer is save to neglect by examining a fluid boundary layer solely meeting

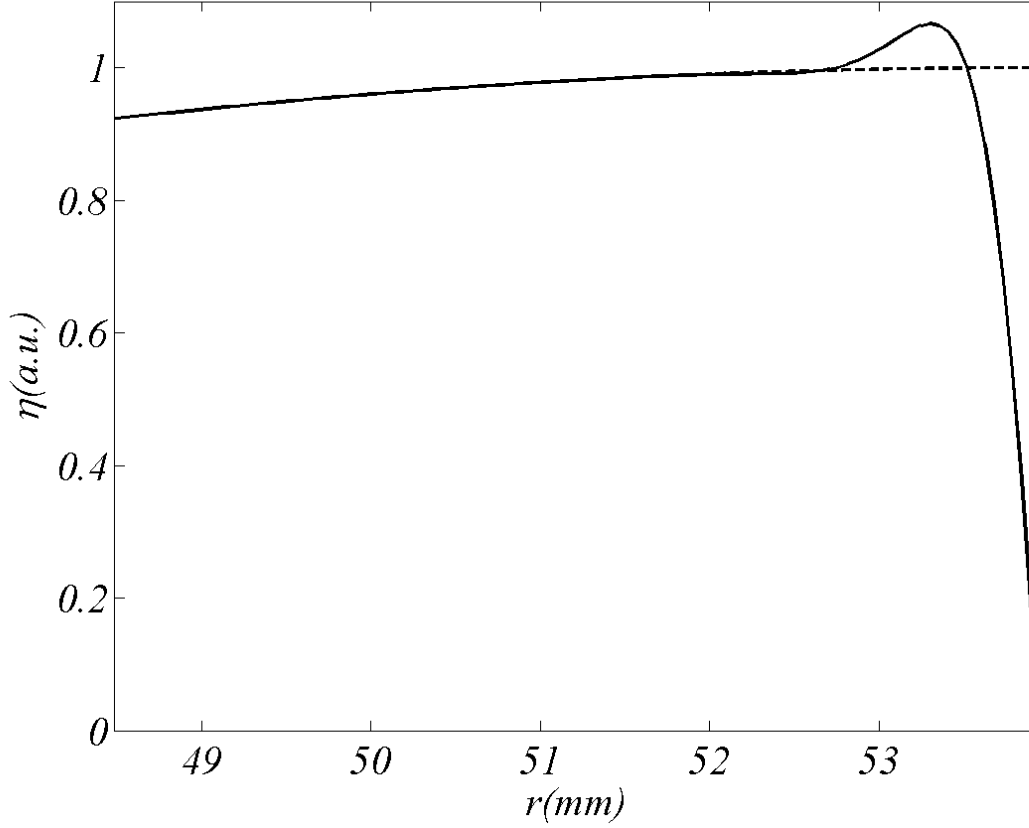


Figure 2.10: Surface profiles for the (0,1) mode close to the wall; Airy profile (dotted) and with wall boundary layer correction in the lowest order (solid). The right edge represents the wall.

the stresses as if the fluid was in a vacuum. Again we start with the rotational flow from eq.(2.64) but we take $\xi = \kappa$ to have the same radial dependence as the irrotational flow. It follows $\zeta \approx (1 + i)\sqrt{\Omega/2\nu}$. For infinitesimal surface elevations eq.(2.33) yields

$$0 = \frac{1}{\nu} \hat{\mathbf{n}} \cdot \boldsymbol{\tau} \cdot \hat{\mathbf{t}} \approx \left[\frac{\partial(\mathbf{u} \cdot \hat{\mathbf{r}})}{\partial z} + \frac{\partial(\mathbf{u} \cdot \hat{\mathbf{z}})}{\partial r} \right]_{z=0} \quad (2.67)$$

$$= -C J_1(\kappa r) [2\kappa^2 \phi e^{\kappa z} + (\kappa^2 + \zeta^2) \psi e^{\alpha t + \zeta z}]_{z=0} \quad (2.68)$$

$$\Rightarrow \psi e^{\alpha t} = \frac{-2\phi}{1 + \left(\frac{\zeta}{\kappa}\right)^2} \quad (2.69)$$

ζ/κ is of order 10^3 so ψ is very small compared to bulk flow, hence the surface dissipation can be neglected compared to the kinetic energy.

2.2.8 Meniscus Waves

The boundary layers make sure the stresses are in balance. Most notably is the no-slip condition implying the vertical velocity at the wall is zero. However, this also suggests that the surface is always pinned at the contact line Γ . From experiments we observe that this is not always the case and that the fluid slips over the cylinder. Its effect is assumed to act on a very small scale such that the irrotational flow of the bulk is still a good approximation.

First we have to give a more accurate description of the steady state of the system. In section 2.2.5 we found the (0,0)-state or solid body state. This state is not entirely flat because close to the walls surface tension forces may counter gravity and a meniscus is formed [22]. Its profile can be calculated in many ways but here we use the zero velocity field to find that all contributions to the mechanical energy (eq.(2.44)) are zero as well. Without forcing the conservative term (eq.(2.40)) has a homogeneous solution as well, $gz + \bar{\gamma}k = 0$ at the surface, which is a second order differential equation. We use η again as the parameterization and express the curvature in its derivatives $\partial_r \eta = \eta'$. One defines the capillary length $\lambda_c^2 \equiv \bar{\gamma}g^{-1}$, then in the cylindrical symmetric case

$$\eta = \lambda_c^2 r^{-1} \left(\frac{r\eta'}{\sqrt{1 + \eta'^2}} \right)', \quad (2.70)$$

by eq.(2.24). Note that this can be considerably different from Cartesian coordinates. For symmetric surface elevations the second curvature is automatically accounted for, because the surface is always parallel (no curvature) to $\hat{\theta}$. The boundary conditions are that $\eta' = 0$ far away from the wall and that $\tan \alpha_E = \eta'$ at the wall. The latter condition is due to the wettability of the material, e.g. water on a perspex surface has a contact angle of 70.9° resulting in $\alpha_E = 0.11\pi$ (difference of $\pi/2$). The entire meniscus curve can also be described in angles, e.g. $\eta'(1 + \eta'^2)^{-1/2} = \sin \alpha$. Linear solutions of eq.(2.70) are

$$\eta = aI_0 \left(\frac{r}{\lambda_c} \right), \quad (2.71)$$

with I_n the n^{th} modified Bessel function of the first kind. Objects with a greater density than a liquid may still float in it, due to the forces originating from the local meniscus profile around the object. Several floating objects may have mutual attraction or repulsion due to the local curved surface. This is known as the Cheerios effect [90]. The constant is $a = \lambda_c \tan \alpha_E / I_1(L/\lambda_c)$ such that the contact angle at the wall is met, see figure 2.11. Since the amplitudes for meniscus waves are expected to be small, we use a linear approach in the remainder of this section.

The contact angle can be calculated from a force balance of the contact line. For most surfaces this value is not unique. The contact angle of a pinned contact angle may vary in a limited range, which can be related to microscopic structures in the solid wall [76, 22]. The limits are the advancing and receding angles, such that $\alpha(L) \in [\alpha_A, \alpha_R]$, which is a well defined interval in normal circumstances. We hypothesize that the angle is dynamic and varies within this interval when the system is weakly forced. This is because waves are generated

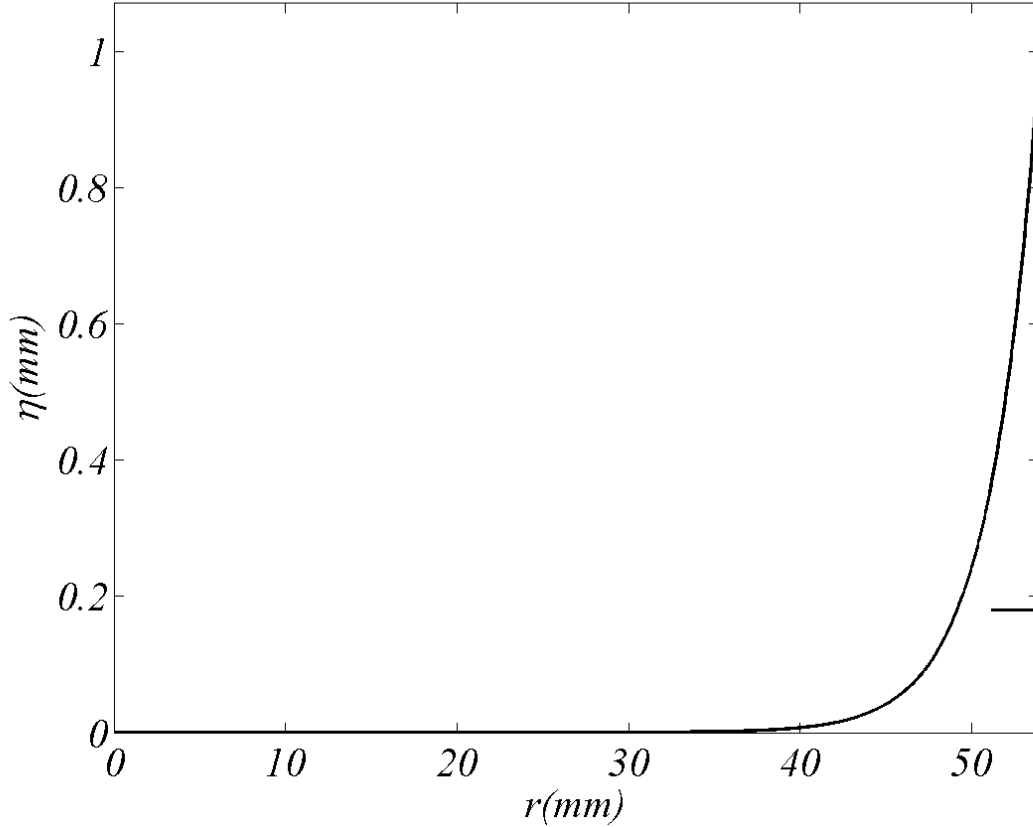


Figure 2.11: Meniscus for water on perspex from eq.(2.71). The length of the bar is λ_c and the relative difference with eq.(2.70) is less than 1%.

at the meniscus. When the cylinder moves upwards (downwards) the gravity is effectively larger (smaller), due to the acceleration of the container and the meniscus becomes steeper (more gradual). A surface wave is created because of continuity, which is consequently at the frequency of the excitation. This was observed by Douady [30], although he did not assume the contact line was pinned in his analysis.

Due to the forcing, there actually is a varying capillary length

$$\bar{\lambda}_c^{-1} = \frac{\bar{g}}{\bar{\gamma}} = \lambda_c^{-1} (1 - f \cos \omega_0 t). \quad (2.72)$$

Eq.(2.70) still is the homogeneous solution for $\bar{\lambda}_c$, but there now is a dynamic part leading to a traveling wave equation, which we will denote as meniscus waves. Dynamically, the meniscus waves are generated because of the kinematic coupling (eq.(2.26)). There are however some discrepancies with a traveling solution as they are combinations of Bessel functions of the first and second kind, so-called Hankel functions [11]. The second kind part goes to infinity at

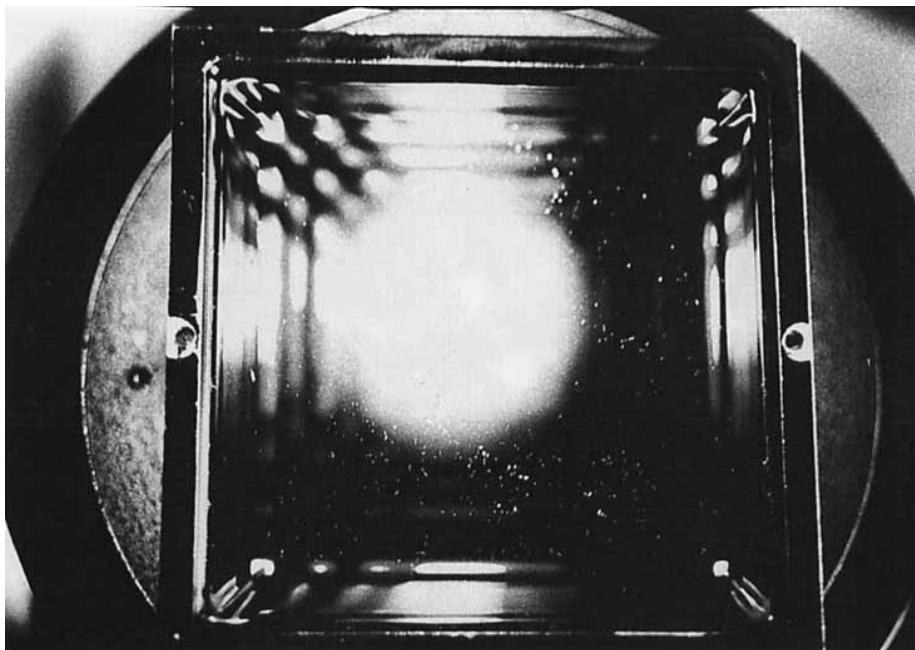


Figure 2.12: Meniscus waves in a square container of $80 \times 80 \text{mm}^2$ filled with 2mm of silicon oil taken from [30]. The driving frequency was 20Hz such that isochronous waves have an expected wavelength of one twelfth of the length, which is in good agreement.

the origin which is unphysical. This cannot be countered by for instance surface tension, because the profile is a solution of the separated Laplace equation (eq.(2.49)). If we were not to violate volume conservation and incompressibility we have to allow a very sophisticated flow field preventing the singularity at the origin. On the other hand, appropriate standing waves fulfill the incompressibility condition automatically. There already is a required anti-node in the center since the traveling waves generated at the wall always meet in the center with the same phase. In fact, when the wave reaches the opposite wall, it interferes with the meniscus motion such that there are also anti-nodes at the wall. A boundary layer makes sure the contact line is pinned. With this in mind the profile is split into the homogeneous meniscus (eq.(2.71) for $\bar{\lambda}_c$), a profile corresponding to the irrational flow (eq.(2.56) for $s = 0$) and one corresponding to an appropriate boundary layer or in formula $\eta = \eta_m + \eta_d + \eta_b$ respectively. We pin the contact line by requiring

$$0 = \partial_t \eta_m(t, L) = \partial_t \left(a(t) I_0 \left(\frac{L}{\bar{\lambda}_c(t)} \right) \right), \quad (2.73)$$

$$0 = \eta_d(t, L) + \eta_b(t, L). \quad (2.74)$$

Since a has to be a function of time, there is a restriction on the contact angle, which did not have an explicit constraint on its derivative yet.

This discussion shows that the profile near the wall can be very complicated.

One way of solving this system is to calculate the mechanical energy for the separated flow field and yield differential equations for the contact angle and the profiles, where η_d will approximate the surface away from the wall. However, the most important question is when the system transitions to a real standing wave state. When are the meniscus waves too large for the contact angle to be outside its allowed interval? The exact dynamics of this 'solid body' state are of minor interest and we will assume that the system will eventually develop in a standing wave state where Airy waves with appropriate boundary layers suffice. However, there is a large difference with Mathieu forcing, because there are now terms in the mechanical energy depending on the meniscus profile, which now acts as a classical driving force for oscillators. This corresponds to the qualitative description mentioned earlier that the meniscus generates waves due to parametric oscillation. The fact that the meniscus is a wavemaker changes a lot; the solution will be forced to follow the excitation which is different from Mathieu theory which may result in solutions with other temporal dependences.

Let us assume that the mechanical energy with the Airy approach leads to a temporal differential equation that can be split in a Mathieu part and a part behaving as a forced harmonic oscillator. The response of the second part is isochronous, i.e. of the same frequency as the excitation, and depends on how close the driving frequency is to eigenfrequency of the system given by the dispersion relation (eq.(2.62)). Note that the responses of both parts can both be significant. Most interestingly are isochronous Faraday waves which are found around $p = 4$, which one can particularly expect in large rectangular systems. For standing waves $\Omega^2 \approx \kappa g$ with wavenumbers $\kappa = 2\pi n L^{-1}$ for integer n . Assume $\kappa = \kappa_0$ is a period doubled Faraday wave ($p = 1$) then $\kappa = 4\kappa_0$ leads to $p = 4$ while the corresponding dispersion equals the driving frequency.

2.2.9 Wetting effects

When the contact angle exceeds the allowed interval, the fluid tends to slip over the wall. The direction in which this happens is a priori unknown, but one can think of a flow field that moves over solid interfaces without 'real' slipping. Like caterpillar tracks there never will be tangential velocities at the wall and perpendicular flow corresponds to deposition or extraction of fluid particles from the wall. The complications this flow has on a molecular scale are immense, but we think this is a nice visualization. Real slipping of fluids on interfaces is studied in for instance [45].

In our setup the fluid will move up against the wall eventually and wet an area proportional to the amplitude of the wave. The exact dynamics are complicated and beyond the scope of this study. However, in a macroscopic setting the dynamic contact angle (α) results in a kinematic force per unit length given by $\bar{\gamma}(\sin \alpha - \sin \alpha_E)$ [76, 22]. As the length of the contact line for symmetric motion always equals the circumference this force equals

$$F_{\Gamma}(\alpha) = 2\pi L \bar{\gamma}(\sin \alpha - \sin \alpha_E). \quad (2.75)$$

Microscopically it will not act on a line but on a small volume and determine the shape of the fluid and wall on this scale. We assume that the energy needed for the contact line to move against this force comes from the fluid's mechanical energy. We expect that the angle equals the advancing angle while wetting the wall, because the line does not have to move when the angle is in its allowed interval again ($\alpha \in [\alpha_A, \alpha_R]$). It appears that the contact angle is actually velocity depended for slipping lines, but the critical speed when α_A is reached is very small, c.q. order of mm/s [69]. The energy needed for the fluid to move up to height h is now approximated by

$$E_\Gamma = F_\Gamma(\alpha_A)h. \quad (2.76)$$

It gives rise to hysteresis in the transition from solid-body to standing wave states. Assuming the amplitudes for standing waves are so large that the contact line cannot be pinned the system has to 'invest' energy to wet the walls whereas this is not the case in the transition to the solid-body state. There is also an energy loss involved when the amplitude grows. Moreover, this description supports the pinned contact angle for meniscus waves in the solid-body state.

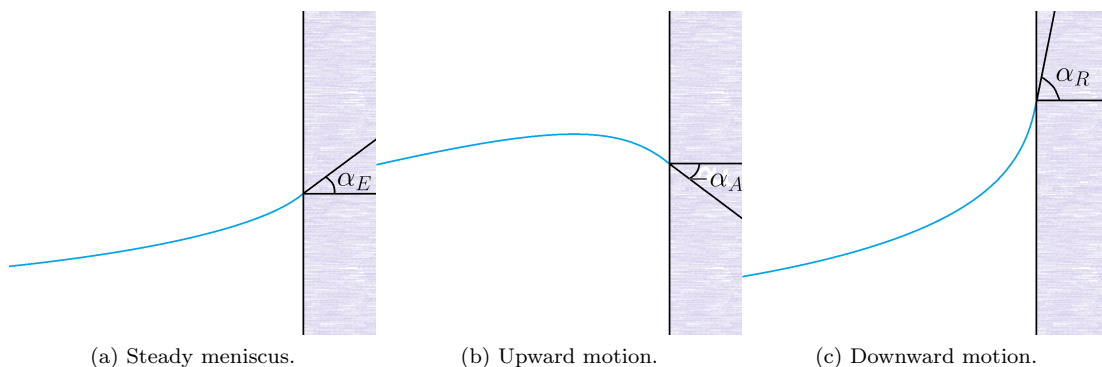


Figure 2.13: Schematic surface profiles (blue) in a full slip model. The shapes and angles are not proportional to the setup.

We investigated two possibilities for the contact line movement when the fluid moves downward. We will first base a model on the restriction that the contact line moves with the fluid, which is denoted as the full-slip model. If the contact line is pinned at its new height a thin film will be deposited on the container wall. We will briefly treat the dynamics of thin films by comparing the system to plates that are pulled and withdrawn from a liquid reservoir. Finally, we will propose modifications to this model such that it is better applicable to our system.

Following our discussion the natural assumption is that the contact angle equals the receding angle in downward motion, leading to the force $F_\Gamma(\alpha_R)$, see figure 2.13. Miles calculated the dissipation in such a system by assuming the velocity at the contact line is given by the potential bulk flow [69]. The contact angle changes instantaneously from advancing to receding angles and vice

versa if the sign of the velocity changes. The vertical velocity at the wall is $w(t) = \partial_z \Phi(t, L, \eta)$. The force is averaged as

$$\bar{F}_\Gamma = \frac{F_\Gamma(\alpha_R) - F_\Gamma(\alpha_A)}{2} \text{sgn}(w) = 2\pi LC\bar{\gamma} \text{sgn}(w), \quad (2.77)$$

where the constant C only depends on the advancing and receding angles, e.g. $C = 0.31$ for water on perspex. The power absorbed from the mechanical energy is the velocity of the contact line times this force.

$$P_\Gamma = \bar{F}_\Gamma w = 2\pi LC\bar{\gamma} |w| \quad (2.78)$$

This dissipative power has to be added to eq.(2.44), i.e. $\partial_t K + P_C + P_D + P_\Gamma = 0$. In contrast to the other mechanical power terms this dissipation is not proportional to a square of the velocities which means P_Γ is amplitude depended. In fact, we can recalculate the Airy result (eq.(2.61)) including this term. Then $w = \partial_z \Phi(t, L, 0) = \sqrt{2}L^{-1}\dot{\phi}$ and $\text{sgn}(w) = \text{sgn}(\dot{\phi})$ resulting in

$$2\pi\dot{\phi} \left(\kappa\dot{\phi} + \bar{\Omega}^2 T + 4\nu\kappa^3\dot{\phi} + \sqrt{2}C\bar{\gamma}\text{sgn}(\dot{\phi}) \right) = 0. \quad (2.79)$$

In a period averaged evaluation of the friction terms one has to group all dissipative terms with $\dot{\phi}$ and the prefactor determines the damping coefficient, e.g. $4\nu\kappa^3$ (also see section 2.1). When dividing $\dot{\phi}$ from the contact line term one finds $\text{sgn}(\dot{\phi})\dot{\phi}^{-1} = |\dot{\phi}|^{-1}$. Hence, one finds that the contribution of the contact line is inversely proportional to the amplitude of the motion. This potentially leads to very large dissipation. For very small velocities, when the contact angle varies continuously with the line velocity, this is of course not the case and the model should be modified accordingly. Also, the contact line dissipation becomes more dominant for smaller containers, as they have a relatively larger circumference. Keulegan commented on both issues, "With a liquid not wetting the walls [...] losses from surface activity, of some obscure origin, outweigh many times the losses due to viscosity in the basins of smaller sizes" [53].

Many of our experiments show that the fluid wetting the wall does not follow the bulk flow and a thin film remains on the wall. Gravity incites drainage of the film but this is slowed down by significant viscous forces because of the small length scales.⁵ If the contact line moves downward slowly there is only a small distance for the contact line force to act on. This results in considerably smaller dissipation than in the full slip model. With this in mind, we have to look for models predicting the contact line velocity and describing the dissipation in these layers.

First of all we have to note that contact line velocities are not easily estimated from system parameters. The velocity of the layer of liquid molecules adjacent to the wall is proportional to the velocity gradient at the wall times a slip length, which is generally of the order of a few molecule sizes [26]. The difficulty lays in matching the microscopic profile to the macroscopic flow.

Liquid moving down a solid wall can be transformed to a problem where a flat

⁵This also implies that we have to wait long enough in between experiments for the film to drain.

plate is pulled out of a liquid, which is intensively studied [49, 58, 27, 24, 82]. More recently, Maleki et al. experimented with a plate that is first pulled out and subsequently pushed into a liquid [64]. The approach generally consists out of two parts; the assumption that the layer is very small such that a Poiseuille ansatz can be made and an estimation of the contributions in the Navier-Stokes equation which leads to a balance between dominant forces.⁶ De Ryck and Quéré published a detailed overview of the regimes involved in a plate withdrawn at velocity W [24]. In a two-dimensional system (y, z) , with y the distance from the wall, the velocity is approximated by $\mathbf{u} = [0, w(t, y)]$, since the layer is assumed small such that the horizontal velocity and the vertical derivatives in the film can be neglected. Navier-Stokes leads to a balance of viscous forces ($\nu\partial_{yy}w$) with inertial and pressure terms that do not depend on y . The boundary conditions are no-slip at the wall and no stress at the free surface (eq.(2.28)). Since the film is almost flat, there is a horizontal normal vector, the latter is approximated by $\partial_y w = 0$, such that

$$w \sim \frac{\frac{1}{2}y^2 - ye}{\nu}, \quad (2.80)$$

where the surface is parametrized by $y - e = 0$.

The dimensionless numbers involved are the capillary (Ca) and Reynolds (Re) numbers,

$$\text{Ca} = \frac{\mu W}{\gamma} = \frac{\nu W}{\tilde{\gamma}}, \quad (2.81)$$

$$F = \frac{1}{\mu^2} \sqrt{\frac{\rho\gamma^3}{g}} = \frac{1}{\nu^2} \sqrt{\frac{\tilde{\gamma}^3}{g}}, \quad (2.82)$$

where $\text{Re} = F\text{Ca}^{5/3}$. A negative capillary number corresponds to downward motion of the plate, but we will first limit the description to positive capillary numbers. When Reynolds is small and $\text{Ca} < 10^{-3}$ we are in the visco-capillary regime and the film thickness is proportional to $\text{Ca}^{2/3}$. The prefactor can be found by matching the profile to the static meniscus, which is known as the Landau-Levich-Derjaguin (LLD) solution. The visco-gravitational regime is for $\text{Ca} > 10^3$ when gravity drains the film, the horizontal position of the surface scales as $\sqrt{-\nu z/gt}$ with maximum thickness

$$e = \lambda_c \text{Ca}^{1/2} = \sqrt{\frac{\nu W}{g}}. \quad (2.83)$$

The crossover regime between both described concerns six decades. Interpolation is suggested such that the thickness gradually goes from a 2/3 to a 1/2 power law as the capillary number increases. For a Reynolds number of order unity inertial effects are considered, but this leads to very cumbersome equations without a clear relation for the thickness as function of the system's parameters. In figure 2.14 one observes it causes thickening of the film which should be compared with eq.(2.83).

⁶In a sense the potential flow was a comparison between inertia and pressure, while rotational flow compared inertia and viscosity, which we encountered in sections 2.2.5 and 2.2.7.

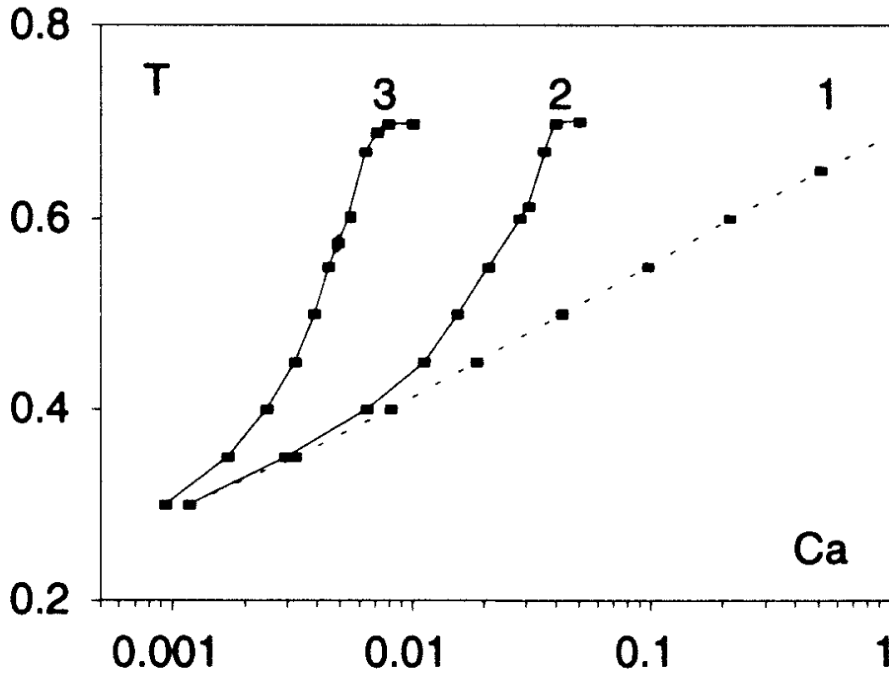


Figure 2.14: Thickness parameter $T = e\lambda_c^{-1}Ca^{-1/2}$ as a function of the capillary number in the inertial regime for $F = 0$ (1), $F = 10^4$ (2, alkane) and $F = 2.10^5$ (3, pure water) taken from [24].

In our experiments we consider pure water ($F = 2.10^5$) and sunflower oil ($F = 27$). The characteristic velocity is estimated as the maximum vertical velocity of the potential flow at the wall like in the slip model. Assuming the maximum elevation in the middle is the reciprocal of the wave number and we are exiting the system at $p = 1$ for the (0,1) state (2.2.5) we approximate $|W| \leq J_0(\kappa L)\omega_0/2\kappa \approx 0.15m/s$. This results in $|Ca| \leq 2.10^{-3}$, $|Ca| \leq 2.10^{-1}$ and $|Re| \leq 6.6$, $|Re| \leq 2.0$ for water and sunflower oil respectively. Maleki et al. report the surface remains smooth (no bumps or so) for small downward velocities of the plate, i.e. $-1 < Ca < 0$ [64]. Since we meet this requirement we find film thicknesses of $5.10^{-5}m$ and $5.10^{-4}m$ using the trend in figure 2.14.

We can now estimate the slip velocity of the contact line. The velocity gradient at the wall scales $\partial_y w \sim e/\nu$ by eq.(2.80) which is of order 10^1s^{-1} . In the visco-gravitational regime the prefactor is g ([24]) but multiplied by a slip length of order $10^{-9}m$, the length of a few molecules, we find a speed of order $10^{-7}m/s$. This model predicts the contact line is practically fixed, although it seems an underestimation. Experimental observation have to be conclusive whether the contact line is pinned compared to the interval of one period of the fluid motion.

In estimating the dissipation in this layer we use eq.(2.43). Since the horizontal velocity is small we omit the second term. We assume the height of the

layer varies between the irrotational flow and the fixed contact line at $z = h$, such that the domain is $0 \leq y \leq e$, $\eta(t, L) \leq z \leq h$ and $W = \partial_t \eta$. We use eq.(2.80) with again g as a prefactor and assume the thickness does not vary much over time because of the small period of oscillation.

$$\begin{aligned} P_{\Gamma} &= \nu \int_{\eta}^h \int_0^e (\partial_y w)^2 dy dz = \int_{\eta}^h \frac{g^2 e^3}{3\nu} dz \approx \frac{e^3}{3\nu} (h - \eta) \\ &\approx \sqrt{g\nu} (\partial_t \eta)^{3/2} \frac{h - \eta}{3}. \end{aligned} \quad (2.84)$$

In the vertical integration we used a steady homogeneous thickness without the prefactor that we used to determine the thickness earlier. Maleki et al. find a difference in the profile for upward or downward motion, but we think this integration is a good approximation since the flow profile (eq.(2.80)) does not change. It is because of two things; first we want to compare the nature of this dissipation with the slip model, eq.(2.78). The difference is the velocity exponent, the origin (surface tension or gravity and viscosity) and the dependence on time. Period averaged the amplitude goes with exponent 5/2 such that this dissipation is proportional to the square root of the amplitude in an Airy approach compared to the inversely proportionality in eq.(2.79).

Secondly, we have to point out the many discrepancies of this plate model with our setup. The relations involving plate withdrawal are based on boundary conditions assure a smooth coupling between the film and the static meniscus. However, in our setup we have to match the film with a moving fluid, subject to parametric oscillating gravity, while even the boundary layer is a few orders of magnitude thicker than the film, by comparing eq.(2.83) to eq.(2.66). Probably a correction for the film is not realistic enough and we have to find a new boundary layer for appropriate boundary conditions at the wall and surface. Finally, we doubt whether the dissipation inside the film decreases the mechanical energy of the fluid, because the bulk fluid is relatively far away while the field inside the layer is dissipative. This is contrast to the slip model where it is clear the fluid has to overcome the corresponding forces. Moreover, it is strange that the dissipation depends on terms related to surface tension and gravity when it only depends on the vorticity if the normal velocity of the surface is negligible due to eq.(2.43). In plate withdrawal the corresponding forces can require work done by the system, but in our system the flow field is similar over one period.

We propose a third model that is motivated by this discussion. Since we are only interested in the relevant dissipation for the bulk flow and the argument that it only depends on vorticity we look for the rotational part of the flow in the film. The decoupling of the flow is by eq.(2.46) and the equation of motion is the same as for the boundary layers, eq.(2.64). Surface tension and gravity are indeed not involved while inertia and temporal dependence is. We impose a pinned contact line with a no-slip condition over the entire wetted wall. The solution is straight-forward; we add a steady profile to the surface elevation like a meniscus. That it is stationary is not inconsistent since it are conservative forces that incite the drainage of film. In the solid-body state (like figure 2.10) the contact line was pinned at $z = 0$, but here we 'lift' the entire boundary layer to the new contact line. In fact both the boundary layer and the thin

film have the same no slip boundary condition, so it is natural to see combine them is one flow field. In figure 2.15 the surface elevation η for a harmonic motion of the (0,1) state is plotted for several instances. The profile is a sum of the irrotational bulk flow, wall boundary layer (eq.(2.66)) and a static film, in this case equal to the wall boundary layer at its maximum elevation. This

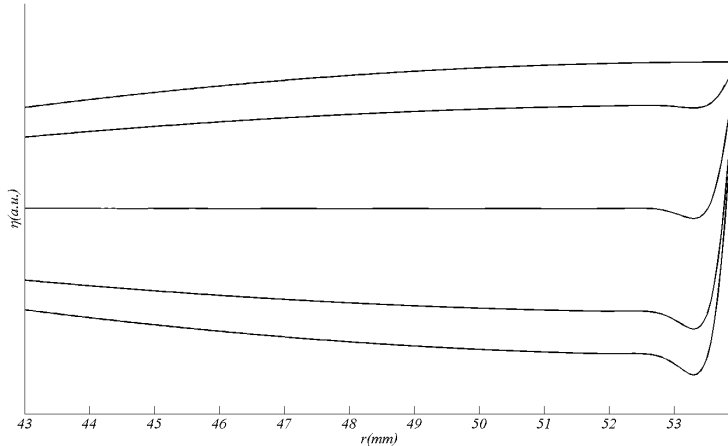


Figure 2.15: Several surface elevations close to the wall ($L = 53.9\text{mm}$).

model meets all required conditions, a smooth transition to the bulk flow and boundary layer, a pinned contact line, but it suggests that only a small amount of dissipation is involved, namely the contribution of the elevated part of the boundary layer. This might be an oversimplification. On the other hand we argued that dissipation in the film is probably not relevant for the main fluid motion. Dissipation analysis of fluid motion in containers without accounting for the contribution from the film show good agreement with experiments [68]. Other problems are that the boundary layer is much thicker than the expected real film thickness at some locations and that the film is only drained when the bulk motion is downward.

2.3 Cavities and Jets

Free surface interfaces are not necessary smooth. Especially at larger amplitudes they can become unstable, like ocean waves breaking as they approach a beach. Processes like air entrapment, foam creation and modification of the bottom show that wave-breaking is of a violent nature. In the standing wave case troughs and crests will become cavities and jets for larger amplitudes. Certain Mathieu's solutions grow uninhibitedly which motivates the investigation into the dynamics for larger surface waves. In fact, Faraday systems are often associated with jets. In this section we will first give an introduction with a qualitative description of cavities and jets. Next we will give examples of cavities in other systems and look for similarities. We treat solution offered, both analytical as numerical and go into the relation of jetting in relation with the solid and standing wave states.

2.3.1 Introduction

In the case of standing waves a deep trough can be formed that does not move upward 'normally' to form a crest. These unstable troughs are usually denoted as cavities. It collapses, i.e. the free surface moves radially inward faster than vertically upward, such that it connects with itself over the depth of the cavity. However, this contradicts the continuity requirement in the exact center and a singularity is formed. In a very short time scale the radial inertia has to be converted in the vertical direction, which is now concentrated in a small volume. This part of the fluid will move very fast in a thin, needle shape; the jet. The direction of the jet is upward in general but there are cases that the cavity closes and creates an entrapped air-bubble under the surface. This is called a cavity pinch-off. A second jet originates from the top of the bubble directed downward and it will penetrate the entire bubble if strong enough, creating a donut-like vortex ring.

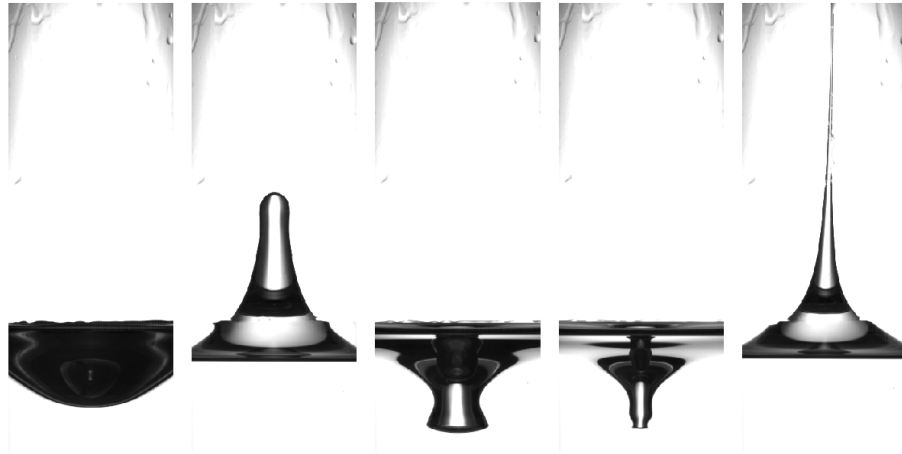


Figure 2.16: From left to right: a trough, crest, cavity, its collapse and a jet in sunflower oil. The relative timing is [0, 131, 265, 271, 369]ms and the driving frequency was 8.303Hz.

Any hole in a surface is unstable when the restoring force is gravity, but it depends on the inertia and geometry whether this leads to a jet or a wave. For jet formation the side walls have to move inward and meet before the upward motion prevents this. One of the ways a jet can form is when a submerged bubble rises and forms an open cavity upon coalescence with air [61, 9]. It is like instantaneously introducing a concave surface. Jets are also created when a fluid moves upward in a cylindrical tube that is partly submerged in the fluid [23, 62]. These tubular jets are however not always preceded by cavities. Another method is when a test tube falls on a solid surface due to gravity. Upon impact a jet is formed but only when the surface was initially curved [2]. A cavity is always created by forcing the bottom to move downward, e.g. by the impact of a solid object on the surface. Everyone is familiar with the cannonball dive in a swimming pool ⁷ and it is well known subject in fluid physics

⁷'Bommetje' in Dutch.

[43, 42, 41, 40]. This will always result in a pinch-off about halfway down the cavity with jets in both directions. Liquid impact, like drops or other jets, on the surface can create open cavities without pinch-off [44]. Both impact methods can also result in eruptions, like crown like shapes [48, 78]. Examples of jetting methods without any cavity collapse are shockwave impact on a surface, the expansion of laser-induced vapor bubbles or ink-jet printing.

The main difference between the above examples and a Faraday setup is the transition from wave to cavity in the latter. The triggering mechanisms in above systems is better controlled and the jet follows almost immediately. The time scales are very different in our setup. The system can be in a wave state for a long time while the dynamics of a single cavity with a jet is about one period. Therefore the exact jetting location is much harder to predict as well.

The specific singularities in Faraday systems is also associated with self-focusing. The entire system is driven but the fluid itself focuses most of its inertia in contrast with diffusive processes which are more common in nature [47]. Faraday excitation in a flat container show less focusing effects, e.g. [2]. We would like to stress that jetting is still free surface dynamics and the equations of motion found earlier still apply. That is up to topological changes, like bubble and droplet creation. Some equations can be simplified, as there is not enough time for some forces to have significant effects. On the other hand, the closure of the cavity can be accompanied by inneglegible air flow [43, 40].

2.3.2 Similarity solutions

Singularities are often associated with similarity solutions, i.e. all solutions are similar to each other in a particular way. Barenblatt showed for a function of interest $F(x, y)$

$$\lim_{x \rightarrow 0} x^{-\alpha} F(x, y) = f(y), \quad (2.85)$$

with constant exponent α [5]. Physically, the variables need to be dimensionless. If $f(y)$ exists, is finite and nonzero than we may write $F(x, y) = x^\alpha f(y) + \mathcal{O}(x^\alpha)$. This is a similarity condition of the first kind. \mathcal{O} , the quantity of order t^α , is dropped close to the singularity. To apply this relation to equations all variables should first be made dimensionless for a free use of exponents and we need to make sure we are indeed close to the singularity to apply eq.(2.85). Compared to the dimensional original coordinates (t, r, θ, z) the new coordinates (t', r', θ, z') are scaled by characteristic time and length scales while the singularity occurs at $(0, 0, \theta, 0)$. The azimuthal does not change as we will evaluate cylindrical symmetric systems.

Zeff et al. proposed a potential flow neglecting all viscous and gravitational forces in a Faraday setup. There are three equations describing this system; Laplace equation for the potential, the vertical parameterization of the kinematic boundary condition (eq.(2.26)) and Bernoulli's equation (the potential

part of eq.(2.63)).

$$\nabla^2\Phi = 0, \quad (2.86)$$

$$\partial_t\eta + \partial_r\Phi\partial_r\eta - \partial_z\Phi = 0, \quad (2.87)$$

$$\partial_t\Phi + \frac{1}{2}|\nabla\Phi|^2 + \bar{\gamma}k = 0. \quad (2.88)$$

Now we actually need more than two exponents to prevent an overdetermined system. We write $\eta(t', r') = \eta'(t', r't'^\beta)$ for another exponent β . The same method is applied to the potential such that we can apply eq.(2.85) for smooth functions χ and Ψ .

$$\eta(t', r') = t'^\alpha\chi(r't'^\beta), \quad (2.89)$$

$$\Phi(t', r', z') = t'^\epsilon\Psi(r't'^\beta, z't'^\delta), \quad (2.90)$$

where we find the values of the four exponents by substituting them in eq.(2.86)-(2.88) and requiring the same temporal dependence, resulting in $2/3 = \alpha = -\beta = 2\epsilon = -\delta$. These constants can also be found by dimensional analysis. Since the two forces are surface tension and inertia, the dimensionless potential and length are obtained after scaling by $\Phi_0 = (\bar{\gamma}^2t)^{1/3}$ and $\eta_0 = (\bar{\gamma}t^2)^{1/3}$ respectively [52]. By scaling Bernoulli's equation the surface tension changes to the reciprocal of the Weber number, which physically is the ratio between kinetic and surface energies.

$$\frac{1}{\text{We}} = \frac{\bar{\gamma}\eta_0}{\Phi_0^2} = 1.$$

This shows the Weber number is itself self-similar and that the ratio between surface tension and inertia is conserved in the singularity.

2.3.3 Other solutions

Hogrefe et al. proposed a method that does describe the transition from cavity to jet analytically [47]. They assumed the cavity shape directly before the singularity was cylindrical shaped, as in figure 2.16. This leads to the approximation that neglects any vertical velocity of the cylinder before the singularity, such that $\mathbf{u} = [-c/r', 0, 0]$ because of continuity. In here c is a positive constant, such that the cylinder wall collapses as $\zeta \sim \sqrt{-t'}$ (remember that t' is negative before the singularity). This velocity field blows up at $r' = 0$ which is repaired by assuming the radial changes to $-cr'/(1+r'^2)$, which goes to zero smoothly at $r' = 0$ and approximates the initial relation for large r' , so no other constants appear. The vertical velocity can be found by continuity and is approximately $2cz'$ around $r' = 0$. Although this leads to a strong vertical velocity in the center, there is no further argumentation why the velocity profile near the singularity should change as proposed.

Oğuz and Prosperetti used Green's third identity to find an implicit surface

integral for a potential flow [77].

$$\Phi = - \int_F (G \nabla \Phi - \Phi \nabla G) \cdot \hat{\mathbf{n}} dx,$$

with $4\pi G = -|x - x_F|^{-1}$ for all $x_F \in F$ and $x' \in \forall$. The relation becomes an integral of sources and dipoles

$$4\pi\Phi = \int_F \left(\frac{1}{|x - x_F|} \nabla \Phi - \Phi \nabla \frac{1}{|x - x_F|} \right) \cdot \hat{\mathbf{n}} dx_F.$$

Gekle et al. used this integral over a free surface in a cavity pinch-off after solid impact [42]. Close to the pinch-off the cavity can be seen as a shrinking cylinder, i.e. $\nabla \Phi \cdot \hat{\mathbf{n}} = \partial_t \zeta$ with $\zeta(t, z)$ the radial position of $x_F \in F$, such that a surface element is $dx_F = 2\pi \zeta d\zeta$. We neglect the dipole term and approximate $|x - x_F| = \sqrt{r^2 + (z - \zeta)^2}$ which modifies eq.(2.3.3) to

$$2\Phi = \int \frac{qd\zeta}{\sqrt{r^2 + (z - \zeta)^2}},$$

with $q(t, \zeta)$ a distribution of sinks. The integral still has to be handled with care as the surface splits in the moment of pinch-off. Also, the sink distribution is altered for more realistic results. Together with the kinematic boundary condition this leads to a coupled ordinary differential system. Integrals over an infinite interval are evaluated over a large cut-off length scales.

Eq.(2.3.3) can also be solved numerically which is nowadays known as the boundary integral method (BIM). The boundary is discretized and at every boundary grid point Φ or $\nabla \Phi \cdot \hat{\mathbf{n}}$ is known. At the free surface Bernoulli finds Φ while the normal derivative at solid surface is equal to the velocity of the boundary. The integral finds the unknown variable, but the factor of 4π is variable and depends on the concavity of the surface. Through the kinematic surface condition the velocity of the free surface is found, such that the grid points can be relocated after a certain number of time steps.

2.3.4 The jetting state

We already remarked that Faraday excitation needs considerable time to produce a jet. When our setup (chapter 3) is excited at a small and constant amplitude, some experiments remained in a solid body or standing wave state for more than hundred cycles before a jet occurred. If the amplitude is held constant or is slowly decreased jets will keep forming although it is hard to predict what exactly will happen, because the falling jet will impact on the surface and distort it in the process. If the effect of the impact is mild we can expect a continuous jetting state with jets on a regular interval. This will also happen if the impact destroys a surface profile of a standing wave. The system will repeat growing again until the cavity, followed by a jet and its impact. If we assume a dissipation which depends on the amplitude of the wave we can expect hysteresis in the transition from wave to jet as well. The waves grow because their amplitude is below the stable amplitude. If they can grow far enough beyond this value before dissipation keeps up, a cavity will form whereas a wave at its

stable amplitude stays in the standing wave state. On the other hand the jet impact might just alter the growing standing wave. For instance it may trigger lasting asymmetric motion, preventing normal growth of the waves.

2.3.5 Surface irregularities

Keller and Eggers separately proposed description of surface modes on jets [51, 37, 38]. In our system we can also expect capillary and meniscus waves, Rayleigh instabilities and other distortions of the free surface, like in figure 4.4. Their characteristic length is much smaller than the container radius such that their influence on the standing waves is small. The shape of the surface can still be altered significantly and may possibly be difficult to analyze. Especially in a low viscous fluids instabilities are to be expected. We also found small irregularities near large curvatures (figure 4.5), but which exact origin is unknown. They were also observed by Zeff et al. [95].

At the top of crest there can be a thickening which is also known as a type of Rayleigh instability. It can influence the cavity shape, because of the increase in curvature when it moves down. In the extreme case there is a pinch-off and a droplet will fall into the closing cavity. This can have an enormous effect on the jet.

Chapter 3

Experimental Aspects

Faraday waves are of complex nature and experiments are necessary to validate our model and hypotheses. In this chapter we will describe the experimental facilities and procedures. First the setup and its components is treated. A secondary setup, to measure the surface tension of a droplet in ambient air, is described as well. We did not perform experiments to confirm the viscosity of the fluids.

3.1 Setup

The main components of the experimental setup are the shaking apparatus, accelerometers, a high speed camera and a liquid in a perspex container. The setup is sketched in figure 3.1.

3.1.1 Components

The fluids considered are demineralized water and sunflower oil. Small volumes ($< 0.2\%$) of food dye can be added to the water for better contrast. Two long perspex cylinders and one rectangular perspex container are available. The height of the cylindrical containers is approximately $0.5m$ while the inner diameters are $L = 107, 90 \pm 0.05mm$ or $L = 108, 50 \pm 0.05mm$ respectively. The height of the fluid can be calculated from its volume which has a measurement uncertainty of 1% . The cylinder is sealed with a perspex lid to prevent evaporation, contamination or liquid escaping due to jetting. The fluid level was measured over time and its decrease was minimal, i.e. the droplets on the lid and wall explained most of the volume loss. It is mounted vertically on a vibration system, the shaker (TV 50301, Tira GMBH, Schalkau, Germany). Vertical placement of the shaker and the cylinder is obtained with the help of a spirit level. An accelerometer (Endevco 751-10, Meggit, Dorser, UK) is attached to the shaker mount and measures the vertical acceleration. It is mainly used in the internal feed-back loop of the apparatus to control its motion. It is also connected to an acquisition module (NI USB-4432, National Instruments Corporation, Austin, USA) although that connection is not drawn in the figure. All connectors to the module are standard BNC coaxial cables. Another accelerometer (Endevco 2228C, Meggit) obtains measurements for all three directions. It is attached to

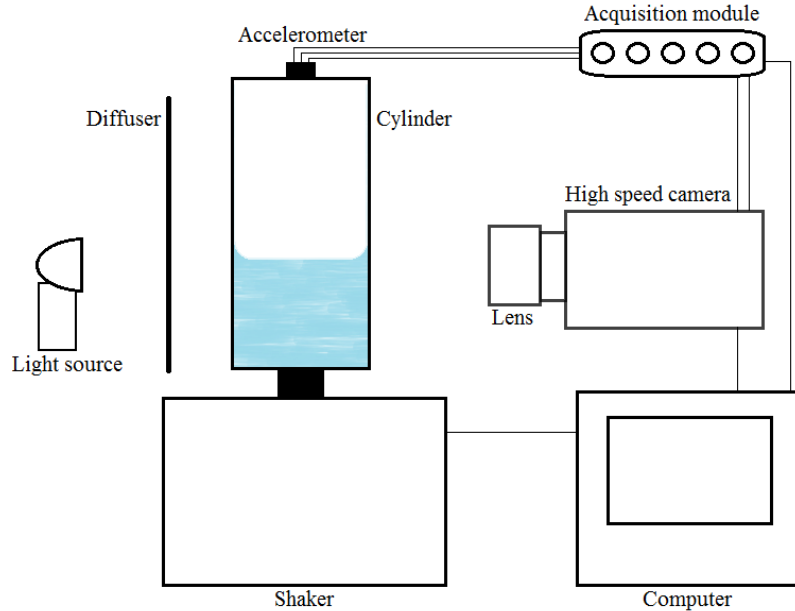
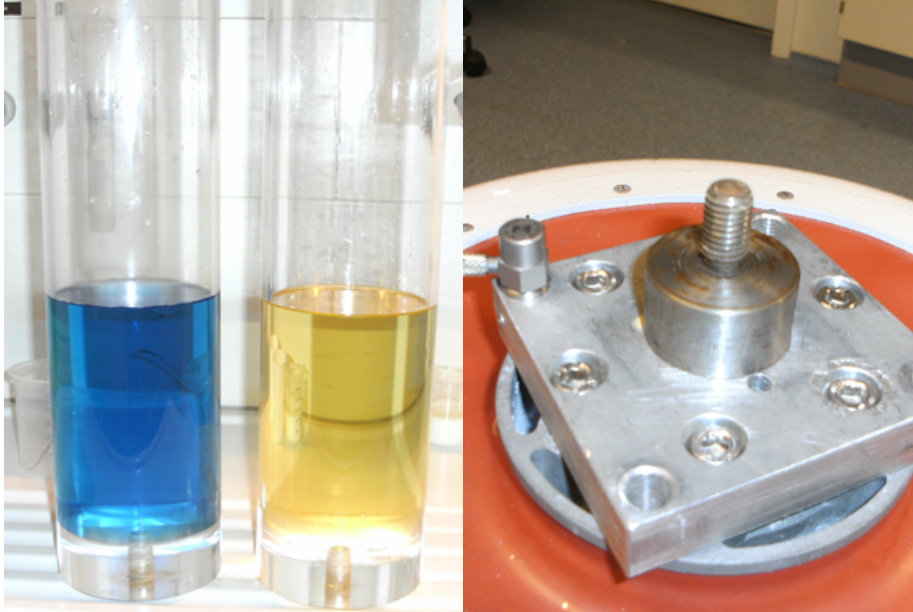


Figure 3.1: Schematic of the experimental setup. The thin lines represent data cables.

the lid and also connected to the module. The fluid dynamics are recorded by a high speed camera (Fastcam SA1.1, Photron Limited, Tokyo, Japan). The record trigger and exposure time of the camera are measured by the module on the same channel. The optics only consist of a 60mm lens (Makro-Planar T*, Carl Zeiss AG, Jena, Germany) which mounted on the camera. The light source consists of three xenon lamps (Mega Beam Xenon, Hella Inc., Peachtree City, USA) in front of a large diffusive plate. A computer downloads the data from the camera, shaker (via Ethernet connection) and the acquisition module (via USB connection) and is also able to give certain commands to these apparatuses.

3.1.2 Faraday excitation

The shaker is a high powered machine (up to 36A and 100V) with applications in (heavy) industry. The are four main parts, an exciter, an amplifier, the control equipment and the blowers. The control equipment sends a signal to the amplifier which drives the exciter in turn, see figure 3.3. In the exciter there is a field coil fixed to the casing and a vibrating coil that can move vertically. On top of this coil there is the armature table. It is shown in figure 3.2b with the cylinder mount and the 751-10 accelerometer attached to it. This accelerometer is connected with the control equipment which is used in a feedback loop. The



(a) Cylinders with 0.1% food dye solution (left) and sunflower oil. (b) Armature table with accelerometer and cylinder mount.

Figure 3.2: Components of the shaker.

blowers (not shown) prevent the machine from overheating.

It is important to realize the practical limitations of the mechanical motion. The system can be loaded with a maximum vertical weight of $350N$, has a maximum acceleration of $108g$ and its frequency range is $[2, 4000]Hz$. We are only close to the lower limit of the frequency range as our experiments are in the interval $[3, 12]Hz$. Also, the apparatus seems to have difficulties for small amplitudes with a limit at about $0.02g$. We can expect that the motion is less accurate near the edge of system's variables. Manually observed acceleration values as seen by the machine software differed up to 5% relative to the demand (i.e. desired acceleration). Furthermore the shaker has a tolerance for horizontal movements. This is precisely to prevent damage from horizontal forces on the exciter ($80N$ maximal). In case of a fluid these forces originate from non-axisymmetric motion, e.g. the slogging state (the (1,1) state in section 2.2.5). Finally, the response time of the shaker can be long (order of a period), because the motion is controlled by a feedback loop that is based on the frequency spectrum. If a signal with a varying amplitude is required, one has to take convolution and artifact effects into account.

To test the performance of the shaker we recorded the movement of an empty cylinder at $8.6Hz$. The acceleration was suddenly increased from $0.25g$ to $0.40g$.¹ The displacement is plotted in figure 3.4. One sees it takes approx-

¹Actually there are two sweeps in the software in this case. The first changes the frequency gradually from $8.59Hz$ to $8.60Hz$ at $0.25g$ and the second goes from $8.60Hz$ to $8.61Hz$ at

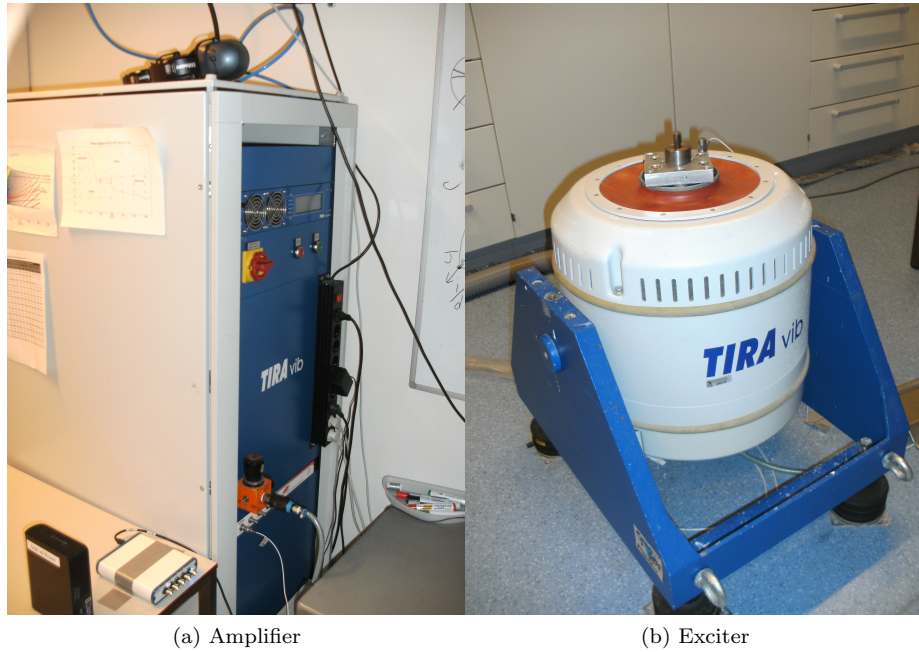


Figure 3.3: Components of the shaker.

imately 12 cycles (1.4s) for the amplitude to adapt. The temporal range was much larger than in the figure, from which we concluded the frequency was at least accurate up to approximately $0.1Hz$. The frequency settings can be specified up to μHz , so we assume the accuracy is much higher than this. The amplitude appears to be very accurate as well, although the spatial resolution is limited as can be seen from the plot. We cannot see the behavior at high amplitudes because we cannot change the amplitude fast enough or instantaneous in a zero-crossing. The fluid will always travel through a jetting regime before reaching the desired value. Because of the non perfectly vertical placement the jet will move asymmetrical counteracting succession jets.

To prevent undesired motions, e.g. in the horizontal direction, we make sure there is a lot of inertia, by using a large volume. The inertia of non-axisymmetric motion is then relatively small. This does of course limit the measurements to dispersively deep liquids. We have to make sure that the cylinders are still mostly filled with air otherwise the lid may act as a boundary for the air flow and in turn influence the fluid. Secondly, the measurements of the accelerometers are evaluated after every experiment and the experiment is discarded if they signal is not close enough to the demand. Figure 3.5 shows the excitation amplitude as a function of the camera time, while the left edge of the graph is the start of the run. It was set at $\omega_0 = 8.4Hz$, $f = 0.2$ with a 10s start up interval. The interval here is 9.03s and it is normal that the machine is off $0.40g$. This should instantly change the amplitude, since the levels only require the frequency to be continuous.

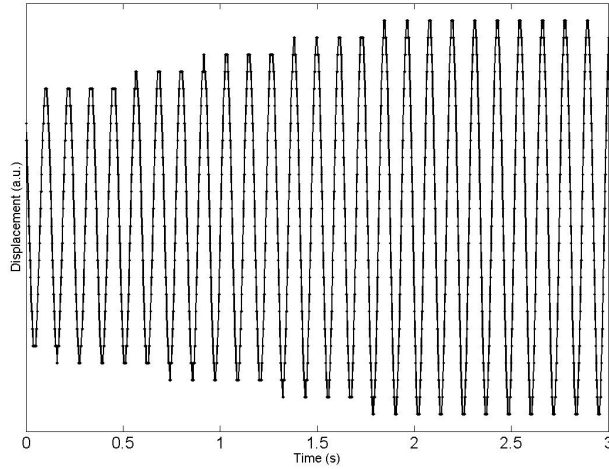


Figure 3.4: Displacement of the empty cylinder, measured using high speed imaging, for instantaneous acceleration change, i.e. instantaneous according to the software.

by a few seconds. This is a characteristic profile, i.e. all runs have a maximum deviation of about 5% of the desired signal.

3.2 High speed imaging

We experimented with two camera positions. One is just above the level of the fluid at rest at about $1m$ away from the center of the cylinder. The other is from a higher position under an approximately 45° angle and at a close distance. The second method can be used to study the profile close to the equilibrium position as the fluid at the walls can obstruct light paths in the other camera setup. Examples of such profiles are capillary and meniscus waves. The first method is used to focus on the vertical cross-section in the center of the cylinder. The camera is positioned somewhat higher to avoid refraction effects when viewing through the fluid. In this setup the camera is also tilted because the height of the image is easier to adapt, while we want more flexibility for the width. This is used for instance in parameter sweeps, when only a small portion of the resolution is required, allowing longer images to be recorded.

In figure 3.6 the contour for a crest and trough is plotted for a wave in (1,0) mode. All image analysis procedures are in fact matrix manipulations. These contours are found by the class of morphological structuring in Matlab. The profiles appear to be very accurate except for the edges of the crest and a small curve on the left of the trough. The droplets on the inside of the wall cause little problems in this method. The algorithm is able to extract the surface profile as a function of time by means of a for-loop. The computational expense is mainly due to the loading of the frames from the recordings.

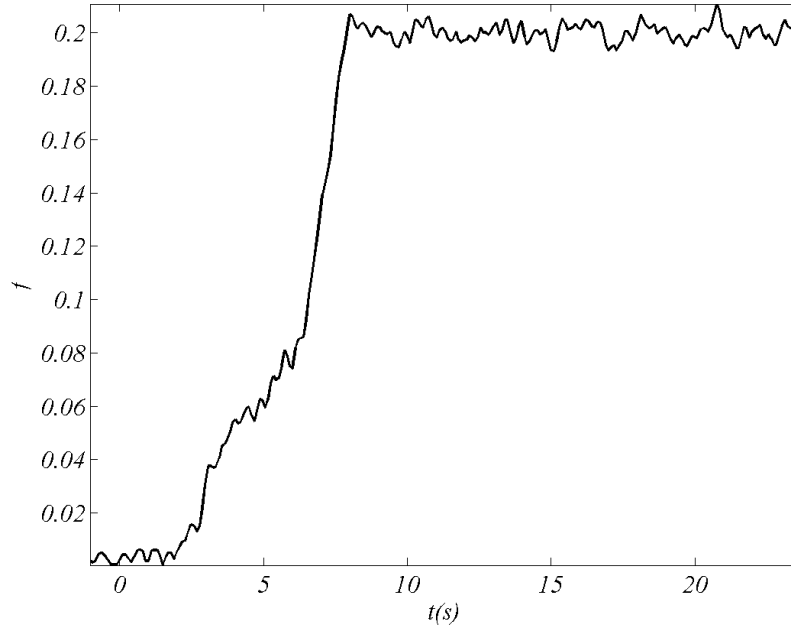


Figure 3.5: Forcing amplitude as measured by the shaker software. The excitation frequency was 8.40Hz and the time interval is rescaled to align with that of the camera recordings.

The top and bottom contours are found separately because they are influenced differently by refraction. In figure 3.7 the effect is visualized for a millimeter spaced grid. It appears a linear scaling of the bottom contour is sufficient. This calibration image is recorded after every repositioning of the camera. It is a grid printed on a transparent sheet and attached to a perspex bar. We placed it manually in the cylinder but placeholders on the top and bottom of the bar make sure it is in the center and vertically aligned. The azimuthal alignment is obtained by placing a rod over the camera and cylinder. If the rod is parallel with the camera the bar grid should be perpendicular to it.

We like to point out that high speed imaging is expensive in memory and downloading time. Other methods have been proposed in the investigation of Faraday waves. For instance, figure 3.8 shows the amplitude in the center of a square container with a 92% glycerin mixture [81]. Here a laser sheet technique is used, such that the amount of light measured at the other side of the container is a measure for the wave height. The method is very fast and efficient, but one-dimensional and therefore only applicable if one expects a single wave state.

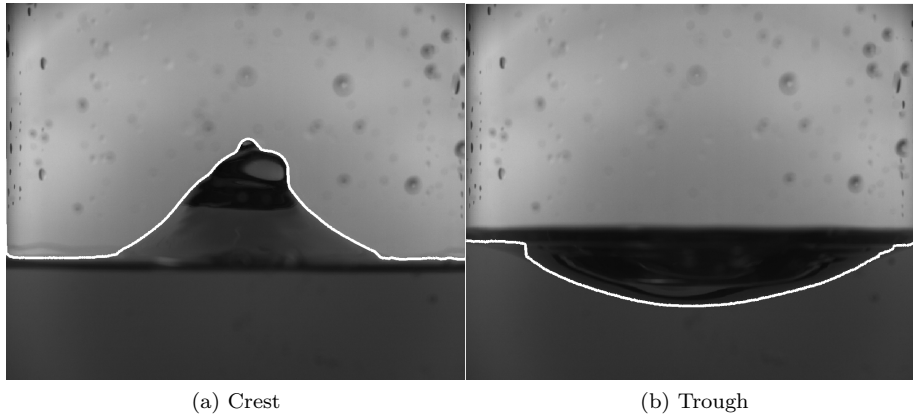


Figure 3.6: Images of a (1,0) mode at $8.6Hz$ and the contour found in Matlab.

3.3 Automation

In order to do a lot of measurements in a large parameter space, our experiment is partially automated. All equipment, with the exception except the light sources, is connected to the computer in a way such that both data can be downloaded and commands can be send. We use a Matlab algorithm to communicate the devices. The acquisition module is fully compatible, while the shaker software can only be run using keyboard and mouse commands. Photron has drivers available such that various scientific programs can initiate and download recordings. Matlab can be used to call a Java robot which commands mouse movements and keyboard strokes. As this functionality had to be employed to operate the shaker software, it was used to communicate with the camera as well. Besides, it was found that algorithms communicating with the Photron are difficult to design, have less functionality compared to the original software and are less stable.

The layout of the algorithm is as follows. The software of the shaker and camera are active next to Matlab. The necessary mouse positions are saved as a location on the screen. For the Photron and the acquisition module sub-algorithms are written that start, stop and save a measurement. The latter uses the National Instruments Toolbox available in modern versions of Matlab. For the shaker there is also the possibility to adjust the settings for every run. When it is done the software's data is saved as well. It lists for instance the demand and actually response of the system. As this only concerns data in the vertical direction the other accelerometer is still needed.

It is actually necessary to use a computer to trigger the experiments in order to relate the data of the various devices. The acquisition module measures when the camera is triggered but its timing relative to the shaker is unknown. The algorithm therefore saves the time (with millisecond accuracy) when a start command to the three devices is made. This is done just before and after because the computer needs some time to process the command.

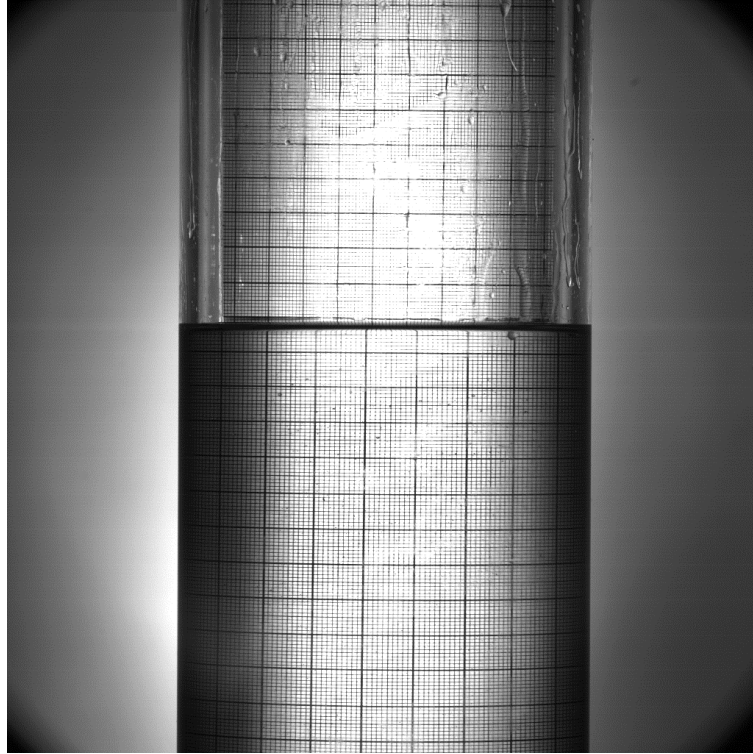


Figure 3.7: A millimeter grid in sunflower oil.

Other advantages are better time management. As lab time is limited our automated system makes it possible to give an accurate prediction of the duration of the experiments.

3.4 Surface tension measurements

Surface tension can be measured in various ways. A pendant drop experiment exploits the balance of surface tension and gravity of a drop hanging from a syringe. A video-based contact angle measurement device (OCA 20, Future Digital Scientific, Garden City, USA) is used to record the shape of the drop. It is assumed that the top cross-section of the drop is a disk of the size of the syringe. Its width is also used to calibrate lengths in the recorded images. The radius as function of the vertical coordinate (z) is fitted to a balance of Laplace pressure and gravity, i.e.

$$gz + \bar{\gamma}k = 0,$$

where the curvature is a function of z as well by substituting the profile of the drop. The best fit of this linear equation gives the value for $\bar{\gamma}$ as the gravitational constant is known.

We used this to perform surface tension measurements before and after experiments. A small sample volume from the cylinder was taken to this setup.

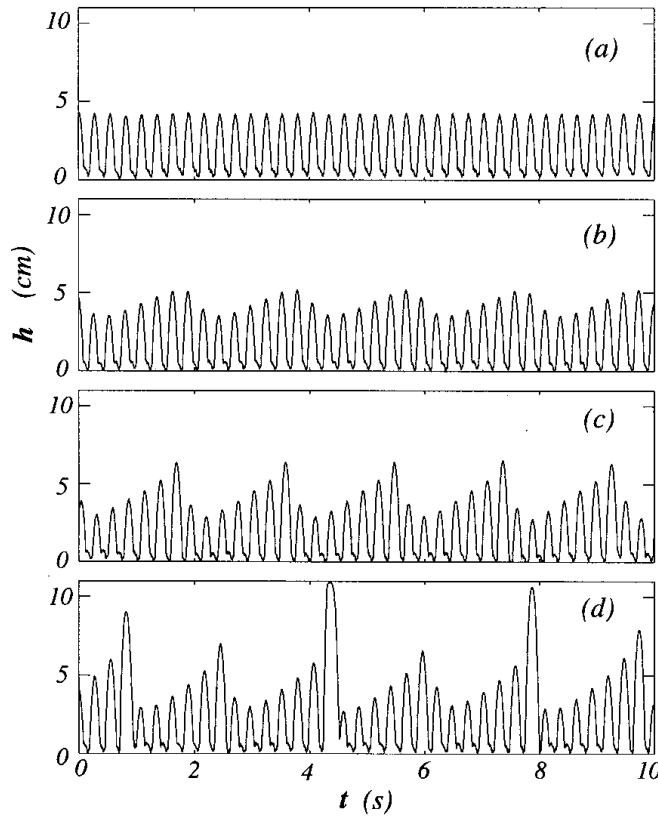


Figure 3.8: Time series of the wave height at a driving frequency of $7.4Hz$ with amplitudes $[0.48, 0.51, 0.52, 0.53]g$ for (a) through (d) respectively (taken from [81]). Mathieu behavior is clearly visible in (b), while (d) is a jetting state.

Also, a Matlab automated experiment was designed to measure the surface tension over very long time scales. This is to investigate the rate in which the surface is contaminated by for instance dust particles from the ambient air. The automation is in refilling the evaporated volume. This cannot be done by setting a constant flux into the drop, as the device cannot handle this small fluxes. Anyhow, the volume can be very different on a large time scales with this method. Too large drops will fall from the syringe and the accuracy drops for smaller drops.

If there is contamination we might have to include the corresponding tangential stresses following the discussion in section 2.2.3. However, our setup is sealed from the surrounding air and there is only a small volume of air inside the cylinders. On the other hand, the samples can not be taken from the surface or will not likely be on the surface of the drop since when in the device. This means that we will only measure the surface tension of the bulk fluid and not of the possibly contaminated surface.

Chapter 4

Analysis and Results

In this chapter we will discuss the experimental data. As an introduction we will first go into the results in a qualitative way. Next we will explain how the data is analyzed and we present the experimental results. The three regimes, solid-body, standing wave and jetting, are treated separately as well as their transition. The dissipation in the system is compared to the model.

All experiments were conducted in cylindrical containers, with the exception of surface tension measurements and experiments in the rectangular container. The latter were performed to investigate the thin film as the curvature of the cylindrical containers prevents the recording of film from a side view.

The acceleration of the shaker is fg for dimensionless f which we will use throughout this report. The dimensionless detuning and forcing are corresponding to section 2.1, i.e. $p = 4\kappa(g + \bar{\gamma}\kappa)^2\omega_0^{-2}$ and $q = 2f\kappa g\omega_0^{-2}$. All digital analysis were performed in Matlab.

4.1 Qualitative observations

For the cylindrical containers we recorded the motion in a horizontal side view and under an angle. The latter proved to produce valuable data for meniscus waves and the shape of troughs and cavities as this was poorly visible with the other method. In that case, the air-fluid interface close to the wall, like the meniscus, obstructed the light paths, see figure 4.2. In the case of standing waves there was an elevated profile near the wall and a deposited film complicating images of the profile in the center, see figure 4.1. We were not able to determine the thickness of the film because it is not visible from a side view in a cylindrical container. We can however assume the contact line is practically pinned in the interval of one period for constant driving amplitude as is visualized in figure 4.23. Standing waves are relatively simple to produce in cylindrical containers at small excitation amplitudes. Mathieu theory predicts the excitation frequency correctly and the profiles show good agreement with irrotational flow. In figure 4.3 several modes are visualized which should be compared with figure 2.9. As expected more irregularities are generated in water than on sunflower oil. For instance on crests (figure 4.4) and around large

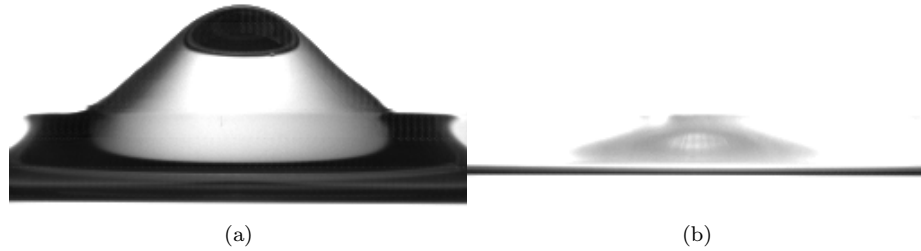


Figure 4.1: Two images of sunflower oil in a $(0,1)$ standing wave state. The profile in the middle is subject to refraction (a) and almost invisible for small elevations (b). The interval between images is $60ms$, which is half a period of the excitation.

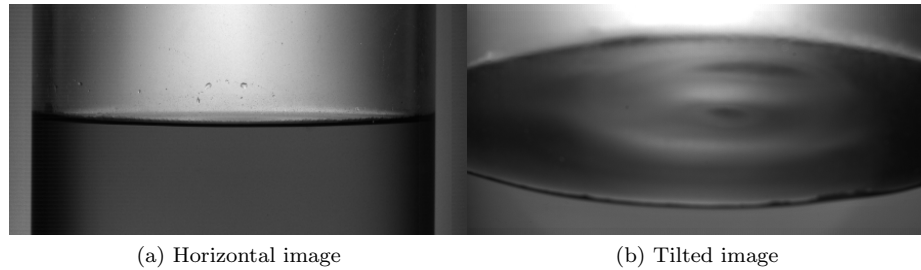


Figure 4.2: Two images of water in solid-body state showing that meniscus waves are actually only visible in the tilted view and only due to reflection of the surface. This image can be related to the capture of Douady in figure 2.12.

curvatures (figure 4.5) they are clearly visible. Jets also tend to break up earlier in water than in sunflower oil, which may lead to beautiful recordings of the impact as visualized in figure 4.6. Jets for other modes than $(0,1)$ were recorded as well. They are generally slower but surprisingly stable. For instance the $(1,2)$ mode produces two jets of different velocities closely after each other. The $(3,1)$ mode was found to produce wall jets, which simultaneously moved along the cylinder wall. Droplet ejection and bubble capture were encountered during experiments. The dynamics seems to be a combination of the standing wave with irregular waves, hence their creation is rather uncontrollable. A smaller wave can form a cavity on top of the crest of a larger wave. This can result in a small jet, intermediately contracted to a droplet by surface tension, or in bubble entrapment just below the surface by the wake of the jet pulled in the fluid when it does not detach. Once created they are very stable. Bubbles remain steady just under the surface and droplets may bounce of the surface instead of coalescing, see figure 4.7. Bubbles created by cavity collapse or jet impact can be very stable as well. The stability of droplets can be utilized. For smaller Faraday waves the experiment is more controllable such that droplets are able to survive for very long times. The droplet itself can be the trigger of Faraday waves in its surrounding and move over the surface as well. These droplets are known as walkers [19]. These effects did not seem to have significant influence

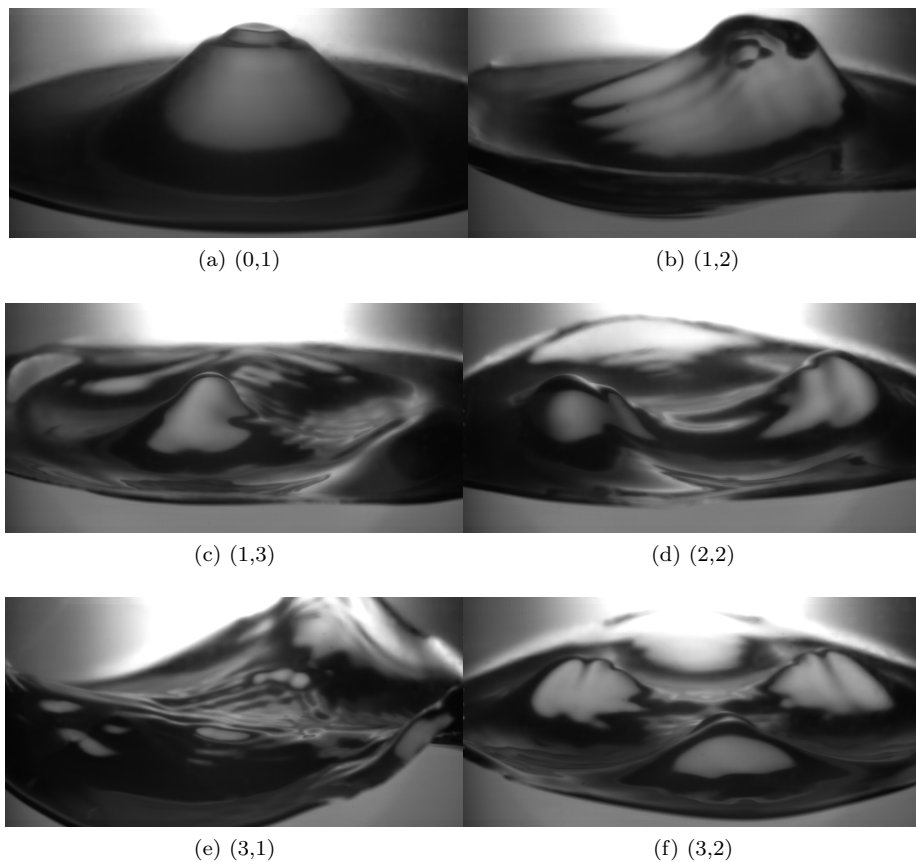


Figure 4.3: Several standing wave patterns in water recorded under an angle. The number within brackets denotes the state, while the detuning was almost unity for all cases.

on the standing waves.

4.2 Solid-body state

As described in chapter 2 the fluid will be in a solid-body state at the beginning of experiments. The characteristic fluid motion for this state are meniscus waves. It is natural to start here because this will always be the first state the system is in. Hence, we will examine how they arise from fluid profile at rest and how their amplitude stabilizes. Their parasitic presence in other states, e.g. fully developed standing waves, is commented on later.

4.2.1 Meniscus waves in water

In figure 4.8 a series of recordings are visualized for the forcing for $0 \leq f \leq 0.2$ as plotted in figure 4.10. This forcing is enough to trigger Faraday waves but they are not observable before $t = 12s$. It is very difficult to extract the exact

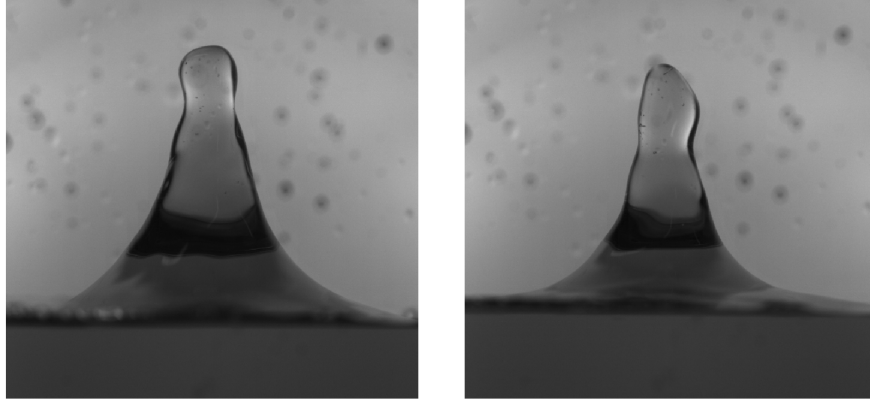


Figure 4.4: Surface irregularities in water one cycle before jetting. The time between frames is $26ms$, which corresponds to a phase difference of 0.44π .

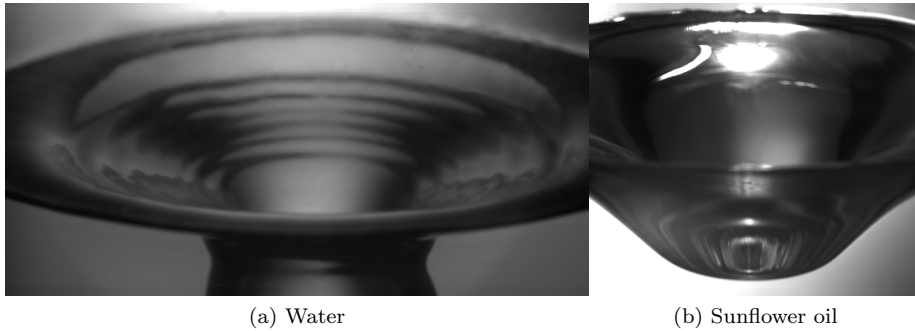


Figure 4.5: Two cavities and their surface profile recorded under an angle. Surface disturbances on the expected profiles are clearly visible in water due to its smaller viscosity.

profile of these waves because only the reflection is visible which only reveals potential information about the slope of the surface. Even the way the waves travel is hard to determine. At the startup the waves travel from the walls to the center as they are created by the meniscus.¹ The waves appear as traveling in the remainder of the frames but we find that the initial disturbance is 'taken over' by a standing wave. As mentioned in section 2.2.8 a real traveling wave should go to infinity at $r = 0$, but the recordings show the curvature is very small where the profile should at least tend to go to infinity if surface tension was a force countering this behavior. The traveling nature of the wave is because standing waves are actually a superposition of traveling waves. A combination of the standing waves may appear as a traveling wave, for instance

¹When the frames are shown subsequently as to form a movie this is much clearer.

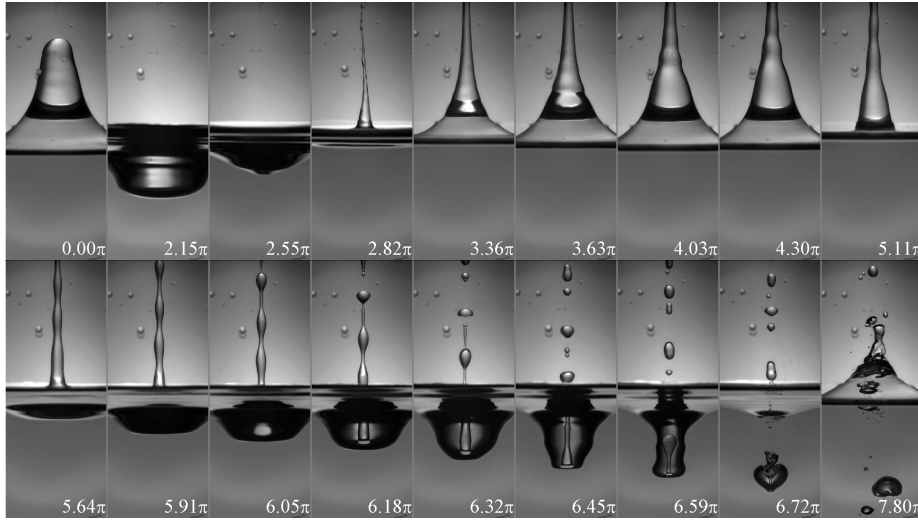


Figure 4.6: Jet and its impact in water for $p = 1.04$, $q = 0.104$. The number denotes the phase relative to the excitation in radians.

in our tilted camera setup.² The wave profile can be better understood when we take a small vertical strips along the center and paste them together for a number of consecutive frames. This is done in figure 4.9 for an interval that the excitation amplitude is constant. The waves are indeed isochronous, i.e. of the same frequency as the excitation.

The (0,3) standing wave state appears to approximate the profile correctly. The system is driven at $\omega_0 = 8.4Hz$ and linear dispersion yields $\Omega = 7.70$ and $\Omega = 9.46$ for the (0,3) and (0,4) states respectively. They correspond to $p = 3.36$ and $p = 5.07$ while q is small such that there is no Mathieu excitation for these modes according to the phase plot in figure 2.1. The strips can also be combined for a larger interval. In figure 4.10 they are visualized combined with the forcing obtained from the shaker software. The motion of the contact line and the surface profile show corresponding behavior.

4.2.2 Meniscus waves in sunflower oil

For sunflower oil approximately the same results are obtained, which is expected as fluid properties are less important in this low amplitude behavior. However the higher viscosity lead to higher damping and the reflective properties of the oil result in ill images. In figure 4.11 a few instances of the meniscus wave in sunflower oil are plotted for $f = 0.25$ and $8.303Hz$.

²One can easily check this for oneself; define more than one standing wave on an arbitrary spatial interval, each with a unique temporal periodic dependence. Now add them together and plot the result for several appropriate time steps.

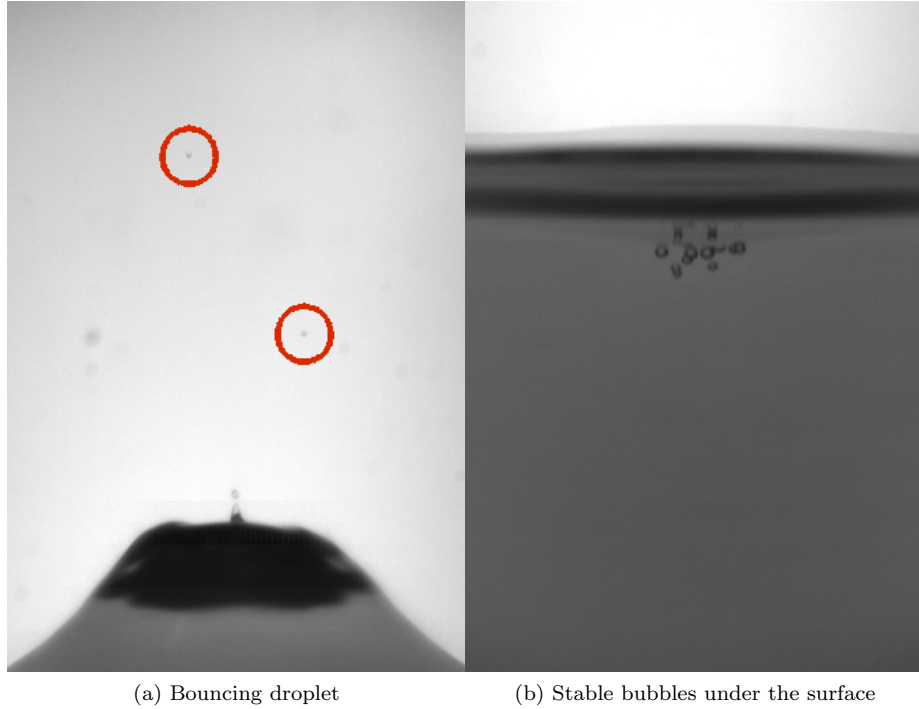


Figure 4.7: a) Zoomed image of a crest in the (0,1) mode. Two droplets (inside red circles) that bounced of the surface in previous cycles and a new droplet at the moment of ejection. The jet shape on the crest is clearly visible. When the droplet does not detach the jet is pulled inward and a bubble is formed under the surface. b) The (0,1) standing wave moving through its equilibrium showing multiple entrapped bubbles created by this process.

4.2.3 Transition to the Faraday waves

In figure 4.10 not only the solid body state is visible but also the evolution of the system to a standing wave state and even to a jet. The standing wave can be clearly observed from the motion at the edges, especially after $t = 14s$. It is period doubled and the amplitude is larger than the excitation of the cylinder, showing the contact line is in motion. We hypothesized that the contact line cannot be pinned when the amplitude is significant since the contact angle becomes too large. For this low amplitude waves we assume the contribution to the profile of the (0,1) mode is given by the combination of an Airy wave and a boundary layer to the lowest order, c.q. the profile in figure 2.10. In that case the derivative at the wall is $|\partial|_r \eta(L) = 1.62 \cdot 10^3 A$ with A the elevation at $r = 0$ (and the prefactor of units m^{-1}). The hysteresis from the equilibrium contact angle is $0.334rad$ such that $|\partial_r \eta(L)| \leq 0.34$, resulting in $|A| \leq 0.21mm$. This is a very small wave and not recordable from a side view as it is 5 times smaller than the meniscus height. The meniscus wave contributes to the elevation as well so the angle can be too large even for smaller waves. Its wavelength is longer but of the same order so we can expect the amplitude is also of the same order

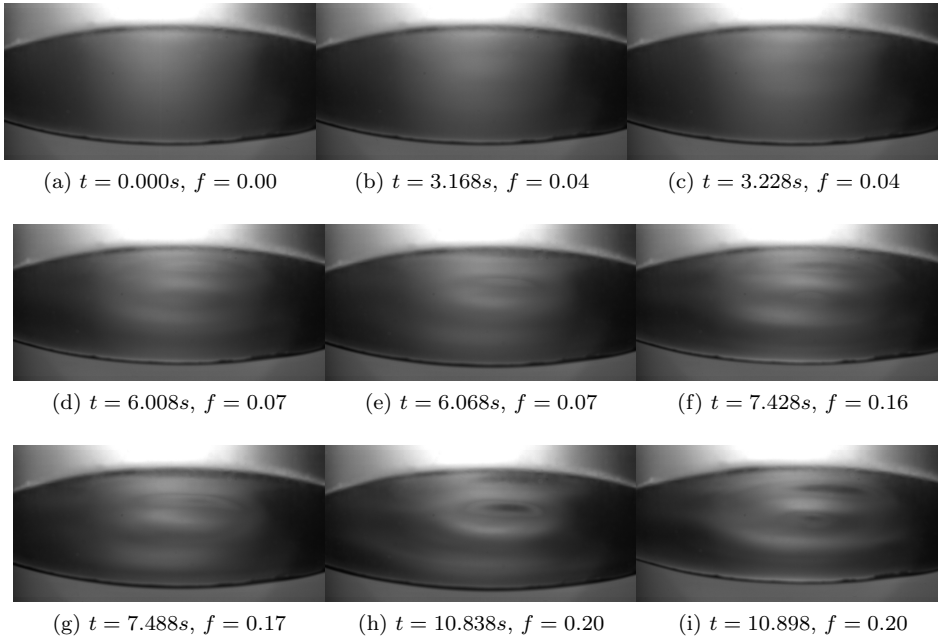


Figure 4.8: Meniscus waves in water recorded under an angle corresponding to the forcing in figure 3.5. The time of the images is such that there are pairs that are approximately half a period from each other, except for (a). The forcing is read from the shaker signal at the instant of the image. The images are recorded at 500fps , with a closure time of 3000^{-1}s for 512×1024 pixels.

when the contact line is pinned. In fact, it appears that the meniscus waves is already at the contact angle limits as the Faraday wave in figure 4.10 is not visible before the contact line is unpinned, i.e. the period doubled components are always larger than the meniscus wave. Apparently, the meniscus wave can not trigger the movement of the contact line, which supports the interpretation that the dynamic meniscus actually is a wavemaker. If the contact line would move the meniscus wave generation mechanism has subsided. This can also be seen from the fact that the isochronous component decays for $16\text{s} \leq t \leq 19\text{s}$, when there is no pinned contact line anymore.

The measurements confirm the existence of meniscus waves. They are gravity waves, as they obey the corresponding dispersion relation and they are externally driven as they are isochronous. The recordings support our hypothesis about the generation mechanism but are inconclusive. As long as we can not extract the exact surface profile this analysis remains rather qualitative in nature. A measuring method can be developed based on the reflection of the surface, to study meniscus waves more deeply.

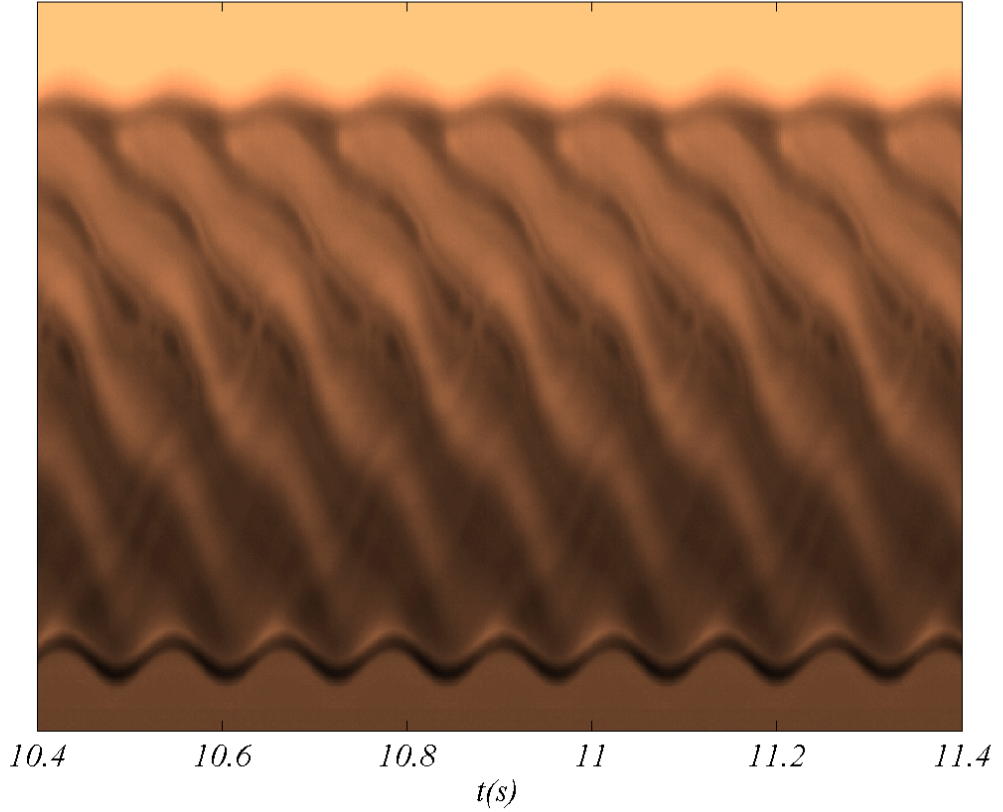


Figure 4.9: This image is constructed out of the recordings visualized in figure 4.8. From those images of 512×1024 pixels a vertical strip of 512×4 pixels is taken from the middle. Here 500 consecutive strips are combined together, which consequently correspond to a temporal interval of 1s as the frame rate was 500fps. The horizontal axis shows the camera time, i.e. $t = 0$ corresponds to the start of the recording. From this image one observes the isochronous behavior of meniscus waves. The waves appear to be generated at the top boundary and to be traveling to the other side (bottom boundary). However, the system is symmetric so the waves are generated along the entire circumference equally. The (0,3) mode has three wavelengths in this spatial interval, which is in good agreement, although the term 'wavelength' is a little strange for cylindrical waves.

4.3 Standing wave state

The state of stable Faraday waves is denoted as the standing wave state. We will first examine the profile of the waves and compare their temporal response with Mathieu functions. Then we will analyze the boundaries of the regimes and measure the dissipation. Finally we will take a closer look at the transition to other states. In this section we will emphasize on the (0,1) state for

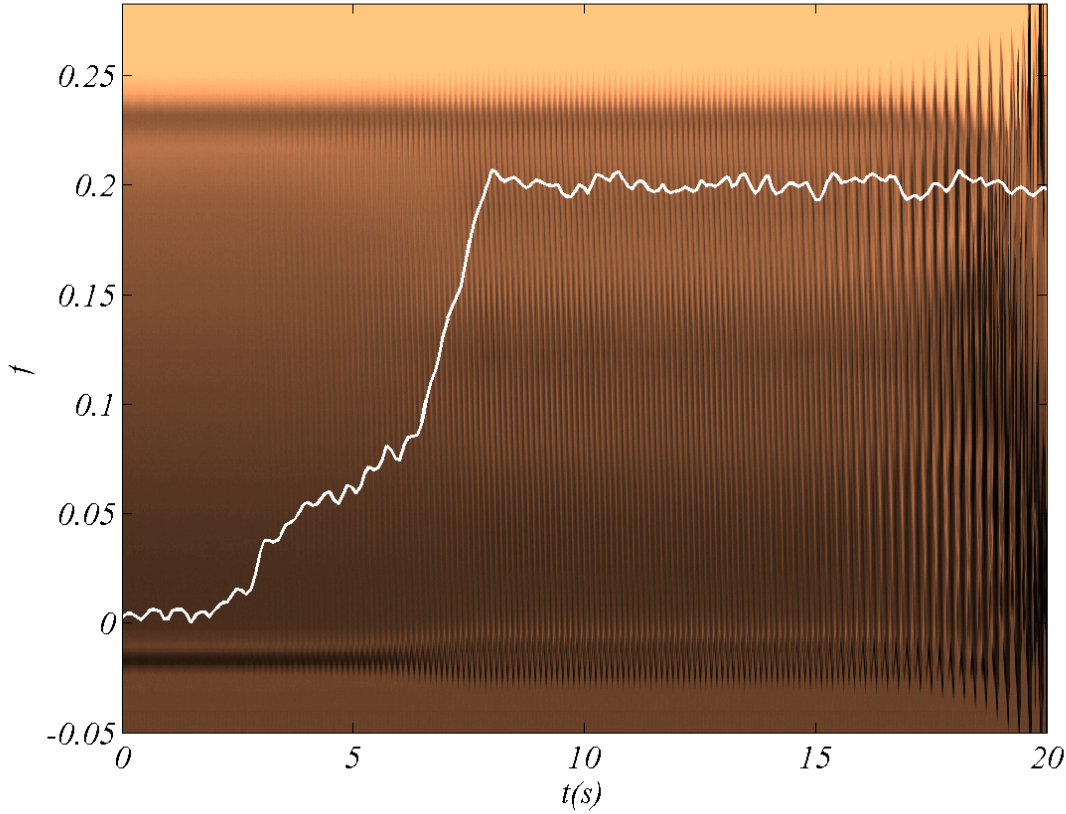


Figure 4.10: This image is constructed in the same way as figure 4.9, i.e. a combination of vertical strip of 512×4 pixels. In this case there are 10^5 strips over an interval of 20s. The forcing for this run is plotted as well (white line). The horizontal axis shows the camera time and the vertical axis shows the forcing amplitude f . From this image it is hard to observe the individual waves and we would like to focus on the amplitude, which is easiest observable near the edges of the cylinder (at the top and bottom of this image). The meniscus waves follow the forcing almost instantly. After $t = 14$ s Faraday waves are visible which can be observed from the period doubled motion. Simultaneously the meniscus waves decay, which can be seen from the vanishing isochronous component. At $t = 19$ s the isochronous component has disappeared completely. At approximately $t = 20$ s a jet is formed.

water and sunflower oil. As the cylinders vary slightly their wavenumbers are $\kappa = 71.0 \text{ rad/s}$ and $\kappa = 70.6 \text{ rad/m}$ respectively. The depth was 162 mm and considered infinity deep for the linear dispersion relation.

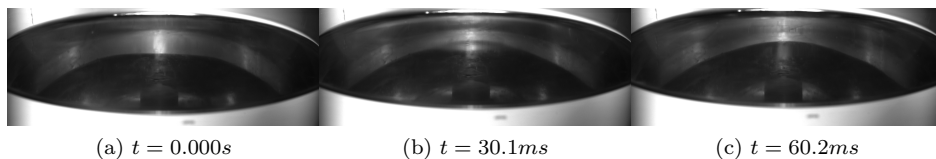


Figure 4.11: Meniscus waves in sunflower oil recorded under an angle at 8.303Hz . The images show three images of a cycle at $[0, 0.5, 1]\pi$. The images are recorded at 1000fps , with a closure time of 4000^{-1}s for 384×1024 pixels. In contrast to figure 4.8 it is much harder to observe waves in oil. This is because of the reflective properties of the fluid and due to the larger viscous damping resulting in smaller waves. If observed carefully, the intensity of the light just above the middle of the images changes in every frame. A movie of consecutive images makes it much easier to observe meniscus waves.

4.3.1 Mathieu function

For smaller waves we expect the profile of the waves to behave as modes predicted by irrotational flow. The Airy approach predicts their evolution to be like a Mathieu function. However, waves in water are distorted by parasitic waves as seen in figures 4.3 and 4.4 and for sunflower oil low amplitudes are hard to visualize. The profile of the viscous fluid is visible for higher amplitudes but in this case nonlinearities are significant, see figure 4.12.

On the other hand the modes obtained from irrotational flow, match reasonable to the shape of the standing waves. Their excitation frequencies is also correctly predicted by Mathieu theory, like in figure 4.3. We were always able to excite specific modes considered here around $p = 1$ for small excitations ($f < 0.2$). This suggests that the irrotational mode is excited by the Mathieu forcing and other (nonlinear) effects are in turn created by this motion. Therefore we can still expect period doubling as the dominant term. To confirm this the camera resolution was set to a very small width such that a vertical strip of the center is recorded, while focused at the center. We recorded the height profile for the (0,1) state by exciting the system for $0.2 \leq f \leq 0.4$. When the system transitions out of the solid-body state the forcing amplitude was lowered to a certain value. The system was held at this value until the motion was stabilized, i.e. when the amplitude was constant according to the experimentator, which was generally in the order of 10s .

One of the results is plotted in figure 4.13, for the same detuning as in figure 4.12. The period doubling is obtained but the growth rate is much too small, implying dissipation is significant. Also, the plots for $q = 0.088, 0.13$ stabilize at a certain amplitude, suggesting that the dissipation is amplitude depended as well. Even for large amplitudes the standing waves are stable. Nonlinear effects, like thin crests and shallow troughs are always observed. In fact, pure linear waves were never observed (except for meniscus waves) because the amplitude required for standing waves was always significant.

In water the results are similar. In figure 4.14 the surface elevations for wa-

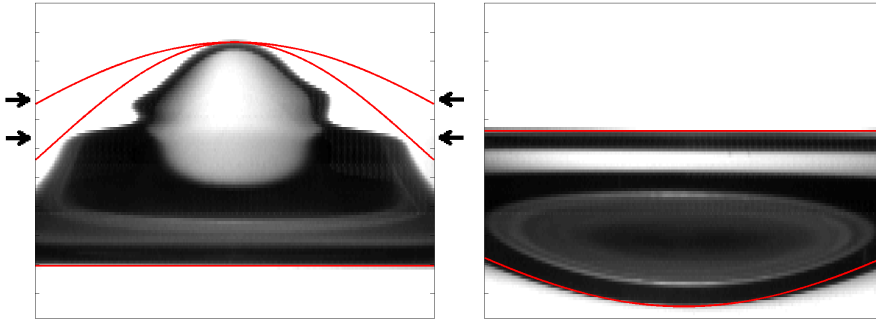


Figure 4.12: Two images (104×256) of sunflower oil in a standing wave state for $p = 1.04$. The width is approximately $L/2$ and the height of each image is 21mm. In the left image a crest is visualized. The arrows next to the image indicate a strip that is distorted due to oil on the inside of the cylinder wall. The surface profile in this area is therefore not representative. The height of this strip is approximately 3mm in this case. Above the strip the image is not affected, while under the strip the surface profile appears to be stretched due to refraction effects of the oil-perspex interface. We have to use the calibration images to relate these parts to each other. The three red lines are fits to the (0,1) mode (R from eq.(2.55)) using this calibration image. The bottom line corresponds to the value of the profile at $r = L$, which is a straight line because of the cylindrical symmetry. The other two lines correspond to the radial dependence of R which are scaled such that at $r = 0$ they relate to the height of the crest and at $r = L$ to the bottom line. The top line is corrected for refraction effects using the calibration image, while the middle line is not corrected. The dimensionless excitation is found by multiplying the excitation at $r = 0$ with the wavenumber, yielding 0.78.

In the right image a trough is visible. Here no distortion is present because the whole image is seen through the oil-perspex interface. Again the profile of the (0,1) mode is plotted but the uncorrected line is left out. The dimensionless excitation is -0.61 . Both values are too large for the waves to be considered linear. In this case the top line corresponds to the contact line. This position corresponds to the location of the distorted strip in the left image.

ter are plotted. They require smaller driving amplitudes but are also less stable as expected for a less viscous fluid. In the third plot one can observe that the jets are more violent, since irregular motions are less damped as well.

The (0,1) standing wave state is relatively stable and is susceptible for frequencies predicted by (linear) Mathieu functions. This is even true when the system is in a jetting state. Nonlinear effects are clearly present for amplitudes that the system is in a standing wave state.

4.3.2 Parameter sweeps

To further investigate the stability of the standing wave state we performed sweeps through the parameter space. We will slowly vary the frequency and amplitude to find the borders of this regime. From Mathieu theory we know

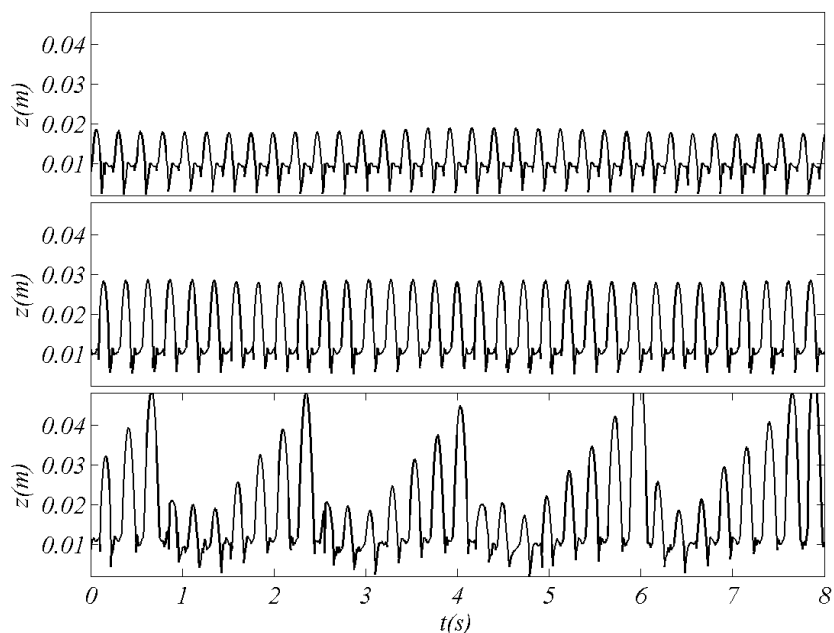


Figure 4.13: Surface excitation in sunflower oil for $p = 1.04$ and $q = 0.088$, 0.13 and 0.15 . The highest elevation is extracted such that plot is actually an overlap of the crest and profile near the wall which causes the wiggles. Other irregularities are caused by droplets falling down or asymmetric motion. In the third plot, the highest excitations represent jets, but due to possible asymmetric motion their captured elevation may be smaller.

that the response depends heavily on both parameters. At low amplitudes we expect the transition of the solid-body and standing wave state. Here nonlinear effects are the smallest which makes it useful to study dissipation. At higher amplitudes jets will occur, which phenomenon is an interesting part of our study, hence the involved transition as well. Moreover, other modes than the $(0,1)$ mode will be excited in experiment. The $(2,1)$ and $(3,1)$ modes are the first to be excited as their eigenfrequencies are close to that of the $(0,1)$ mode. Their wavenumbers are $56.5, 77.8$ (water) and $56.2, 77.4 \text{ rad/m}$ (sunflower).

This parameter space is large. We found jets in water for $q = 0.1$ but more forcing is probably required at larger detuning. The $(2,1)$ and $(3,1)$ modes have a detuning unity for respectively $p = 1.27$ and $p = 0.90$ for the $(0,1)$ mode. Their presence will probably be observed for values closer to unity. The edges of the parameter space are where these states become dominant. The largest disadvantage of such a large space is the limited measurement time. Since we are provisionally interested in the borders of this mode and the standing waves are clearly distinguishable as are jetting and solid-body states, we performed the observations ourselves. The frequency was held constant and the amplitude was changed with steps of 0.2 dB . We waited 10 to 20s on average in a pa-

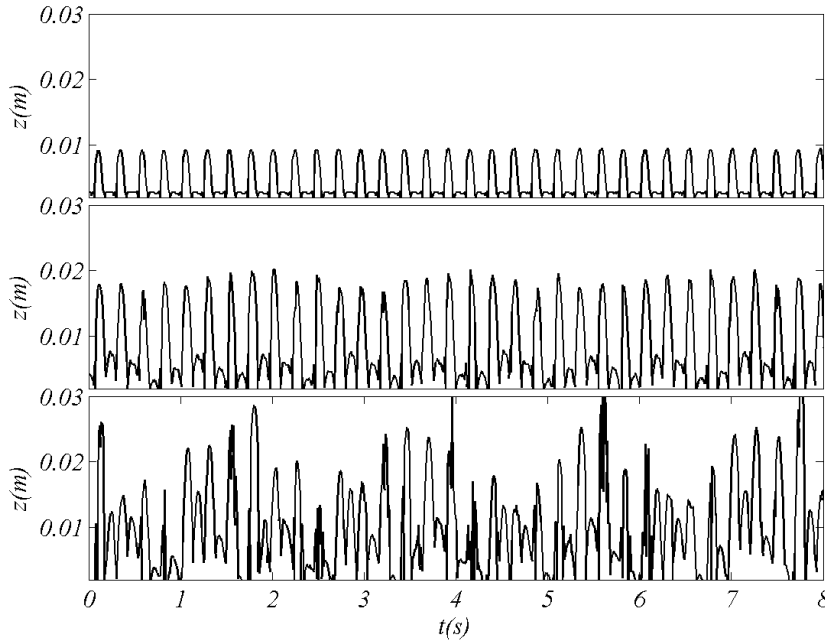


Figure 4.14: Surface excitation in water for $p = 1.04$ and $q = 0.036, 0.083$ and 0.099 , which is similar to the results in figure 4.13. In the third plot, the highest excitations represent jets as well.

parameter point. We first increased it from the solid-body state then decreased it from the jetting state and noted the values for which transitions occurred. The result is plotted in figure 4.15. The modes are placed in their corresponding regimes and the stars denote transition locations. For instance, for almost the entire frequency range the fluid is in the solid-body state, $(0,0)$ below $q = 0.04$. Jetting occurs in the top area but is still denoted by a $(0,1)$ state. At the edges of the chart, the system changes to a $(2,1)$ mode for small frequencies and to a $(3,1)$ mode for higher frequencies. The $(0,1)$ mode was only observable for higher amplitudes and higher frequencies. We did not define a transition here because the exact location was unclear.

The region where both the $(0,1)$ and the $(0,0)$ mode occur, is particularly interesting. The existence of a standing wave mode completely depends on the previous state of the system, which means the upper transition is one from solid-body to a jetting state. Since instant jets are impossible and a few waves are observed in the transition recordings of this transition is necessary.

An experiment using high speed imaging was also designed. We varied the frequency and the amplitude simultaneously and proportionally in order to scan through the space of $2\pi \cdot 8.0 \leq \omega_0 \leq 2\pi \cdot 8.9 \text{ Hz}$ (or $1.14 \geq p \geq 0.92$) with forcing amplitudes $0.02 \leq f \leq 0.4$. Four sets of 81 diagonals of varying length are performed to cover the entire the space and hysteresis effects. At a rate of

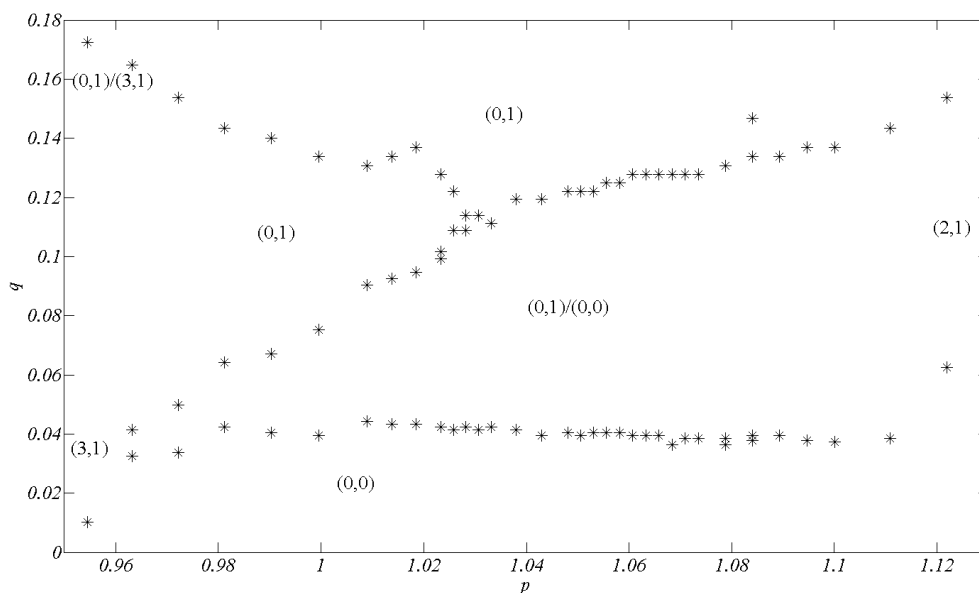


Figure 4.15: Phase plot as a function of frequency and amplitude. All stars denote individual measured transitions. A few are obtained for the same frequency, implying this measuring method is not adequate. The modes denote the state of the fluid in the corresponding area. According to section 2.1 the growth rate should strongly depend on p with a maximum at $p = 1$. However, the transition from standing wave state to solid-body state is nearly independent of p . This could also have been a discrepancy of the measuring method.

$11.5mHz/s$ or $4.87 \cdot 10^{-3}gs^{-1}$ (m for milli) the experiment takes about 15 hours including downloading of recordings. The images are 1024×16 pixels (minimum width) and the frame rate is $1000fps$. Two of the sets in water are visualized in figure 4.16. The space was divided into smaller areas and the average crest height is calculated for the time the parameters are in this particular region. The left image shows some similarity with figure 4.15 but for the bigger part the results are completely different. Firstly, there is some randomness in the plots. The overall trend is visible but adjacent diagonals are not smooth transitions to one another. Some runs go into a standing wave state while others skip this state altogether. On the top right of the left image some runs lost too much amplitude that the remainder of those runs in the right image are again in the solid-body state. In general, the dynamics are clearly determined by their previous states. We conclude that the sweep rate is much too fast for a phase plot. This was also the case in other runs. Also the direction of the sweep was important as the results in this plot differed from those in a backward diagonal sweep (not plotted) or in a vertical sweep (for fixed frequency, e.g. figure 4.15). This experiment suggest we have to lower the sweep rate drastically. We could lower the resolution by a factor of two and choose a smaller sweep rate. For acceptable spatial and temporal resolution this might result in a data reduction by 16. However, this only affects download times which are about two third of the

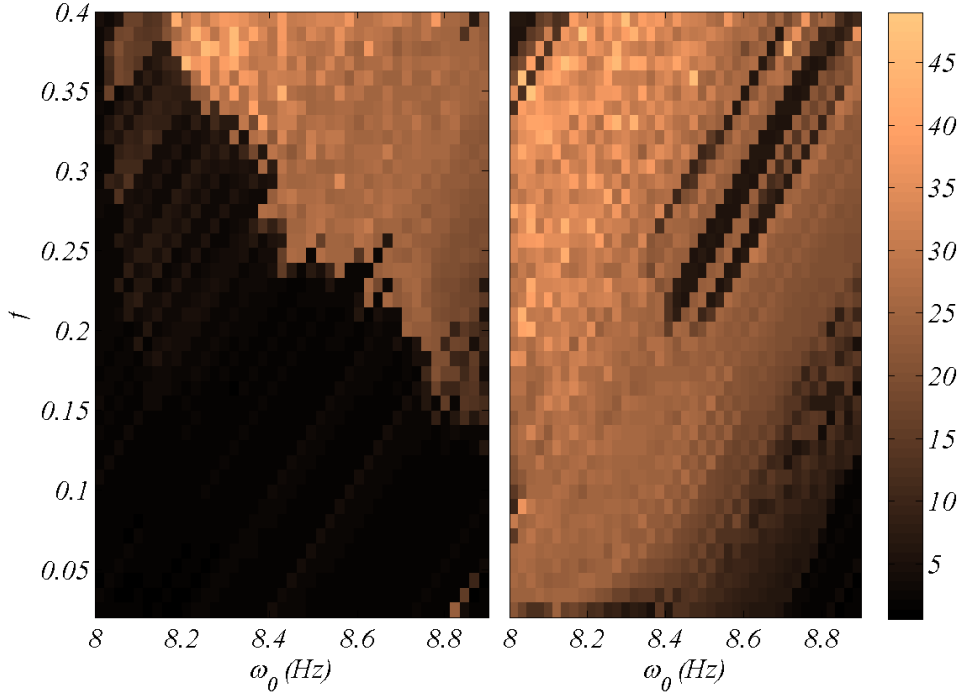


Figure 4.16: Average wave height for a forward parameter sweep (bottom left to top right and back). The scale is millimeters and the space was divided into a 41×41 grid, which corresponds to about eight cycles of the standing wave per cell. The run starts at the left or bottom border of the left image and sweeps until it reaches the top or right edge. The experiment continues by sweeping back to the start position which results are plotted in the right image. The axes are not rescaled to p and q because the machine only allows the rates to be proportional, hence the diagonals. The corresponding p, q space would be like a trapezoid.

experimental time in this setup. If the download rates are decreased linearly the recording time is increased by eight thirds. As the sweep rate can be decreased by the same factor this is very likely to be slow enough for our requirements. Another factor is that the direction of the sweep is an important factor as well. One actually has to include the sweep-rate and the ratio of the amplitude-rate to frequency-rate as parameters for to find a correct phase representation.

As we are forced by limited experimental time we choose only two parameters to vary. As the standing waves grow the fastest around $p = 1$ we keep the frequency fixed and only vary the sweep rate. The direction parameter now only has two values, namely up or down. We still have all three states. The previous experiments are still valuable; we know when the (1,2) and (1,3) state join in approximately and that sweeps suffer from some irreproducibility, so we have to perform each sweep a multiple of times.

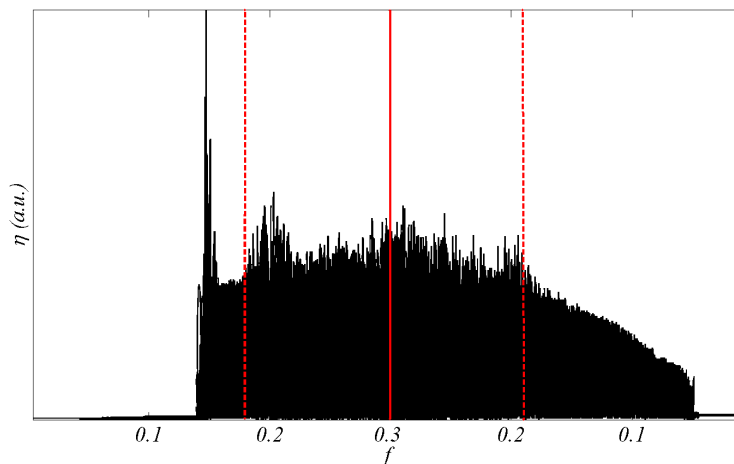


Figure 4.17: The wave height as a function of the excitation amplitude at a sweep rate of $0.5 \cdot 10^{-3} \text{gs}^{-1}$. The forcing was increased to $f = 0.30$ (red solid line) and then decreased at the same rate. The transition from a solid-body state to a standing wave is accompanied by 4 jets. The other transitions are smoother. The jetting state starts at $f = 0.18$ (left red dashed line) for increasing forcing and ended at $f = 0.21$ (right red dashed line) for decreasing forcing. On the right of the graph the relation of the wave amplitude to the forcing amplitude seems linear, before the motions transitions to the solid-body state. The transitions were confirmed by manually watching the recordings.

4.3.3 Transitions and Hysteresis

In the following experiment the camera resolution was again of small width, 512×48 pixels while the frame rate was smaller at 125fps . We chose $p = 1.04$ which corresponds to 8.400 and 8.303Hz in water and sunflower oil respectively. At different sweep rates the amplitude is gradually increased and again decreased. Also, the intervals slightly varied to determine if this was a factor, but we did not find significant influence, as long as all regimes are passed through. As we know the excitation as a function of the camera time when can relate it to the wave height. As mentioned before there is some fluctuation on the forcing signal. A result is plotted in figure 4.17 for the slowest sweep rate of $0.5 \cdot 10^{-3} \text{gs}^{-1}$ for the interval $0.01 \leq f \leq 0.30$ in water. Most notably are a few jets at the transition from a solid-body to a standing wave state. The results are combined in figures 4.18 and 4.18 where the transitions locations are denoted. The direction of the sweeps is from bottom to top and this is how one should read the plots. For every rate there are three runs for water and two for sunflower oil.

The results for oil are much more regular than for water, which can be expected

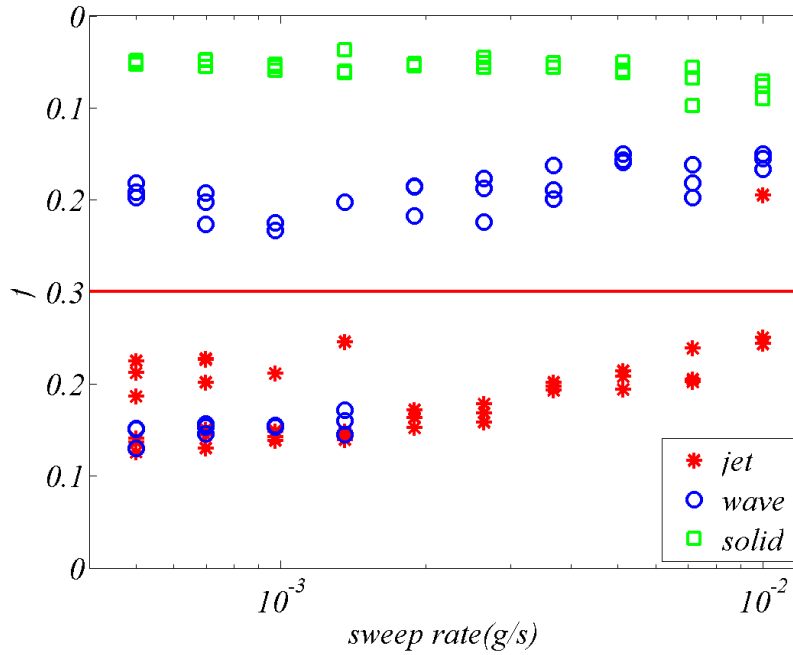


Figure 4.18: Transition locations in water plotted as function of the sweep rate and the excitation. The graph should be read as follows. As the frequency is constant for every run, we start at a small excitation at a certain sweep rate, say $1.3 \cdot 10^{-3} \text{gs}^{-1}$. As the excitation increases we move up in a straight line. At $f = 0.15$ the wave transitions into a jetting state. At $f = 0.3$ (solid red line) the sweep direction is reversed, i.e. the excitation is now decreasing, but in the plot we keep moving upward. When the excitation returns to approximately $f = 0.2$ the fluid transitions in the standing wave state and in the solid body state at $f = 0.05$. At a small excitation, $f = 0.01$ in this case, the run ends. The experiment was performed three times for every sweep rate.

as irregularities survive much longer in a low viscous fluid. For both fluids there is overlap of the regimes for faster rates. In some instances the jetting state is only reached when the excitation amplitude is already decreasing. For water at small rates there also seems to be overlap but these are merely a few jets formed in the transition from a solid-body to a standing wave state, like in figure 4.17. Apparently, jets are always created in water for the transition from solid-body state. For sunflower oil this is only the case at faster rates where there is clear separation of the transition mechanism around $3 \cdot 10^{-3} \text{gs}^{-1}$. At lower rates the system transitions smoothly into a standing wave from the solid-body state. Water has a similar division for smaller rates than $1.5 \cdot 10^{-3} \text{gs}^{-1}$. For both fluids this transition is at lower excitation for lower sweep rates, although it seems that this transition in oil has not yet reached its asymptote. Even more slower sweep rates are not possible at this system's settings.

The transitions from jetting to standing wave to solid-body (the upper half of

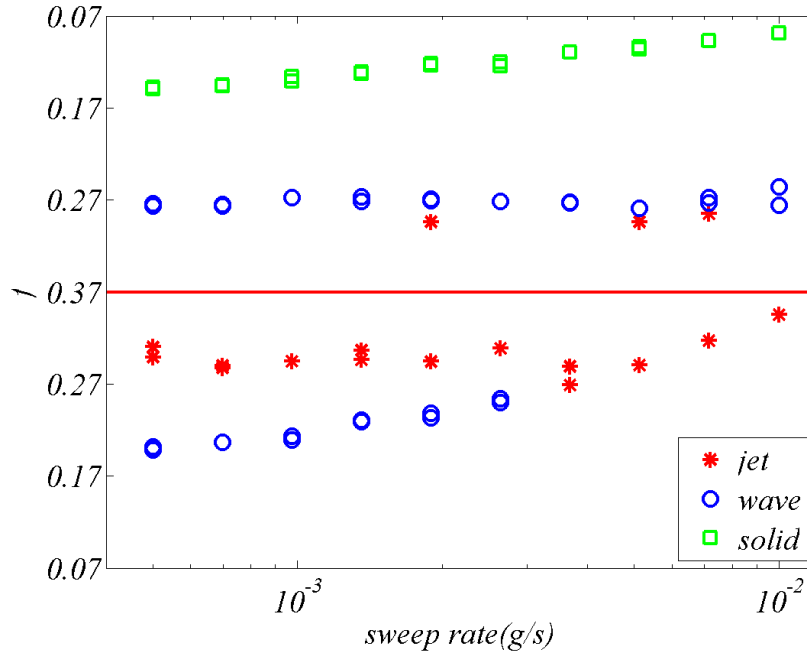


Figure 4.19: Transition locations in sunflower oil plotted as function of the sweep rate and the excitation. At $f = 0.37$ (solid red line) the sweep direction is reversed. The experiment was performed twice for every sweep rate.

the graphs, when the forcing decreases) are well defined and show little dependence on the sweep rate, except the latter case in oil. In that case the transition is at higher excitation for lower sweep rates as one would expect since the system has more time to react to the decreasing excitation. The system transition to the solid-body state eventually, but this evolution is slow compared to faster sweep rates. For water the trend is slightly in the opposite direction for small rates. For the jetting to standing wave transition there is apparently not much time needed to adapt. In the experiment with $4.87 \cdot 10^{-3} \text{gs}^{-1}$ and varying frequencies (figure 4.16) this was not the case. Evidently, the system behaves very differently when varying the parameters discarded in this experiment.

We observe that the system has enough time to adapt to the forcing at small sweep rates. Hence, we confirm the presence of hysteresis in our setup. Let us denote the size of the hysteresis by Δf , which is calculated by subtracting the excitation of the transitions for increasing and decreasing forcing. In figure 4.20 the hysteresis for both transitions is plotted as function of the sweep rate. For transitions of the solid body and standing wave states the minimum difference in excitation amplitude are approximately 0.09 for water and 0.05 for oil. The hysteresis in this transition depends on the sweep rate. For oil the trend is steeper which means that waves in oil react slower to a change in excitation. If we look at figure 4.19 we observe that especially the transition for increasing forcing is dependent on the sweep rate. It is unknown why this is different in

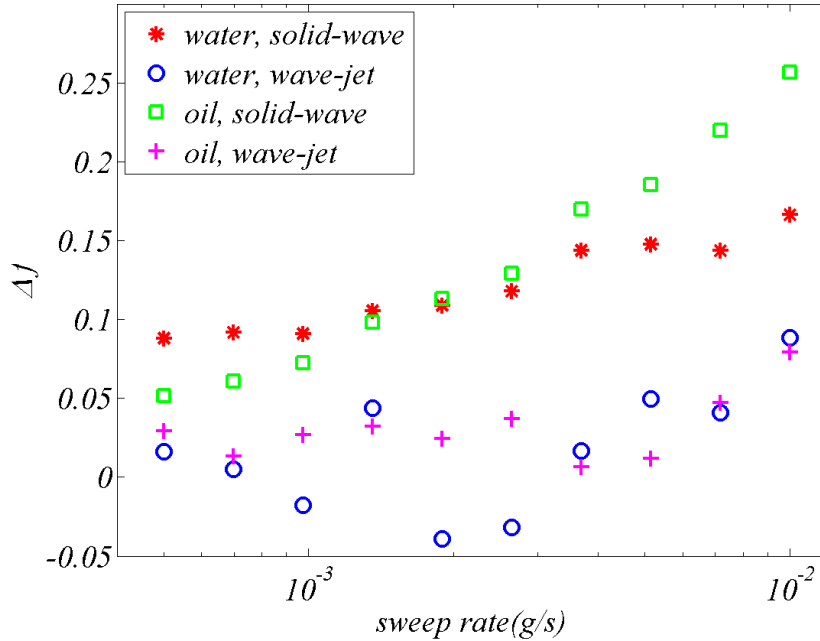


Figure 4.20: The difference in forcing (Δf) for both transitions in water and sunflower oil plotted as function of the sweep rate. The points are obtained from the average of the transitions locations in figures 4.18-4.19 and then taking the difference. A positive value means the transition occurred for higher values of f when increasing the amplitude. For instance the solid-body to standing wave transition for sunflower for $0.5 \cdot 10^{-3} \text{gs}^{-1}$ is at $f = 0.20$ when the forcing increases and at $f = 0.15$ when decreasing, yielding $\Delta f = 0.05$.

water. We would expect a constant value for the hysteresis at very small sweep rates as the change of the excitation will be very slow compared to the dynamics of the fluid. Apparently, the sweep rate is not small enough, although the trend is flattening at the left of the graph. At the smallest sweep rate considered here, the hysteresis is approximately twice as large for water. In section 2.2.9 we based that the energy required for the initial wetting on the movement of the contact line. We found that it should be proportional to the surface tension. The value for water is appropriately twice the value for oil.

In this transition we observed a few number of jets, in water for all sweep rates and for larger rates in oil. We explain this as follows. The contact line force can keep the system in a solid-body state for a long time and when it breaks loose the friction decreases with increasing amplitude, temporally leading to practically unbounded growth, resulting in jets before a standing wave stabilizes. Both results supports the hypothesis that the hysteresis in this transition is mainly due to the initial wetting motion. More investigation in the transition, like the influence of meniscus waves is required to be conclusive. One should also vary the values for surface tension and contact angle hysteresis in experiment.

The transitions of the standing wave and jetting states show an irregular trend for the hysteresis. At the smallest sweep rate, the values are 0.01 and 0.02 for water and oil respectively, but vary in both directions. In section 2.3 we argued that the hysteresis should be positive ($\Delta f > 0$) but we are inconclusive about the exact mechanism.

A final note is on the smoothness of the jets. The ones created from a solid-body state are better reproducible and show less asymmetric motion as for standing wave transitions to jets. This can be expected as there are more irregularities in standing wave. Jets created in a jetting state are completely exposed to this effect.

4.4 Dissipation

There are four sources of dissipation in our setup. They originate from the bulk, the wall and surface boundary layers and from wetting effects. In this section we will estimate their contribution and relate it to experiments. We assumed that the surface layer is negligible for uncontaminated surfaces and we will investigate the contamination first. The contribution from the bulk and the wall layer are evident and we calculate their influence. We already mentioned that the standing waves are non-linear, which one should keep in mind for our (linear) approximations. We will continue with wetting effects. For instance, we will examine whether the contact line is pinned for the interval of one period. Lastly, this analysis are compared with the transitions for the (0,1) mode.

4.4.1 Surface tension measurements

The surface tension measurements of samples from the fluid in the cylinder showed no difference before and after experiments. However, the samples cannot represent the surface of the fluid as mentioned in section 3. The long term experiment confirmed the influence of ambient. In figure 4.21 the surface tension of a pendant drop as a function of time is plotted. The surface tension clearly drops although there is apparently no lower limit, which means the surface contamination is not saturated over the length of the experiment. The larger deviations results from refilling the drop since the measurements assume a constant volume. The surface area ($20 \pm 1 \cdot 10^{-6} m^2$) is large compared to volume ($8.7 \pm 0.4 \cdot 10^{-9} m^3$) in this experiment.

The volume of the liquids in the cylinders are practically constant. Hence, there is insignificant evaporation and consequently no replenishment of containment particles in the air inside the cylinder. Since the rate of the decrease of surface tension is so small we assume the contaminating effect of the air inside the cylinder is negligible. Moreover, the fluid in the cylinder is contained for a large number of experiments such that any initial contamination has a constant influence. Also, the experiments of the next section 4.4.2 were repeated after a day with no notable difference in the results. This also suggest that the surface

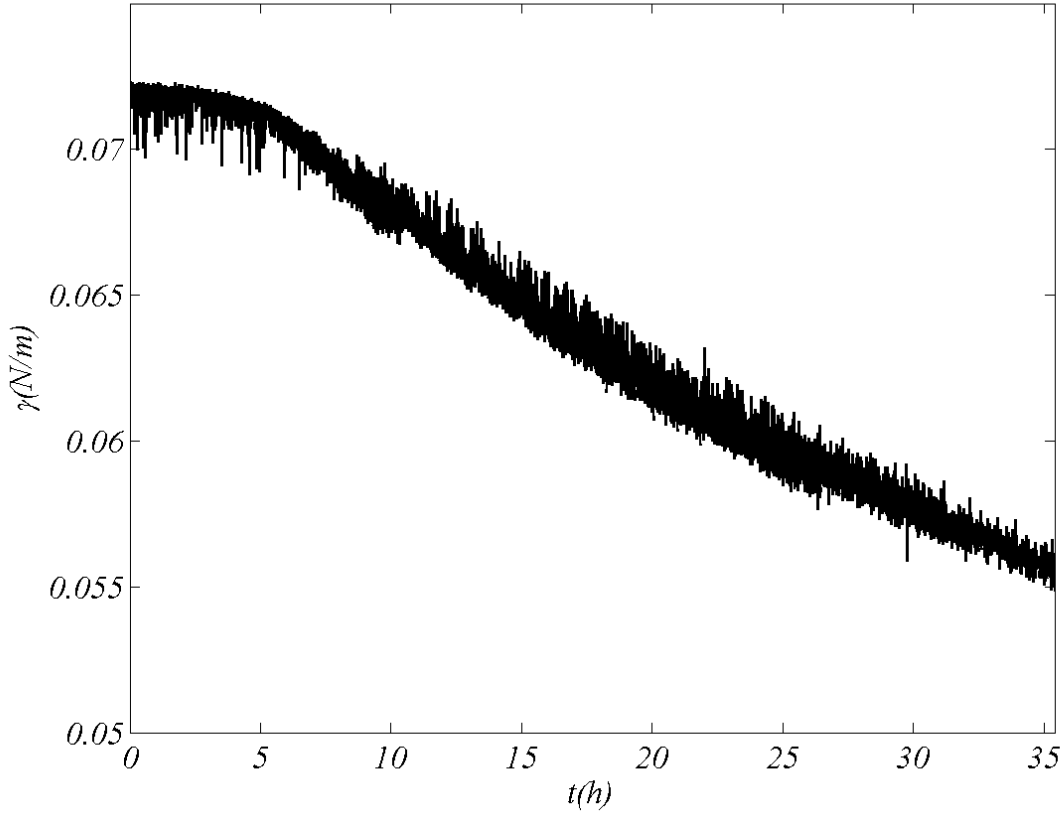


Figure 4.21: Surface tension of a water (with dye) droplet in ambient air.

is not contaminated (further).

Although no such experiment was conducted for sunflower oil, the same reasoning applies. Since this experiment is inconclusive, we did not find grounds to perform it. We also have to note that contamination can have other sources, like particles that break loose from the cylinder wall and travel to the surface. We can never really exclude it, although the cylinders are extensively cleaned before experiments.

4.4.2 Flow dissipation

The mechanical energy (eq.(2.44)) can be calculated in an Airy approach with boundary layer. We will compare to the forcing needed in a Mathieu theory 2.1.4 such that the growth is countered. For the kinetic energy we will only consider the potential contribution, such that we can relate to eq.(2.61) provided that we add the contribution from the wall boundary layer. The wall layer is given by eq.(2.66) and again we will only consider the period doubled frequency component as it is the largest for Mathieu excitation around $p = 1$, i.e. $\alpha \approx$

$i\omega_0/2$. We calculate eq.(2.43) from the first term as it is one order higher than the second one. First we approximate $\boldsymbol{\omega} = -\nabla^2 \boldsymbol{\Psi} \approx \xi^2 \boldsymbol{\Psi}$ and evaluate the integral for the fluid at rest.

$$|\boldsymbol{\omega}|^2 = |\xi^2 C \psi e^{\alpha t + \kappa z} J_1(\xi r)|^2 = 2\kappa^2 \phi^2 \left| \frac{\xi J_1(\xi r)}{L J_0(\xi L)} \right|^2 e^{2\kappa z}, \quad (4.1)$$

$$\nu(\boldsymbol{\omega}, \boldsymbol{\omega}) = 2\pi \cdot 2\nu\kappa^2 \phi^2 \int_0^L \left| \frac{\xi J_1(\xi r)}{L J_0(\xi L)} \right|^2 r dr \int_{-\infty}^0 e^{2\kappa z} dz = 2\pi\nu\kappa\xi_0^2 \phi^2, \quad (4.2)$$

where ξ_0 is a form factor determined by the radial integral. For our variables numerical integration approximates $\xi_0 \approx 260m^{-1}$ and $\xi_0 \approx 95m^{-1}$ for water and sunflower respectively. Eq.(2.61) becomes

$$(\mathbf{u}, \mathbf{N}) = 2\pi\phi \left(\ddot{T} + \bar{\Omega}^2 T + \{4\kappa^2 + \xi_0^2\} \nu \dot{T} \right) = 0, \quad (4.3)$$

which is a contribution of the same order. Now to transform the part within brackets to a dimensionless equation as in section 2.1

$$0 = \ddot{T}' + \frac{2\nu}{\omega_0} \{4\kappa^2 + \xi_0^2\} \dot{T}' + \frac{4}{\omega_0^2} \Omega^2 T' = \ddot{T}' + \beta \dot{T}' + \{p - 2q \cos 2t'\} T',$$

with β the constant dimensionless friction coefficient; for water $\beta = 0.0033$, for oil $\beta = 0.059$. Put new detuning $p' = p - \beta^2/4$ and $\alpha = \frac{1}{2}\sqrt{(q^2 - (p' - 1)^2)}$ from eq.(2.6).³ The argument of the of the period doubled component will be $(\alpha - \beta/2)t' = (\alpha - \beta/2)\omega_0 t/2$. We find growth (nonzero argument) for $f \geq 0.076$ and $f \geq 0.14$ for water and sunflower. If $p' = 1$ the values would have been $f \geq 0.0066$ and $f \geq 0.116$. Note that the dissipation outweighs the effect of a more favorable detuning.

In a comparison with experiment, we observe low sweep rate transitions the standing wave disappears around $f = 0.05$ and $f = 0.15$, which is in good agreement for oil and reasonable for water compared to the predicted contribution from the interior flow and wall boundary layer combined.

4.4.3 Dissipation experiments

Only for infinitesimal waves the dissipation is amplitude independent. We looked at the amplitude of the standing waves as a function of the excitation amplitude at the lowest sweep rate of $0.5g/s$. For water we can only do this for decreasing forcing amplitude because of jets found in the transition to a standing wave state. For oil the increasing forcing can be considered as well. A linear fit was very reasonable in all instances, like in figure 4.22. We calculated the dispersion for infinitesimal wave amplitudes in which case wetting effects should be absent. Therefore, the extrapolation of these lines to an amplitude of zero should correspond to the minimal excitation amplitude required, if the linear relation is valid for a larger interval. However, there was a large spread in the obtained values, while the calculated dissipation was always larger. For sunflower the absolute value of the steepness for decreasing forcing was larger

³ α will now be reserved for the Mathieu growth rate.

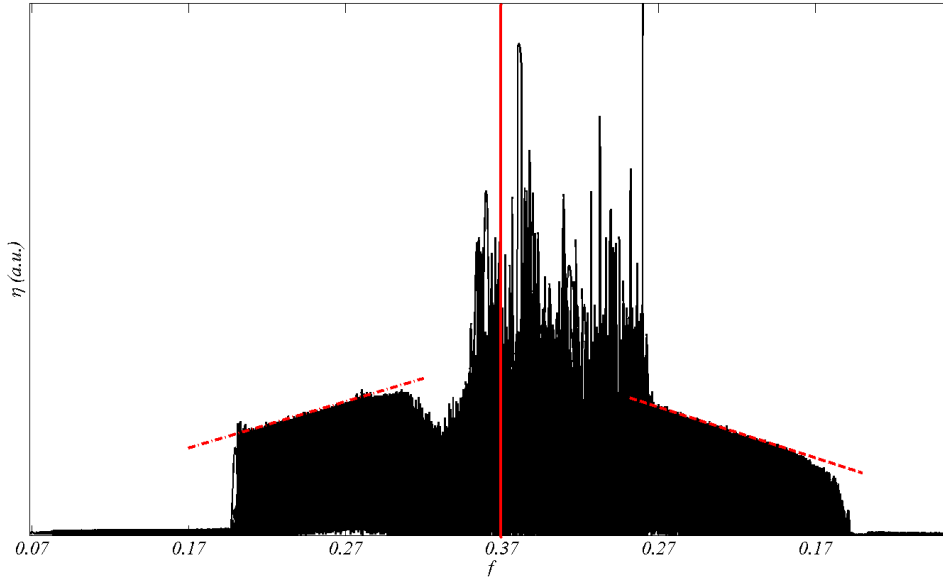


Figure 4.22: The response of the amplitude in sunflower for a sweep rate of $0.5mg/s$ (compare to figure 4.17). At $f = 0.37$ (solid red line) the direction was reversed. The red dashed lines are a fit to the standing wave regimes (approximately $0.20 \leq f \leq 0.28$). The line on the right is 9% steeper. The lower response around $f = 0.32$ is caused by asymmetric jets which are not fully captured by our recording system.

than for increasing forcing. We assume this is caused the growing wave wetting a new portion of the wall for increasing excitation.

Other comparisons are the decay of the wave when the excitation is abruptly stopped. In this experiment a standing wave in water at $f = 0.070$ and $p = 1.04$ was recorded and fitted to an exponential decay with transient frequency of $\exp((i\omega_t - \bar{\beta}/2)t)$ with data from 18 wave periods.⁴ We found $\bar{\beta}/2 = -0.40 \pm 0.03s^{-1}$ and $\omega_t = 4.39 \pm 0.02Hz$, strangely this is higher than the value from the dispersion relation, $\Omega = 4.28Hz$. The decay rate is also much larger than found at the beginning of this section $\bar{\beta}/2 = \beta\omega_0/4 = 0.043s^{-1}$. It has to be noted that the machine does not stop immediately and that the influence from the thin layer can be expected to be significant.

Henderson and Miles compared calculated dissipation with experiments with a fixed contact line, obtained by filling the cylinder up to its rim [46, 68]. In the (0,1) mode their model found a ratio of interior to the wall layer 1.64 but the measured dissipation was 1.3 times the total estimated value.⁵ Short wave

⁴ $\bar{\beta}$ has dimensions of one over second while β is the dimensionless friction coefficient.

⁵Note that a fixed contact line with a standing wave mode and overflow prevention implies very small amplitudes. The more flexible contact line leads to slightly different dynamics although the wavenumbers are identical. For instance, there is no report on meniscus waves.

experiments will likely show better agreement with calculated interior damping. So called walker droplets are able to trigger Faraday waves in the standing wave state [19, 34]. The surface waves decay over distance from the droplet such that wall effects can be neglected and the dissipation can be measured from the lateral profile.

We also performed experiments with an annulus tightly secured to the wall. Its height was 60mm and it was submerged in the fluid such that the fluid above the annulus was 2mm . In this way we hoped to minimize contact line movement in a standing wave state. However, it showed that an anti-node above the edge of the annulus could not be maintained for significant amplitude. The system transitioned into a standing wave in the entire cylinder. The dispersion can be found in the relation $\Omega(\kappa_1, h_1) = \Omega(\kappa_2, h_2)$ as the wave has different wavenumbers inside and above the annulus.

We have to note that the machine excitation is not very accurate, as mentioned before. At these small values of excitation the relative deviation from the demanded amplitude can be large, generally in the order of 10% at $f = 0.05$. A final notion is on the free surface. As frequencies or decay rates did not differ after a day, the elasticity of the surface did not change. This also suggests that the surface is not contaminated as mentioned before.

4.4.4 Wetting effects

The calculated dissipation for both fluids is in good agreement with experiment. Recordings in sunflower oil suggest that the contact line speed is negligible compared to the wave velocity at the wall, like in figure 4.23. This supports the hypothesis that the bulk fluid moving over the thin film is responsible for little dissipation. For water it is much harder to observe whether the contact

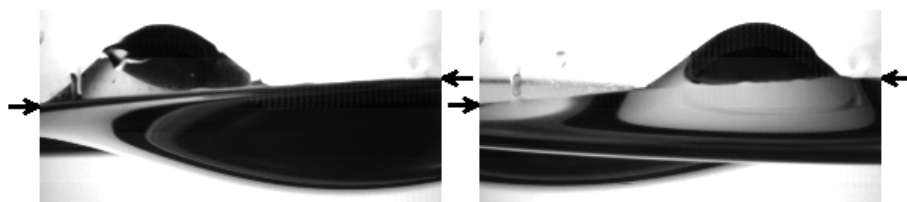


Figure 4.23: Two images of sunflower oil in a (1,2) standing wave state over half an interval of the fluid motion for $p = 1.01$ and $q = 0.145$. The arrows point at the contact line at the wall closest to the camera. It has not moved even in this asymmetric state.

line moves or is pinned. Recordings suggest the latter, but the thin film is near invisible. Experiments in a rectangular container show that the contact line does not move down with fluid immediately, as in the slip model, but they are not conclusive about the exact movement either. If the contact line slips for a small amount we have to consider the slip model for the velocity and distance of its motion. So it is important to determine its dynamics, if one is to estimate

this contribution to the dissipation accurately. To this end the profile of the film should be measured during Faraday experiments. This can for instance be done by reflectometry when the device is placed on the cylinder not to obstruct the camera's view. Also, the cylinder could be mounted in a rectangular container filled with the same liquid such that the film can be recorded.

4.5 Cavities and Jets

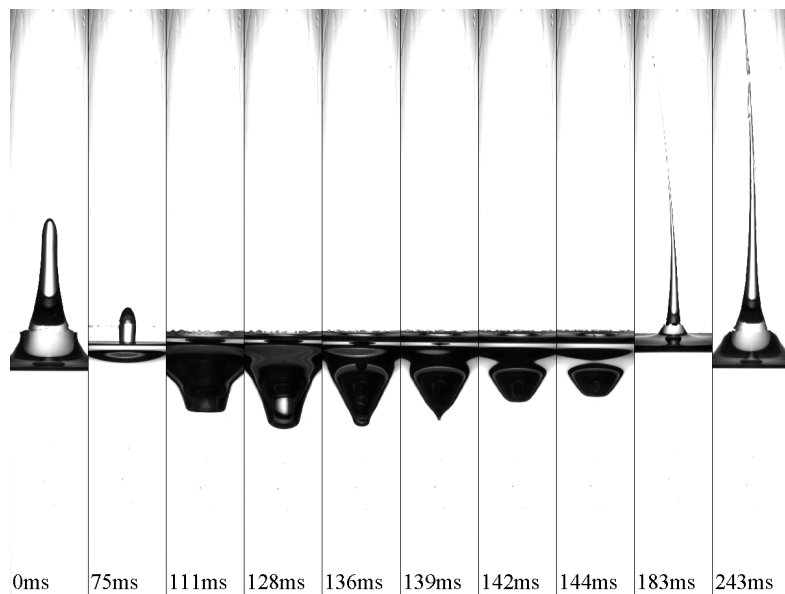


Figure 4.24: A cavity collapse with resulting jet in sunflower oil following a solid-body state at $q = 0.149$. In frame 4 part of the liquid column is still falling and the moment before the singularity is clearly visible in frame 6.

Jets are a very interesting phenomenon but somewhat hard to describe quantitatively. Different shapes and various jetting methods are classifiable and observed in experiment. We subscribe this to the random-like conditions prior to the mechanism, which are due to the long time for a cavity to form in our setup, since we do not control the exact wave motion when the system transitions into the jetting regime. For instance, the crest height and shape of the last wave can be different in similar runs. Further, the amplitude of the period-doubled component in Mathieu like motion can be slightly time depended. This requires us to perform a number of runs per parameter setting.

4.5.1 Transitions to jets

It is important to realize that jets occur following two types of transitions. We now know that the system reacts slowly to a change in excitation amplitude, so we can bring the system in a solid-body state with forcing of the jetting regime such that we can investigate the influence of the forcing on the jet. We know from the previous section that jets formed in this transition are more symmet-

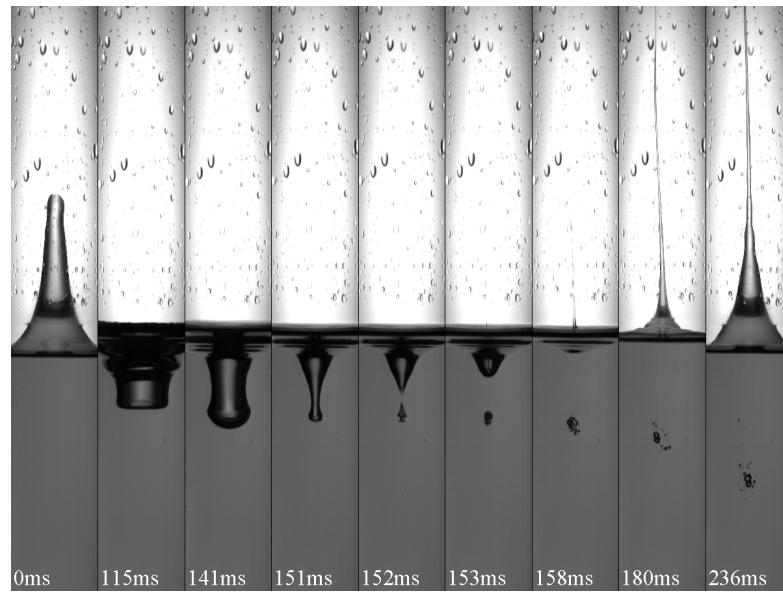


Figure 4.25: A cavity collapse with resulting jet in water following a solid-body state at $q = 0.125$. The cavity collapse is very close to a real pinch-off.

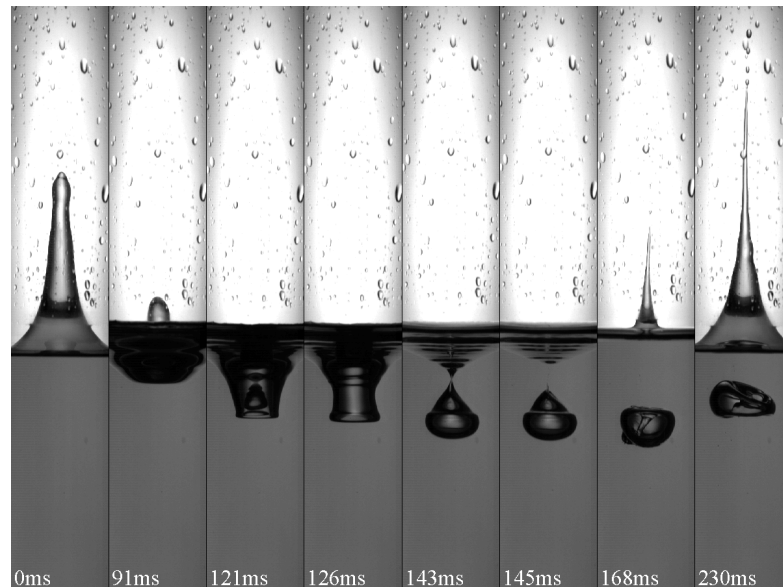


Figure 4.26: A pinch-off where the collapse is just moments later than the liquid column falling through (frames 3-5). The resulting jets are very fast; in frame 7 some smaller droplets reached the top of the image while the downward jet penetrates the bubble completely. Experiment in water following a solid-body state at $q = 0.125$.

ric. Hence we will primary use this desired transition. Again we take 8.400 and

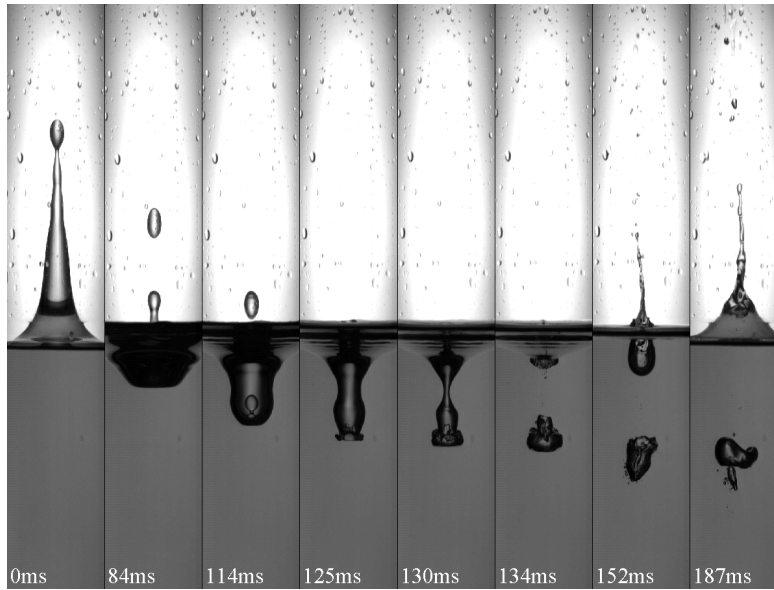


Figure 4.27: A falling liquid column with double droplet pinch-off. The second coalesces with the fluid before the cavity pinch-off (frame 4) while the first impacts on the jet (frame 6). The symmetry is not broken although the surface of the jet is irregular (frame 8). Experiment in water following a solid-body state at $q = 0.100$.

$8.303Hz$ in water and sunflower oil respectively and record the jet formed at two excitation values.

However, it was found that there is a limit of the forcing we could apply and still produce smooth jets. For instance, other modes would start to dominate the profile or air entrapment would happen before jet creation. To produce more extreme jets at the excitation of the machine limits we used a transition from the standing wave state. The forcing would be safely below the jetting regime ($f = 0.08$ and $f = 0.16$ for water and sunflower oil respectively) and the wave is maintained for $180s$ to reduce artifacts in the flow. Then the forcing is suddenly increased at the maximum possible rate. Apart from a non-ideal transition there are two downsides; the exact excitation is ill-defined and a rather long downtime is required for the air and fluid to separate as a mixture is created at these large amplitudes. The machine rate at our settings is approximately $1.2s^{-1}$ so the excitation increases with 0.15 per cycle. The machine limit was $f = 3$ but the jets are always formed for $f < 1.4$ with this method, since the fluid will react faster to the forcing in a standing wave state.

4.5.2 Morphology of collapsing cavities

The crest before the cavity determines most of the dynamics of cavity collapse. Large crests will be thin, long shaped and when it is over its maximum value it can be seen as a falling liquid column. It will interfere with the collapse of the cavity. Figures 4.24-4.30 show different kinds of collapsing types. They

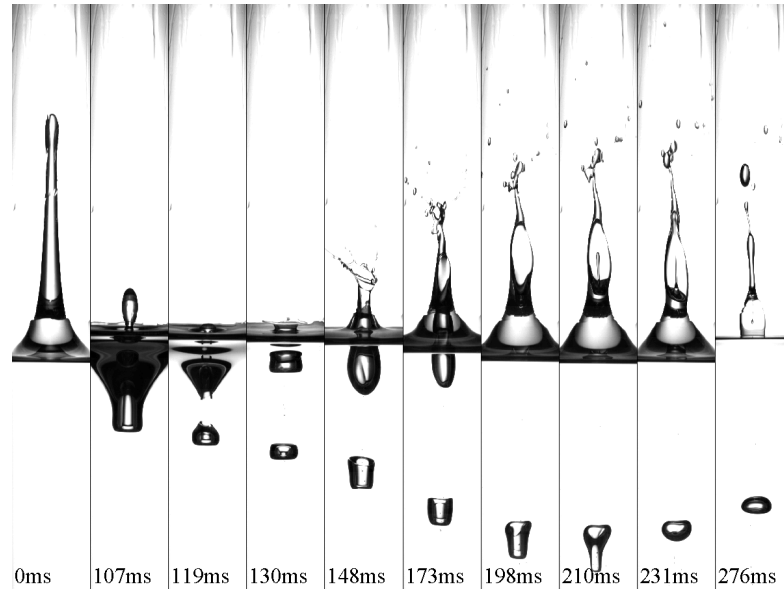


Figure 4.28: A cavity pinch-off in sunflower oil following a solid-body state at $q = 0.199$. The top of the falling column impacts the surface just after a jet is created (frame 3). Two things happen; the jet is in the shape of a hollow sheet with several secondary jets and satellite droplets emerging from the rim (frames 3-4). In frame 6 the rim is closed leading to a irregular shaped top and a hollow middle which reaches it maximum volume in frame 7. The other effect is the creation of a second cavity which collapses between frames 6-7. A second jet is created, moving upward in the hollow inside of the first jet (frame 8), eventually impacting on the tip of the first jet. Frame 9 is a few moments before the coalescence of both jets. The shape of the jets is reasonably conserved in downfall (frame 10).

are obtained from the method just described and the relative timing is given for each frame. 4.24 shows a normal collapse, while the others show increasing complications, producing rather astonishing pictures. The crests are heavily subject to Rayleigh instabilities. Extreme instances are when the curved top of the column detaches and forms a droplet. As expected, asymmetric collapse is found in the standing wave transition (4.31-4.30). The difference between the two liquids is large. Water shows more irregularities and fast jets are actually more like a spray. Sunflower oil has very smooth surfaces, but the jets can be so thin that they are near invisible. It also proved to be hard to find an ideal illumination of the experiment. Cavities need much light to be recorded but this can cause overexposure of the jets.

4.5.3 Tip velocity

Now that we found that the falling liquid column is of much importance we will look for a relations between the last crest and the jet. The maximum crest height can be easily measured and we will characterize the jet by its tip velocity. The latter is measured by dividing the change in vertical position by the expired

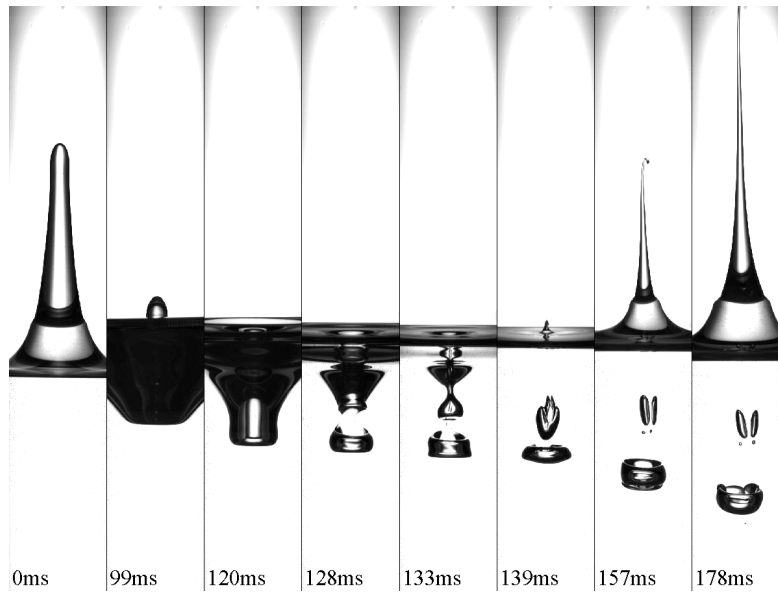


Figure 4.29: A double pinch-off in the cavity in sunflower oil following a standing wave state. The second pinch-off is a result of the droplet falling into the cavity before a jet is formed (frames 3-5). The pinch-offs are not entirely symmetrical, resulting in bended tip of the jet and secondary pinch-offs of both droplets.

time. If the tip of the jet was too fast to observe just above the fluid level the measured distances were the tip of the cavity or pinch-off and the jet tip at the top of the image. If there were complications with the falling column the velocity was undefined and set to zero. The measurement uncertainties are the exposure time for the time and two pixels for distances. The result is plotted in figures 4.32 and 4.33, with corresponding errorbars, where the width relates to the uncertainty in the crest height. The recordings of all jets are shown in figures 4.35-4.40. In all cases the crest at its maximum, the cavity and the jet are visualized. There is approximately one period of the forcing frequency in between the images.

The magnitude of the velocities and the trend are very similar for both fluids. There is an optimal crest height for which maximal velocities are reached ($49mm$ for water and $47mm$ for sunflower oil). We found that on the left there are cavity collapses and on the right are pinch-offs, while the transition between the regimes is not abrupt, like in figure 4.25. The jet speed increases with cavity depth, but if it is too deep it can not sustain itself and a pinch-off occurs resulting in a slower jet. The forcing does not influence the tip velocity in the cavity collapse regime. This suggests that the collapse mechanism is independent of gravitational forces. For sunflower oil there is a clear difference in the pinch-off regime where less excitation corresponds to slower jets. For water there are not enough data points in this area. The data points on the right relate to complicated collapses as expected for larger crest heights. Especially crests in sunflower oil are able to grow large without jetting first. This can also be a consequence of the larger driving amplitude required for this liquid. For

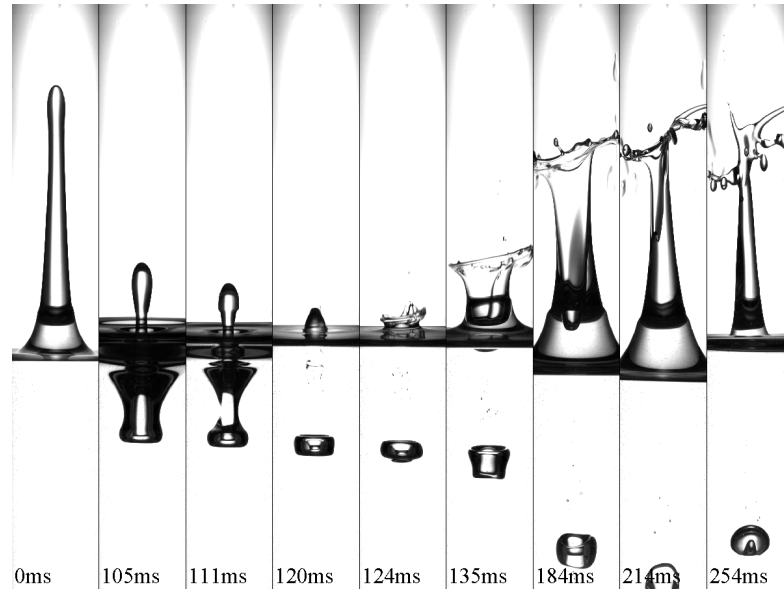


Figure 4.30: An asymmetric cavity pinch-off in sunflower oil following a standing wave state. The impact of the top of the column on the jet (frame 4) results in a crown like eruption. It is also asymmetric; the sheet does not completely encircle the air in the middle which is clearly visible in frames 6-7. It closes in frame 8 resulting in a small jet emerging from the top left of the rim. The rim is relatively stable without jets emerging from it in frames 5-7. When the jet closes under it, the rim rearranges in low velocity jets leading to a 'helicopter' jet.

water there is a data point for a large crest, at $73mm$, which corresponds to the series in figure 4.27. This shows that instabilities of the falling column do not necessarily disturb the jetting process. It appears that the experiments are randomly concentrated. There is no indication that the system prefers a certain regime. More experiments are required to confirm this and will result in a better coverage of the interval.

A similarity scaling was not found to be a good method in comparing cavity shapes. It is a method based on the assumption of a singularity, while we observe a large number of experiments where the surface collapse is only local, i.e. where only a small portion of the surface experiences large velocities. Zeff et al. denote such instances as near-singularities [95], such that only a small number of the considered experiments are real singularities. The profile of such a collapse is shown in figure 4.34. We could not find a good fit for the variables found in section 2.3.2, but our temporal and spatial resolution might not be large enough. On the other hand, we found that the tip velocity is independent on the forcing. The similarity scaling is independent of the gravity so also of the modified gravity in our Faraday system. This suggests that the similarity might be a correct approach to the shape of the collapsing cavities. Moreover, in the pinch-off regime the tip velocity depends on the forcing. For this regime the similarity scaling can be related to gravity if surface tension can be neglected

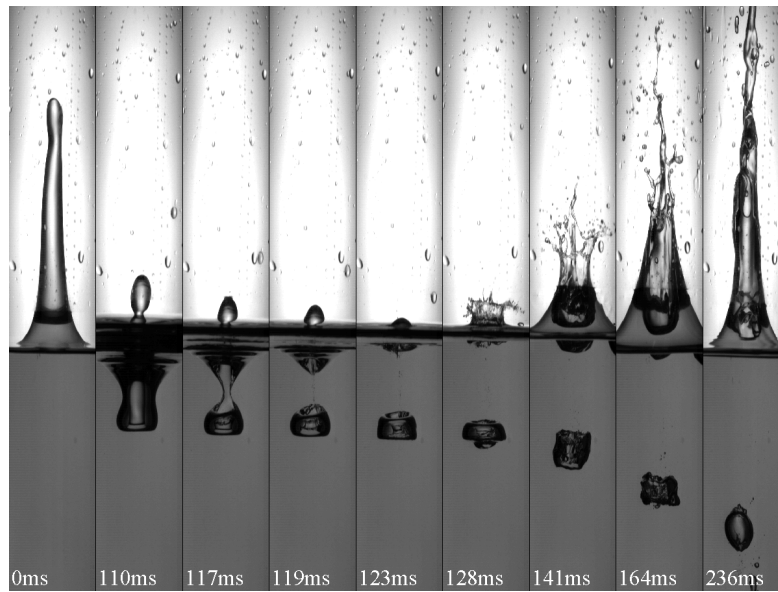


Figure 4.31: An asymmetric cavity pinch-off in water following a standing wave state. The impact of the top of the column on the jet (frame 5) results in a crown like eruption with a lot of secondary droplets. An irregular jet in the middle is also formed, catching up with the liquid sheet in frame 7 and finally coalescing with it in frame 9.

[41]. So both regimes actually agree with these properties of self-similarity solutions. We did not investigate if the solution fitted to the shapes in pinch-off regime.

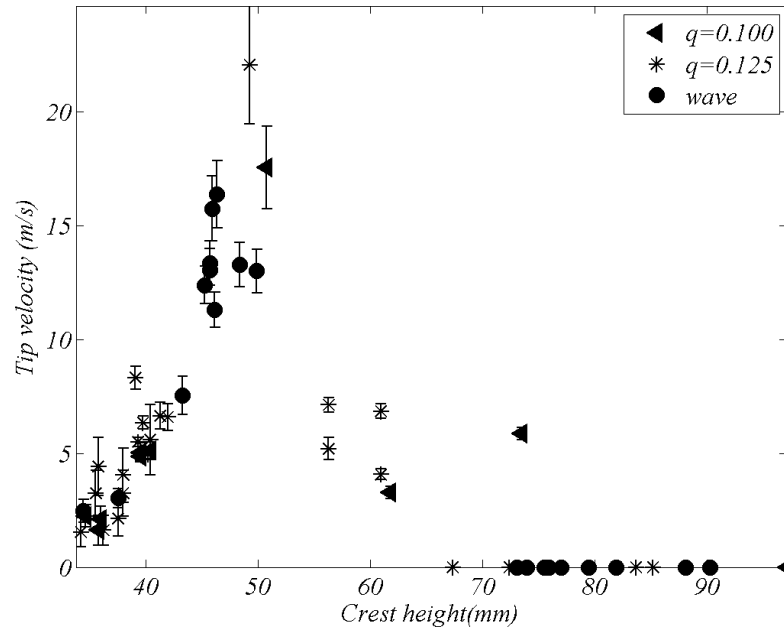


Figure 4.32: Tip velocity for jets in water.

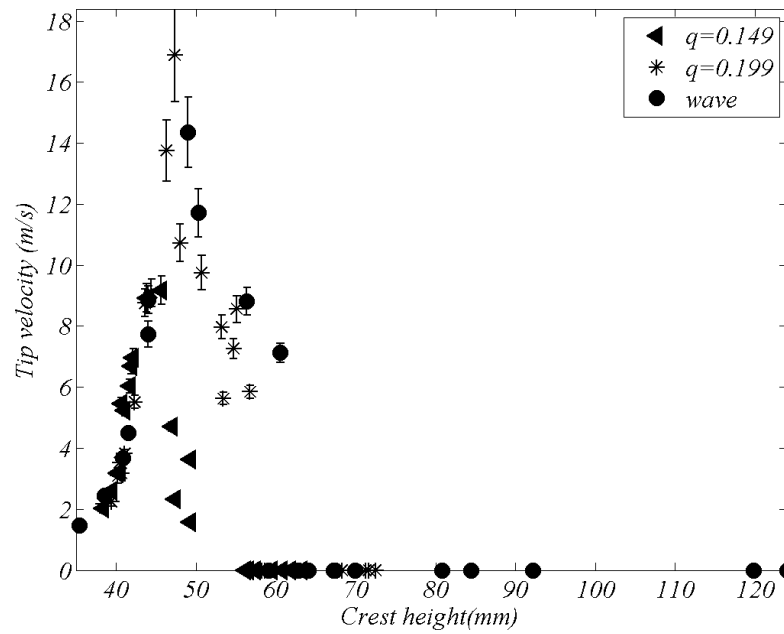


Figure 4.33: Tip velocity for jets in sunflower oil.

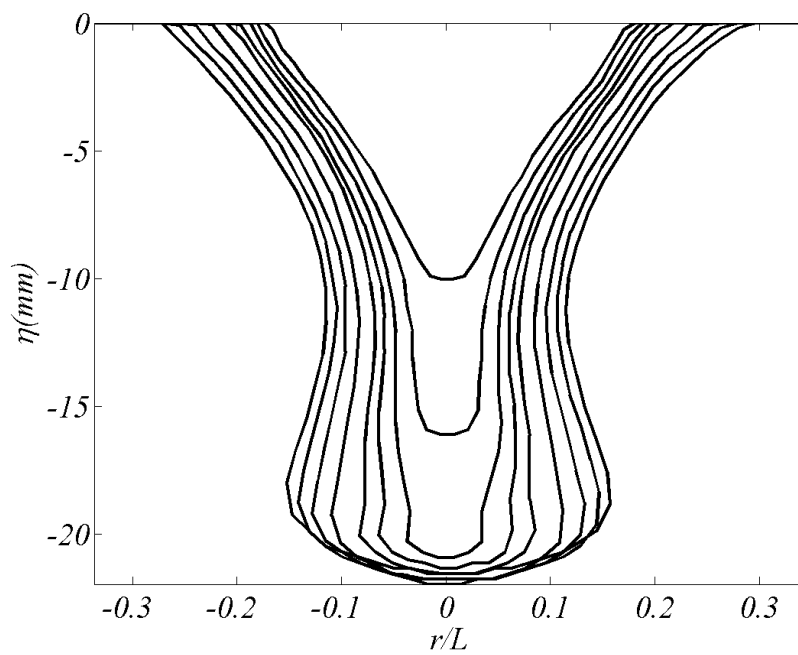


Figure 4.34: Extracted profiles of the cavity in sunflower oil for $q = 0.149$. Every profile closer to the center is at a later instance while the relative timing is $[0, 2, 4, 6, 8, 9, 10, 11, 12]$ s at 8.303Hz . This cavity is a real singularity as the resulting jet has a velocity of 9.2ms^{-1} .

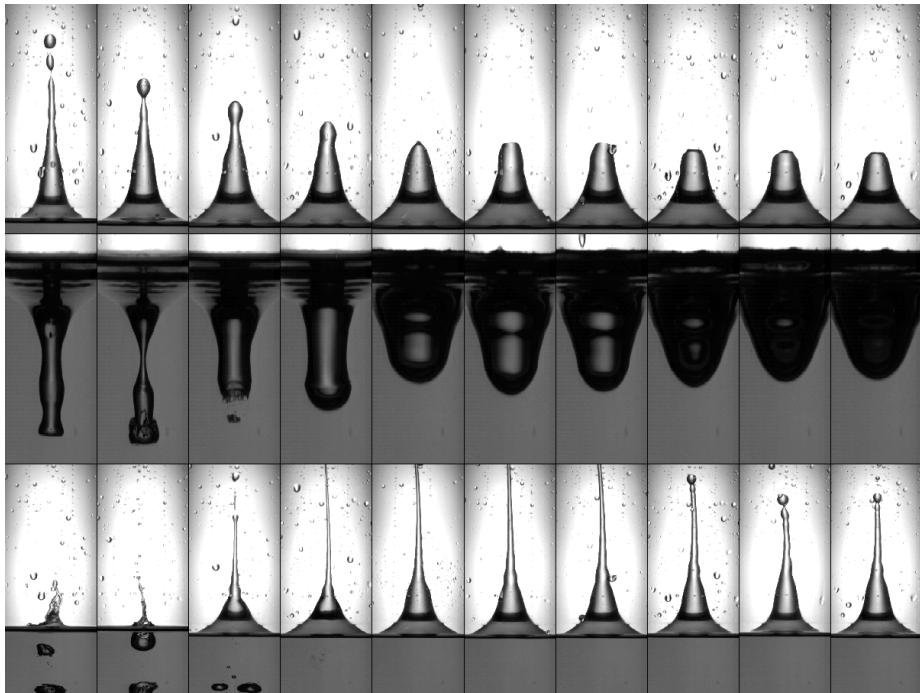


Figure 4.35: Largest crest, cavity and jets in water for $q = 0.100$.

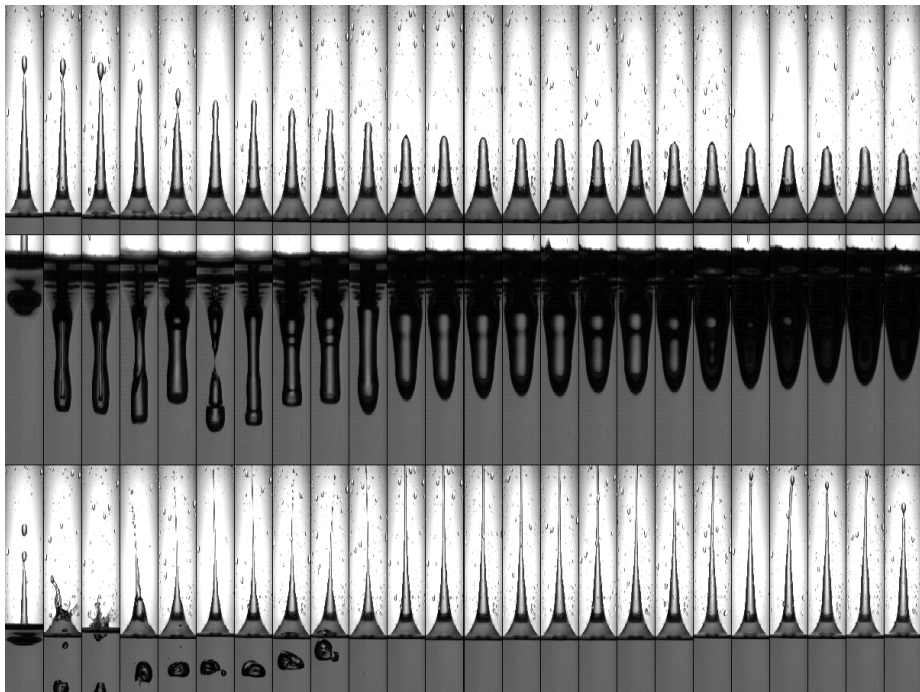


Figure 4.36: Largest crest, cavity and jets in water for $q = 0.125$.

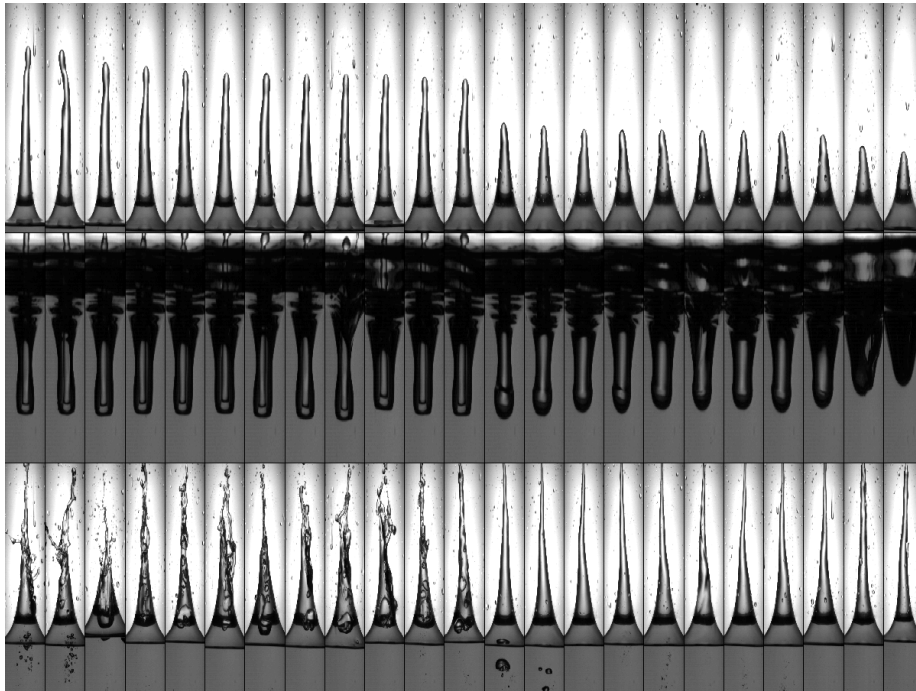


Figure 4.37: Largest crest, cavity and jets in water for the standing wave transition.

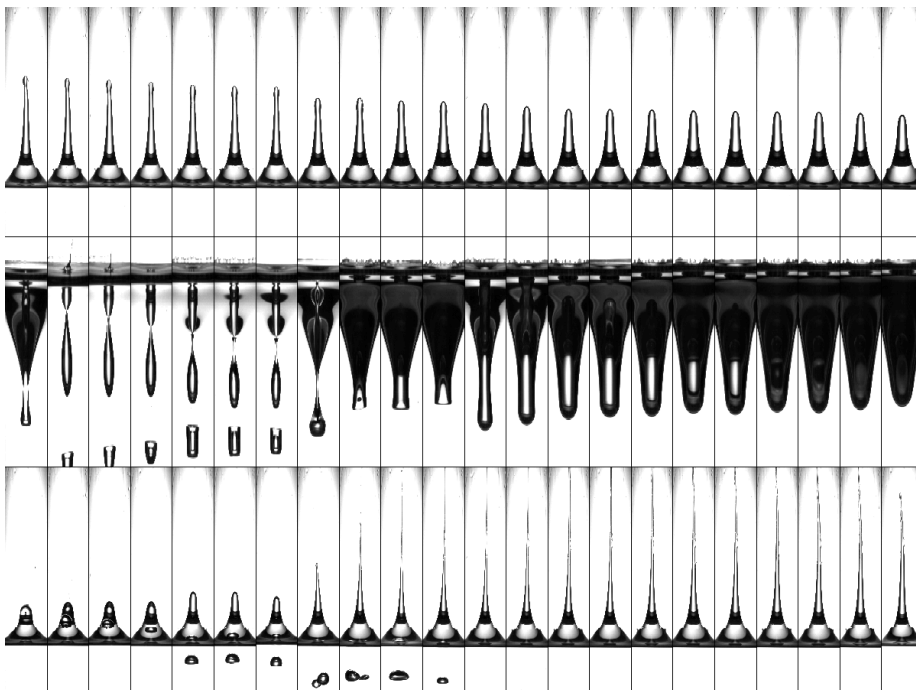


Figure 4.38: Largest crest, cavity and jets in sunflower oil for $q = 0.149$.

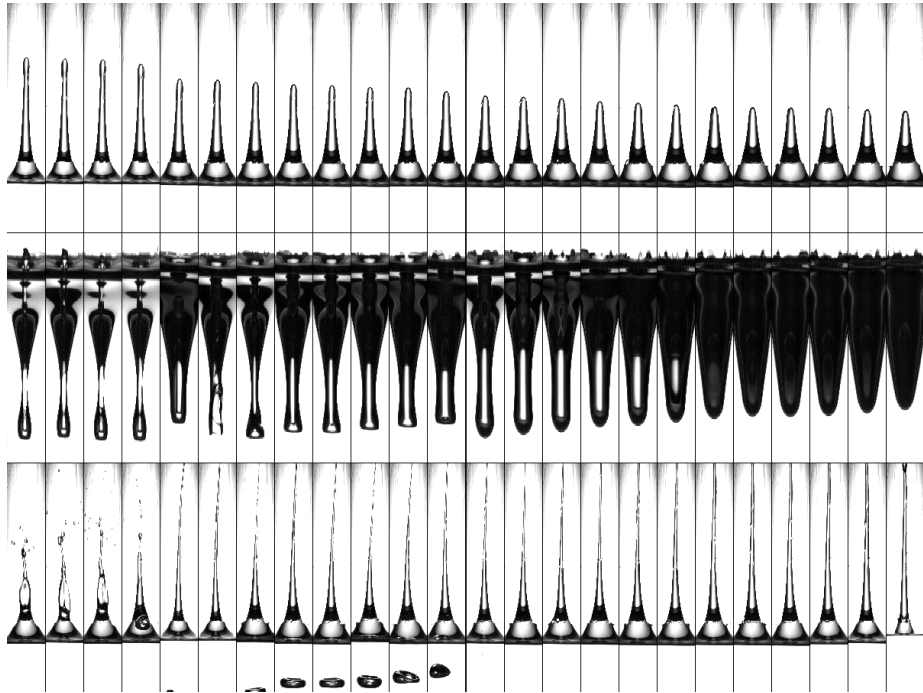


Figure 4.39: Largest crest, cavity and jets in sunflower oil for $q = 0.199$.

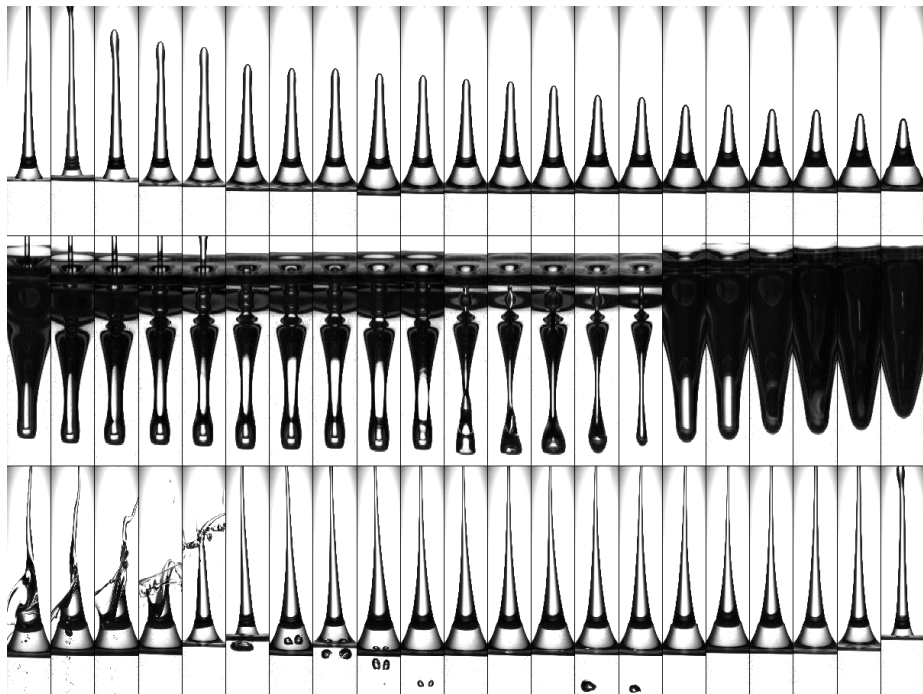


Figure 4.40: Largest crest, cavity and jets in sunflower oil for the standing wave transition.

Chapter 5

Numerical Aspects

In this chapter we will investigate numerical models appropriate for the dynamics of our system. In previous chapters we found that the largest part of the flow is irrotational. This is especially true in the center of the cylinder, where most of our measurements are focused on. However, nonlinearities are still significant as shown by figure 4.12. The period doubled component is the most dominant up to the collapse cavity. This periodic behavior suggest that they are still waves at these extreme appearances. We will first give a short background of surface wave modeling and describe the principles of our approach. The implementation of numerical operators is treated next.

5.1 Introduction

The key in numerical modeling is to produce the most accurate results at the lowest computational costs. In order to derive a decent model we should go analytically as far as the equations of motion can take us. A good principle is to eliminate all lateral coordinates from the equations, without destroying their influences on the flow. Physically motivated assumptions, like incompressibility, are necessary. Surface waves generally exploit irrotational flow. In applications, the viscously susceptible shorter waves are often of little interest as they are damped faster. Moreover, a vorticity-free fluid can often be assumed to remain irrotational during the experiment when there are no boundaries present, like in ocean modeling. One may often neglect tangential stress as well, such that the interface is a real free surface. In that case Bernoulli's principle can be evaluated at the surface. Luke proposed to interpret it as a Lagrangian function [63]. The equation is integrated over the lateral and temporal intervals to find an action functional. A problem with the evaluation of this integral is that the integration volume is not a nice strip as it depends on the surface elevation. To prevent implicit relations there are two main paths to go on. We already encountered the Airy approach where the surface deviation from the fluid at rest is neglected and a convenient integration interval can be used. Boussinesq proposed to use a Taylor series expansion to approximate variables at the surface in expansions of their values at the equilibrium position [10]. There are many Boussinesq-type models including the Kortewegde Vries equations [54]. Another method is to use a change of variables such that surface in the new coordinates is static. This

convenient goes at the expense of more complicated dynamics. Stokes used a conformal transformation to achieve this [59, 83].

We will begin with the separation of variables from section 2.2.5 and include all allowed radial wavenumbers, as given by eq.(2.53). We will limit the model to cylindrical symmetric motion, i.e. the azimuthal wavenumber (s) equals zero.

$$\Phi = \sum_{m=1}^M \hat{\phi}_m(t) R_m(r) Z_m(z), \quad (5.1)$$

$$\eta = \sum_{m=1}^M \hat{\eta}_m(t) R_m(r), \quad (5.2)$$

with $R_m = \sqrt{2}L^{-1}J_0(\kappa_m r)J_0^{-1}(\kappa_m L)$ and $Z_m = \exp(\kappa_m z)$. The truncation number M is necessary for discrete implementation, but is assumed to be infinite for now. We now would like to find a coupled differential system for the arrays $\hat{\phi} = [\hat{\phi}_1, \hat{\phi}_2, \dots]$ and $\hat{\eta} = [\hat{\eta}_1, \hat{\eta}_2, \dots]$. The wavenumber is an array as well, i.e. $\kappa = [\kappa_1, \kappa_2, \dots]$, which one can use to represent the arrays as a function of κ . We will denote corresponding transformations as $\eta \hat{=} \hat{\eta}$.

We will use (\cdot, \cdot) for the integration of the inner product over the entire volume, i.e. $(\mathbf{v1}, \mathbf{v2}) = \int_V (\mathbf{v1} \cdot \mathbf{v2}) dx$. Furthermore, let $\int_0^L f_1(r) f_2(r) r dr = (f_1, f_2)_r$ denote the integral of the multiplication of two scalar functions with weight r .

5.2 Transformations

These equations are actually transformation from the wavenumber space to the lateral space. We still need to deal with Z_n but for η it is clear that if one knows $\hat{\eta}(t, \kappa)$ one is able to find $\eta(t, r)$ by eq.(5.2). We will denote this relation as the backward transformation. The forward transformation is found in a similar way. Then for arbitrary $m > 0$,

$$(R_m, \eta)_r = (R_m, \sum_{n=1}^{\infty} \hat{\eta}_n R_n)_r = \hat{\eta}_m, \quad (5.3)$$

by the orthonormality of the Bessel functions. The difference between the transformations is that the wavenumbers are restricted while $r \in [0, L]$.

There is wavenumber equal to zero in this case. It can be included by letting the sum start at $n = 0$ while defining $\kappa_0 = 0$. This relates to the offset in the transformation since $J_0(0) = 1$. We require conservation of volume so the zero component of the elevation has to be zero, i.e. $\hat{\eta}_0 = 0$. For the potential the zero component corresponds to a constant, which has no physical meaning. Since numerical artifacts can excite this component, excluding κ_0 from the wavenumber array forces the our requirement on the system.

5.2.1 Implementation

The analogy with Fourier series is clear and our representation is known as the Fourier-Bessel expansion [11]. We can construct orthonormal basis functions

for other roots of Bessel functions, e.g. $J_0(\kappa L) = 0$.¹ Fourier transformations imply that the lateral and wavenumber interval is dense and unbounded.² The Fourier-Bessel analog is for $r \geq 0$ and $\kappa \geq 0$. In that case

$$\eta(r) = \int_0^\infty \hat{\eta}(\kappa) J_s(\kappa r) \kappa d\kappa, \quad (5.4)$$

$$\hat{\eta}(\kappa) = \int_0^\infty \eta(r) J_s(\kappa r) r dr, \quad (5.5)$$

since Bessel functions are originally designed to be normalized on this interval.

A discrete Fourier transform conserves the number of points in the lateral and wavenumber spaces in general. The arrays are often assumed to be equally spaced as well. This is straight-forward, as the waves or basis functions represent a signal between the grid points as well. The wave corresponding to the smallest nonzero wavenumber has a wavelength of two node distances and for the largest wave number it is the entire lateral interval. The transformation of a lateral array of length N involves a matrix of size $N \times N$. Properties of this square matrix can reduce the computation costs to order $N \log(N)$ instead of N^2 [18, 86].

The restriction on the wavenumber array in our case requires a thoughtful approach. We require a high resolution for r but this is not necessary for κ , since we expect the (0,1) mode and only a few harmonics to approximate the standing waves. In this way we can leave the forward transformation as in eq.(5.3) if we can calculate the integral for sufficient resolution. The transformation can be represented by $T = J_0(\kappa r)$, an $N \times M$ matrix, where N and M are the number of points in the lateral and wavenumber array. Then, in the discrete setting for an arbitrary lateral array h ,

$$\hat{h} = T \frac{2rh}{NL J_0^2(\kappa L)} = T_f h, \quad (5.6)$$

$$h = T^* \hat{h} = T_b \hat{h}. \quad (5.7)$$

All the weight of the normalization now is in the forward transformation, such that the amplitudes of the transformed signal relate to the original signal, i.e. $J_0(\kappa_n r) \hat{=} \delta_n$. The forward transformation involves element-by-element multiplication of the arrays h , r and $J_0^{-2}(\kappa L)$ all of length N , while the backward transformation needs the transpose of matrix. These operations can be included in the matrices such that we yield a simple matrix operation.

There may be instances that the radial derivative of the potential or elevation is needed, e.g. for the radial velocity. In a Cartesian system we can multiply the transformed signal by $i\kappa$, with $i = \sqrt{-1}$ to calculate derivatives, because the derivatives of cosines and sines are themselves. For Bessel function this is

¹Usually only a few zeros of the Bessel function are documented. To find higher orders we use an m-file exploiting Halley's method [92].

²More common is to apply Fourier transforms in temporal space and in its corresponding frequency space.

different since

$$\partial_r J_0(\kappa r) = -\kappa J_1(\kappa r).$$

Therefore it makes sense to introduce yet another transformation

$$\partial_r \eta = \sum_{m=1}^M \hat{\eta}_m(t) \dot{R}_m(r) = S_b \hat{\eta},$$

with the dot denoting the derivative. S_b is implemented similar to the normal backward transformation, eq.(5.7).

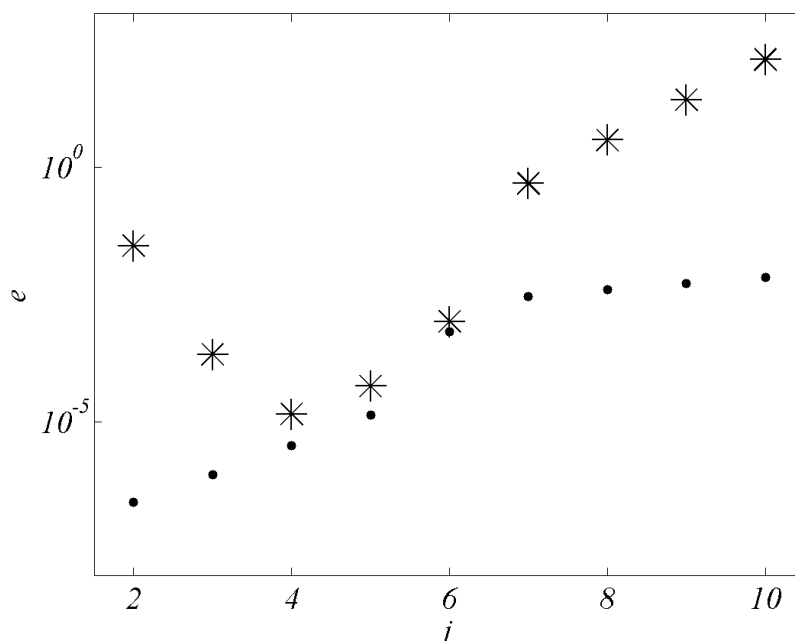


Figure 5.1: Logplot of the errors as function of the number of grid points in each space, $M = 2^j$, $N = 2^{12-j}$. The stars denote the transformation error (e_1) while the dots correspond to the inverseness of the matrices (e_2).

5.2.2 Testing

We experimented with the locations and spacing of the lateral array. We found that the best results were obtained for an equally spaced grid, i.e. the distance between points is $\Delta r = L/N$, and for locations $r = [\Delta r/2, 3\Delta r/2, \dots, L - \Delta r/2]$.

These transformations are tested for a function with wave properties, but that are not basis functions. For $L = 1$ and $h = \cos(6\pi r)$ we calculated the normalized error $e_1 = |h - T_b(T_f h)| / |h| / N$ and the 'inverseness' of the matrices $e_2 = |T_f T_b - I| / M^2$, with I the identity matrix. We know that for Fourier transformations this is of the order of the machine precision. We choose $M = 2^j$ and $N = 2^{12-j}$ such that the computation time is about the same in each run.

The error is plotted in figure 5.1 and the computation time was $42 \pm 8ms$ for these runs. We find that our implementation indeed requires a lot of lateral grid points for an accurate transformation. Artifacts are never completely absent which we describe to the nature of the transformation. Apparently Bessel-functions are not very nice functions.

5.3 A simple system

To find differential equations for both arrays we use the mechanical energy (eq.(2.44)) and the kinematic surface condition (eq.(2.25)). The first equation involves integration, while the second should be evaluated at the surface. Since it is a function of r the vertical integration should be performed first. In this implementation we use a Taylor expansion to approximate the domain while evaluating at $z = 0$.

We will treat the kinematic condition first as it is less complicated. In the potential case,

$$0 = D_t F = \partial_t \eta - \partial_z \Phi + \partial_r \eta \partial_r \Phi, \quad (5.8)$$

at the surface. This relation is already independent of z , since it is evaluated at $z = \eta$. However, the vertical flow matters as Z is still involved, which we approximate as

$$Z_m(\eta) \approx 1 + \kappa_m \eta + \frac{1}{2} \kappa_m^2 \eta^2 + \dots, \quad (5.9)$$

where the full surface elevation has to be taken into account. To eliminate the radial dependence an arbitrary basis function, R_m , is projected on this relation. For all $m \geq 1$

$$\begin{aligned} 0 &= (R_m, D_t F)_r \\ &= \left(R_m, \sum_{n=1}^M \partial_t \hat{\eta}_n R_n - \sum_{n=1}^M \hat{\phi}_n R_n \dot{Z}_n + \left(\sum_{n=1}^M \hat{\eta}_n \dot{R}_n \right) \left(\sum_{j=1}^M \hat{\phi}_j \dot{R}_j Z_j \right) \right)_r \\ &= \partial_t \hat{\eta}_m - \kappa_m \hat{\phi}_m - \left(R_m, \left(\sum_{n=1}^M \kappa_n^2 \hat{\phi}_n R_n \right) \left(\sum_{j=1}^M \hat{\eta}_j R_j \right) \right)_r - \dots \\ &+ \left(R_m, \left(\sum_{n=1}^M \hat{\eta}_n \dot{R}_n \right) \left(\sum_{j=1}^M \hat{\phi}_j \dot{R}_j \right) \right)_r + \dots, \end{aligned}$$

where another summation dummy (j) has been introduced for clarity. The higher order terms are potentially very complicated and expensive to implement.

In the second order the implementation will be

$$\partial_t \hat{\eta}_m = \kappa_m \hat{\phi}_m + T_f \left[((T_b \kappa^2 \hat{\phi})(T_b \hat{\eta}) - (S_b \hat{\eta})(S_b \hat{\phi})) \right], \quad (5.10)$$

which we will later use to test the system. To determine the evolution for the potential we have to use a test function for both the radial and vertical directions. Here we will evaluate $(\nabla(R_m Z_m), \mathbf{N})$ (see section 2.2.4). This is harder to treat than an integral over the pressure, where the equations of motion are found by variational calculus, like in Luke's variational method [63]. In this case, we want to include dissipation, which makes the problem more challenging. To simplify matters, we use a linear approach for the mechanical energy (eq.(2.44)) and approximate the boundary layer as in section 4.4.2. Other contributions to the dissipation are neglected. We already know all terms by the Airy approach (section 2.2.6) where all cross terms conveniently drop out due to orthogonality, except for the contribution from the wall layer, which is given by eq.(2.66). We will only consider the most dominant frequency component which we will assume to be the eigenfrequency of the mode, i.e. $\alpha \approx ig\kappa_n$. Then rotational terms can also be represented by the functions $J_1(\xi_n r)$ for $1 \leq n \leq M$ with $\xi_n = \sqrt{\kappa_n^2 - ig\kappa_n\nu^{-1}}$. Next we assume that the cross terms of these functions are small, such that they are almost orthogonal. Without dwelling too much on the details we obtain

$$0 = \partial_t \hat{\phi}_n + \nu \{4\kappa_n^2 + \xi_{0,n}^2\} \hat{\phi}_n + \bar{g}\hat{\eta}_n, \quad (5.11)$$

with $\xi_{0,n}^2$ form factors similar to section 4.4.2. They are evaluated numerically before solving the differential system. One of their properties is that they are monotonically increasing for increasing n approximately proportional to the square root of κ_n , which can be expected in this approximation. Together with eq.(5.10) this system can now be solved, which is done by Matlab's ode45. We implemented a cut-off wavenumber; components for $n \geq M/2$ are discarded at the end of every time step.

A result for sunflower oil, $f = 0.2$ with $M = 2^4$ and $N = 2^8$ is plotted in figure 5.2. Non-linear behavior, like larger crests and wider troughs are obtained. However, the system could not produce larger amplitudes than approximately 10mm, because the numerical implementation became unstable.

To improve the performance the equations could be expanded up to higher orders. However, it is unlikely that we are able to get close to a real cavity with this model. From experiments we observe that the crest and the cavity before jetting are always very steep, which is very difficult for the system to get at. In some instances the surface is even multivalued for r which is a shape these basis functions can never approximate.

5.4 Coordinate transformations

Here we will briefly consider numerical methods that are based on a coordinate transformation. Since the frequency response of the waves up to the cavity collapse is dominant in the period doubled component, a functional model seems to be possible. To approximate the steeper surfaces one should explore other possibilities. The following implementation is taken from [32, 31]. An viscous-free irrotational fluid in two-dimensional Cartesian coordinates is considered and the model is based on a conformal transformation, while dissipation can later be added in a phenomenological way. Another difference with our model

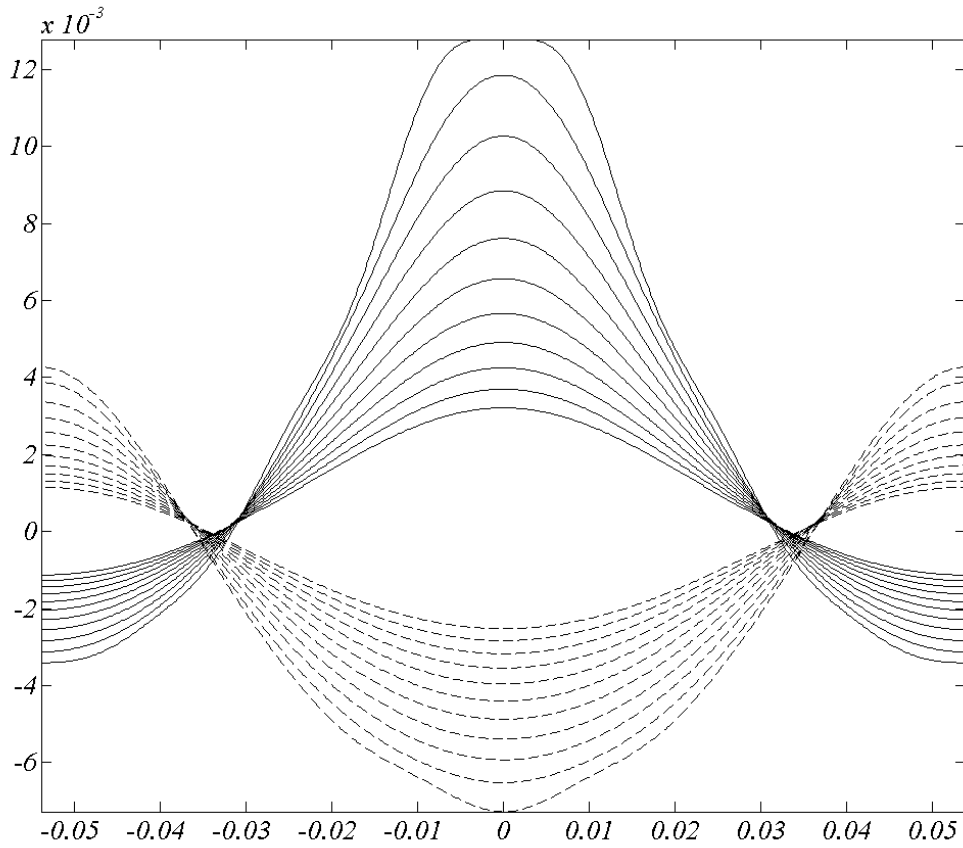


Figure 5.2: Surface profiles for sunflower oil for consecutive crests (solid) and troughs (dashed) at local extrema. The last crest is just before the system blows up. The horizontal axis denotes the radial coordinate while the vertical axis denotes the elevation. The profile is mirrored in the center.

is that surface tension is accounted for.

A result for water with $f = 0.2$ is plotted in figure 5.3 for 2^5 basis functions in water. Also in this case the nonlinear effects are clearly visible. Before the implementation becomes unstable the trough leaves the domain and the crest is intertwined with itself. This is of course unphysical. Indications of cavity formation are also absent for this method.

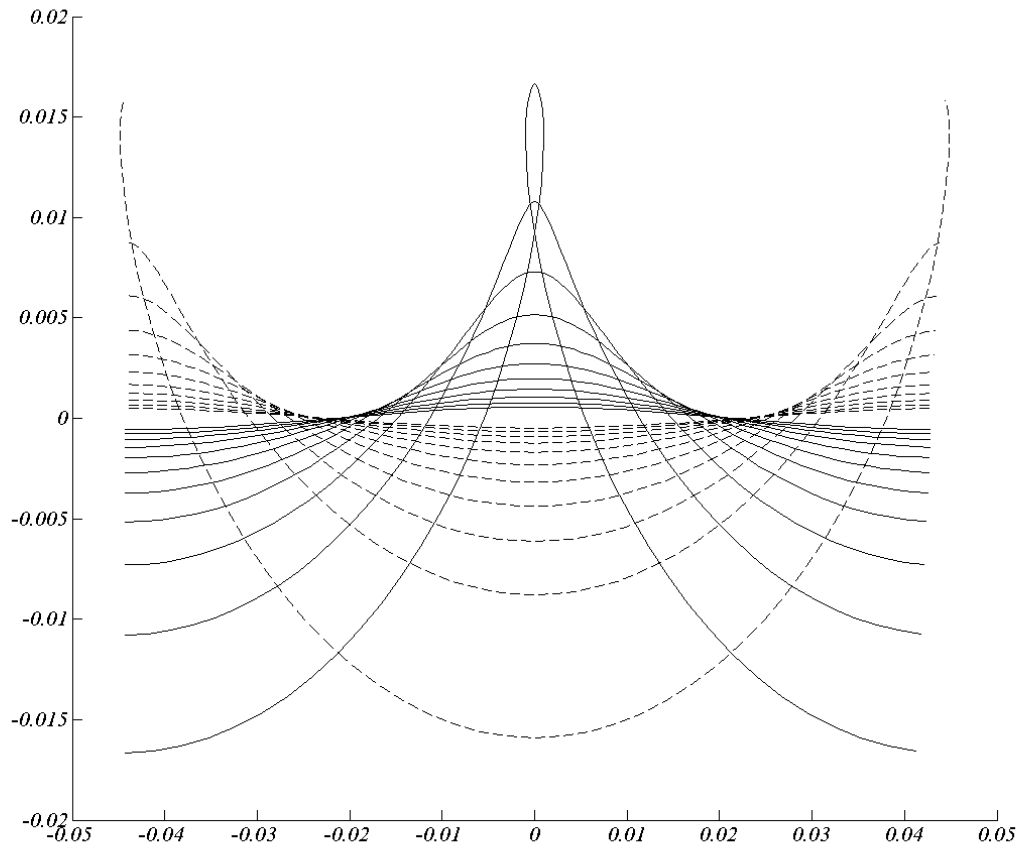


Figure 5.3: Surface profiles for water for consecutive crests (solid) and troughs (dashed) at local extrema. The last crest is intertwined, but the last trough is already outside the domain at the edges (which is responsible for the odd interval on the horizontal axis). The horizontal axis denotes the horizontal coordinate while the vertical axis denotes the elevation.

Chapter 6

Conclusion

In this thesis we investigated Faraday waves and jets theoretically, experimentally and numerically. In this final chapter we will provide discussions, conclusions and recommendations.

6.1 Discussion

Dissipation is a large factor in this project. Most of the phenomena are now in reasonable agreement with the estimated dissipation, especially for the majority of our experiments, which are slightly off-resonance at $p = 1.04$. Around $p = 1$ other experiments showed that there is much smaller growth than Mathieu theory predicts, like in figure 4.15. Hence, we must be cautious when applying this model to a larger parameter space, as we might have chosen an appropriate regime accidentally.

On the other hand, the experiments are surprisingly reproducible given the acceleration accuracy of the shaker at these small amplitudes and frequencies. The amplitude fluctuations are of course of a higher frequency that do not excite standing wave modes. Jets could occur after 20 to 100s for the same settings, which is very inconvenient experimentally, i.e. difficult to capture with the high speed imaging device, because we do not know when to trigger it in advance.

We considered clean water with food dye and sunflower oil as experimental fluids. There were chosen because they do not interact with the perplex cylinders or vapor in the air, like ethanol or glycerin. The downside of water is that it evaporates quickly which causes the ambient air to be of varying humidity. Both fluids are easily contaminated, which was minimized by sealing the cylinders. Also, considerable amounts of droplets could hang from the lid or walls, which can disturb the jet formation significantly upon impact. Especially in a continuous jetting state droplets would fall down regularly. A minor problem was that the temperature fluctuated, because of the high power equipment, like light sources and the shaker amplifier, resulting in slightly varying fluid properties.

6.2 Conclusion

Parametric excitation of a fluid in a cylindrical container is a convenient driving mechanism of non-linear standing waves. Linear analysis correctly predicted the excitation frequencies leading to amplitude growth and, ultimately, to jet formation. Besides the jetting state, the standing wave and solid-body state have been identified and all of the three regimes experience characteristic flow fields.

The fluids were considered to be Newtonian and incompressible with dynamic and impermeable boundaries. The Navier-Stokes equation was used to find the flow field of the fluid, which was found to be irrotational for the largest part. The liquid-air interface can be treated as an ideal free surface: there were no indications of contamination and a surface layer imposed by the no-stress condition was negligible.

Near the walls of the container rotational flow and wetting effects are important. The wall boundary layer was predicted to satisfy the no-slip condition. A linear estimation of the dissipation was in good agreement with experiment. The contributions of the interior flow field and the boundary layer, i.e. the irrotational and rotational motion respectively, were of the same order. The bottom of the container was assumed to be of no influence and there were no indications for it.

At the beginning of an experiment the wall is wetted up to the height of the meniscus. The capillary length varies due to the parametric oscillations which causes the meniscus to act as a wavemaker. The generated waves behave accordingly to linear dispersion and have been clearly observed in water. However, they are too small to be observed from a horizontal view point, due to the presence of the meniscus. The maximum amplitude of these waves was estimated in the order of 0.1mm by a comparison of their slope at the wall to the allowed interval, corresponding to the contact angle hysteresis.

For larger waves the contact line has to move to obey the restriction on the contact angle. However, it was predicted that this motion is met with large resistance, because the no-slip condition is violated. We assume that it is the main cause of hysteresis in the transition of the solid-body to the standing wave state, because the wall is already wetted in the backward transition. The full slip model can be used to calculate the required energy related the initial wetting, but we cannot relate it to the size of the hysteresis, i.e. the difference in excitation acceleration for the forward and backward transition.

When the bulk fluid recedes, the contact line does not move along and a thin film is formed. Experiments for sunflower oil confirm that it is even pinned at its new height compared to the interval of a period of fluid motion, but in water observations are inconclusive. However, this contact line is most likely to be pinned as well, since we found a negligible contact line velocity in an estimation based on the shear stress at the wall. Moreover, the dissipation in the film in the case of a pinned contact line is assumed to be small, while the contributions from interior and boundary layer flows are already sufficient. Also, the full-slip model does not predict hysteresis.

The second transition is from the standing wave to the continuous jetting state. There is also hysteresis in this transition, but considerable smaller. It is probably due to surface destruction, i.e. the dissipation for standing wave may be more efficient and continuous, whereas a destroyed surface profile initially grows without limitation, transitioning to a jet quickly and follows the same cycle again.

The jetting state is similar to the standing wave state in the sense that the period doubled component is dominant and that surface modes can be identified. We focused on the (0,1) mode, although jets in other modes were created as well. A variety of cavity collapses and corresponding jets have been observed, in which the difference between the pinch-off regime and real collapses is the most important. At their transition there is an optimum for the velocity of the tip of the jet, 22 and 17ms⁻¹ for water and sunflower respectively. The regimes and tip velocities can be related to the maximum height of the latest crest before jetting. The tip-velocity in the cavity regime does not depend on the forcing of the system. In the pinch-off regime lower forcing relates to lower tip velocities. Beyond the normal pinch-off regime Rayleigh instabilities complicates the collapsing mechanism.

A numerical method was based on the mechanical energy. However, the implementation was started too late in the project to produce adequate results. Nonlinear behavior was observed in a relatively simple model, but the properties of this approach remain largely unknown. Nevertheless, it is doubtful whether this implementation is able to get close to jet formation.

6.3 Recommendations

There are four parameters in the Faraday experiment. They are the excitation, sweep rate, sweep direction and frequency. We excluded the latter, which also restricted the sweep direction to two possibilities, namely increasing or decreasing excitation. We recommend to consider the entire parameter space around the (0,1) standing wave mode. As the largest part of the flow is irrotational only extracting the amplitude is sufficient in most cases. One could use other experimental techniques, like reflectometry, and save the amplitude as a one-dimensional array. This data can probably be analyzed in real time which could be connected to a high-speed camera and light sources to capture interesting dynamics.

Another experimental improvement is to measure the film thickness during the experiment. Reflectometry is a non-intrusive technique and it should be implemented in a way such that its construction is attached to the outside of the cylinder wall. Since we assume symmetric motion one such device is sufficient, perhaps two or three to be sure. Not only will this allow us to investigate the thin film but also the profile of the meniscus close to the wall, which should give better insight in the origin of meniscus waves. Actually, these phenomena deserve their own studies. The dynamics of standing waves moving over thin films and the generation of meniscus waves are both very interesting.

The Faraday waves in this setup were able to reproduce very exotic jets. Rayleigh instabilities on the crests led to droplets that fell inside the cavity, just before or after the collapse. Phenomena observed were double cavity pinch-offs, hollow jets with a smaller secondary jet on the inside and bubble breakup due to downward jets. Research into these extraordinary jets is worthwhile as well.

Acknowledgments

In het laatste gedeelte van mijn studie heb ik mogen werken aan een fascinerend onderwerp. Ik had dit project nooit zelfstandig kunnen doorlopen en wil een aantal mensen bedanken voor hun bijdrage en hulp.

Allereerst wil ik mijn directe begeleiders bedanken. Brenny en Devaraj, bedankt voor jullie input, suggesties en discussies. Ik weet dat ik vaak wilde plannen kan hebben, maar jullie hebben altijd de tijd genomen te luisteren en het project een meer realistischer richting op kunnen sturen. Ik ben erg dankbaar voor de mogelijkheid af te kunnen studeren in een gecombineerd project. Ik snap dat het niet altijd ideaal geweest moet zijn, echter bij de leerstoelen AAMP en PoF lag er de kans om op de overlap van de disciplines onderzoek te doen. Ik wil Detlef en Stephan bedanken vanuit deze leerstoelen in de afstudeercommissie plaats te nemen. Harold, toen ik zeven en een half jaar geleden begon met studeren, was je al mijn mentor en ik heb je begeleiding toen als erg prettig ervaren. Je had altijd tijd voor studenten en zelfs aan het eind van mijn studietijd ben je bereid plaats te nemen in de afstudeercommissie als extern lid.

De experimenten zouden niet to stand zijn gekomen met de hulp van de technici Gert-Wim, Martin en Bas. Ik was erg blij met de snelheid en kwaliteit van jullie werk. Ceyda en Stefan hebben me erg geholpen met de opstelling en voornamelijk met de shaker, een apparaat dat een speciaal karakter heeft. Dank gaat ook uit naar de leerstoel Physics of Complex Fluids voor het gebruik van hun lab en meetapparatuur, in het bijzonder het contacthoek meetsysteem. Voor dit onderdeel wil ik in het speciaal mijn collega Bram noemen voor de introductie en bediening van de apparatuur. Onze discussies over oppervlaktespanning en vrije oppervlaktes waren erg waardevol.

Ik ben ook dankbaar voor de algehele gastvrijheid en sfeer op de Universiteit Twente. Bij beide leerstoelen was ik altijd welkom en ik wil in het bijzonder mijn kamergenoten bedanken voor de hoge kwaliteit van werken en studeren. Er was altijd de mogelijkheid problemen te discussieren, onszelf aan elkaar op te trekken en de nodige ontspanning te creëren. In dat opzicht heb ik ook genoten van mijn carrière als zaalvoetballer in PoF United. Ik ga ervanuit dat we dit seizoen wederom kampioen worden.

Vanaf het begin van dit project was ik erg gegrepen door de vele aspecten van Faraday golven. Ik ben nog steeds erg onder de indruk hoe een systeem aangedreven onder alledaagse instellingen toch extreme verschijnselen zoals jets kan produceren. Daarnaast heb ik veel geleerd over vloeistoffen en golven in een

gevoelsmatig opzicht. Bijvoorbeeld, waar ik voorheen erg sceptisch was over grenslagen, begrijp ik nu, naar eigen zeggen, wat het idee erachter is en hoe je ze hoort uit te buiten. Ik moest het concept echt zelf een keer tegenkomen en ermee worstelen, voordat dit zover was.

Ook het opereren op het raakvlak tussen natuur- en wiskunde een avontuur op zich. In het lab of bij bepaalde benaderingen ben ik zelden tevreden over de onzekerheid. Aan de andere kant heb ik weinig waardering voor het eerst aantonen dat een bepaalde operatie uitgevoerd mag worden alvorens het eerst te proberen. Toepasselijk lijkt mij een citaat van Abraham and Marsden ¹ over de dogma van stabiliteit: *as these parameters can be determined only approximately, the theory is useful only if the equations are structurally stable, which cannot be proved in many important cases. Probable the physicist must rely on faith at this point, analogous to the faith of a mathematician in the consistency of set theory.*"

Tenslotte wil ik de enorme steun en motivatie benadrukken die ik van mijn vrienden en familie heb mogen ontvangen. Ik heb me erg kunnen optrekken aan Jan-Jaap en Pascal, studenten die ongeveer tegelijkertijd dezelfde fases van het afstuderen doorliepen als ik. Tessa, Maria en Pim, ik wil jullie speciaal bedanken voor jullie toegewijde ondersteuning. Ik besef dat ik deze prestatie uiteindelijk voor het grootste deel aan jullie te danken heb. Als laatste, Ellis, jouw onvoorwaardelijke zorg en aanmoedigingen waren onmisbaar en ik ben erg blij met jou in mijn leven.

¹Foundations of Mechanics, Benjamin Cummings, 1978, second edition

Bibliography

- [1] G.B. Airy. Tides and waves. *Encyclopaedia Metropolitana. Mixed Sciences*, 3:1817–1845, 1841.
- [2] A. Antkowiak, N. Bremond, S. Le Dizes, and E. Villiermaux. Short-term dynamics of a density interface following an impact. *Journal of Fluid Mechanics*, 577:241–250, 2007.
- [3] G.B. Arfken and H.J. Weber. *Mathematical Methods for Physicists*. Academic Press, San Diego, USA, fourth edition, 1995.
- [4] Unknown Author. Unknown title, 2012.
- [5] G.I. Barenblatt. *Similarity, self-similarity, and intermediate asymptotics*. Cambridge University Press (original Russian, by Gidrometeoizdat Press, Moscow, 1978), Cambridge, UK, 1996.
- [6] T.B. Benjamin and F. Ursell. The stability of the plane free surface of a liquid in vertical periodic motion. *Proceedings of the Royal Society (London) A*, 225:505–515, 1954.
- [7] R. Bergmann, E. de Jong, J.B. Choimet, R.M. van der Meer, and D. Lohse. The origin of the tubular jet. *Journal of Fluid Mechanics*, 600:19–43, 2008.
- [8] J. Beyer and R. Friedrich. Faraday instabilities: linear analysis for viscous fluids. *Physical Review E*, 51:1162–1168, 1995.
- [9] J. M. Boulton-Stone and J. R. Blake. Gas bubbles bursting at a free surface. *Journal of Fluid Mechanics*, 254:437–466, 1993.
- [10] M.J. Boussinesq. Théorie des ondes et des remous qui se propagent le long d’un canal rectangulaire horizontal, en communiquant au liquide contenu dans ce canal des vitesses sensiblement pareilles de la surface au fond. *Journal de Mathématiques Pures et Appliquées*, 17:55–108, 1872.
- [11] F. Bowman. *Introduction to Bessel functions*. Dover, 1938.
- [12] M. P. Brenner, J. Eggers, K. Joseph, S.R. Nagel, and X.D. Shi. Breakdown of scaling in droplet fission at high Reynolds number. *Physics of Fluids*, 1573–1590:9, 1997.
- [13] D.V. Chalikov. The numerical simulation of wind-wave interaction. *Journal of Fluid Mechanics*, 87:561–582, 1987.

- [14] D.V. Chalikov. Interactive modeling of surface waves and boundary layer. *Ocean Wave Measurements and Analysis, ASCE*, pages 1525–40, 1998.
- [15] D.V. Chalikov and S. Rainchik. Modeling extreme waves based on equations of potential. *Journal of Computational Physics*, 210:247–273, 2005.
- [16] D.V. Chalikov and S. Rainchik. Coupled numerical modelling of wind and waves. *Boundary-Layer Meteorol*, 138:1–41, 2011.
- [17] S. Chandrasekhar. *Hydrodynamic and hydromagnetic stability, ch.91*. Clarendon, Oxford, UK, 1961.
- [18] J.W. Cooley and J.W. Tukey. An algorithm for the machine calculation. *Mathematcis*, 19:297–301, 1965.
- [19] Y. Couder, S. Protière, E. Fort, and A. Boudaoud. Walking and orbiting droplets. *Nature*, 437:208, 2005.
- [20] A.D.D. Craik. The origins of water wave theory. *Annual Review of Fluid Mechanics*, 36:1–28, 2004.
- [21] G.D. Crapper. An exact solution for progressive capillary waves of arbitrary amplitude. *Journal of fluid mechanics*, 2:532–540, 1957.
- [22] P.G. de Gennes, F. Brochard-Wyart, and D. Quéré. *Capillarity and wetting Phenomena (orig. Gouttes, bulles, perles et ondes, 2002)*. Springer, New York, USA, 2004.
- [23] H.J. de Jong. The tubular jet. Master’s thesis, University of Twente, 2005.
- [24] A. de Ryck and D. Quéré. Gravity and inertia effects in plate coating. *Journal of Colloid and Interface Science*, 203:278–285, 1998.
- [25] S.P. Decent and D.D. Craik. Hysteresis in Faraday resonance. *Journal of Fluid Mechanics*, 293:237–268, 1995.
- [26] G. Delon, M. Fermigier, J.H. Snoeijer, and B. Andreotti. Relaxation of a dewetting contact line. Part 2. Experiments. *Journal of Fluid Mechanics*, 604:55–75, 2008.
- [27] B. Derjaguin. On the thickness of the liquid film adhering to the walls of a vessel after emptying. *Acta Physicochim. URSS*, 20, 1945.
- [28] A.A. Dimas and G.S. Triantafyllou. Nonlinear interaction of shear flow with a free surface. *Journal of Fluid Mechanics*, 260:211–246, 1994.
- [29] P.A.M. Dirac. *General Theory of Relativity*. Princeton University Press, 1975.
- [30] S. Douady. Experimental study of Faraday instability. *Journal of Fluid Mechanics*, 221:383–409, 1990.
- [31] A.I. Dyachenko, E.A. Kuznetsov, M.D. Spector, and V.E. Zakharov. Analytical description of the free surface dynamics of an ideal fluid. *Physics Letters A*, 221:73–79, 1996.

- [32] A.I. Dyachenko, Y.V. Lvov, and V.E. Zakharov. Five-wave interaction on the surface of deep fluid. *Physica D*, 87:233–261, 1995.
- [33] A.I. Dyachenko and V.E. Zakharov. Toward an integrable model of deep water. *Physics Letters A*, 221:80–84, 1996.
- [34] A. Eddi, E. Sultan, J. Moukhtar, E. Fort, M. Rossi, and Y. Couder. Information stored in Faraday waves: the origin of a path memory. *Journal of Fluid Mechanics*, 674:433–463, 2011.
- [35] D.A. Edwards, H. Brenner, and D.T. Wasan. *Interfacial Transport Processes and Rheology*. Butterworth-Heinemann, 1991.
- [36] W.S. Edwards and S. Fauve. Patterns and quasi-patterns in the Faraday experiment. *Journal of Fluid Mechanics*, 278:123–148, 1994.
- [37] J. Eggers. Universal pinching of 3d axisymmetric free-surface flow. *Physical Review Letters*, 71:3458–3460, 1993.
- [38] J. Eggers and T.F. Dupont. Drop formation in a one-dimensional approximation of the Navier-Stokes equation. *Journal of Fluid Mechanics*, 262:205–221, 1994.
- [39] M. Faraday. On a peculiar class of acoustical figures; and on certain forms assumed by a group of particles upon vibrating elastic surfaces. *Philosophical transactions of the Royal Society (London)*, 121:299–318, 1831.
- [40] S. Gekle, I.R. Peters, J.M. Gordillo, D. van der Meer, and D. Lohse. Supersonic air flow due to solid-liquid impact. *Physical Review Letters*, 104:024501, 2010.
- [41] S. Gekle, A. van der Bos, R. Bergmann, D. van der Meer, and D. Lohse. Non-continuous Froude number scaling for the closure depth of a cylinder cavity. *Physical Review Letters*, 100:084502–1–4, 2008.
- [42] Stephan Gekle, José Manuel Gordillo, Devaraj van der Meer, and Detlef Lohse. High-speed jet formation after solid object impact. *Physical Review Letters*, 102(3):034502, Jan 2009.
- [43] J.M. Gordillo. Axisymmetric bubble pinch-off at high reynolds numbers. *Physical Review Letters*, 95:194501, 2005.
- [44] J.M. Gordillo and S. Gekle. Generation and breakup of worthington jets after cavity collapse. part 2. tip breakup of stretched jets. *Journal of Fluid Mechanics*, 663:331–346, 2012.
- [45] S. Granick, Y. Zhu, and H. Lee. Slipery questions about complex fluids flowing past solids. *Nature Materials*, 2:221–227, 2003.
- [46] D.M. Henderson and J.W. Miles. Surface-wave damping in a circular cylinder with a fixed contact line. *Journal of Fluid Mechanics*, 275:285–299, 1994.
- [47] J.E. Hogrefe, N.L. Peffley, C.L. Goodridge, W.T. Shi, H.G.E. Hentschel, and D.P. Lathrop. Power-law singularities in gravity-capillary waves. *Physica D*, 1998.

- [48] A. Iafrati and A.A. Korobkin. Initial stage of flat plate impact onto liquid free surface. *Physics of Fluids*, 16:2214, 2004.
- [49] H. Jeffreys. The draining of a vertical plate. *Mathematical Proceedings of the Cambridge Philosophical Society*, 26:204, 1930.
- [50] V.A. Kalinichenko. Breaking of Faraday waves and jet launch formation. *Fluid dynamics*, 44:577–586, 2009.
- [51] J.B. Keller. Capillary waves on a vertical jet. *Journal of Fluid Mechanics*, 135:171–173, 1983.
- [52] J.B. Keller and M.J. Miksis. Surface tension driven flows. *Siam journal of applied mathematics*, 43:268–277, 1983.
- [53] G.H. Keulegan. Energy dissipation in standing waves in rectangular basins. *Journal of Fluid Mechanics*, 6:33–50, 1959.
- [54] D.J. Korteweg and G. de Vries. On the change of form of long waves advancing in a rectangular canal, and on a new type of long stationary waves. *Philosophical Magazine*, 39:422–443, 1895.
- [55] K. Kumar and L.S. Tuckerman. Parametric instability of the interface between two fluids. *Journal of Fluid Mechanics*, 279:49–68, 1994.
- [56] P.K. Kundu and I.M. Cohen. *Fluid Mechanics*. Elsevier, San Diego, USA, fourth edition, 2004.
- [57] Sir H. Lamb. *Hydrodynamics*. Dover Publications, 1932.
- [58] L. D. Landau and B.V. Levich. Dragging of a liquid by a moving plate. *Acta Physicochim. URSS*, 17:42–54, 1942.
- [59] B. Lautrup. *Physics of Continuous Matter*. CRC Press, second edition, 2011.
- [60] V.G. Levich. *Physicochemical hydrodynamics*. Prentice-Hall (original Russian text), Englewood Cliffs, USA, 1962.
- [61] M.S. Longuet-Higgins. Bubbles, breaking waves and hyperbolic jets at a free surface. *Journal of fluid mechanics*, 127:103–121, 1983.
- [62] E. Lorenceau, D. Quéré, and J.Y. Ollitrault. Gravitational oscillations of a liquid column in a pipe. *Physics of Fluids*, 14:1985–1992, 2002.
- [63] J.C. Luke. A variational principle for a fluid with a free surface. *Journal of Fluid Mechanics*, 27:395–397, 1967.
- [64] M. Maleki, m. Reyssat, F. Restago, D. Quéré, and C. Clanet. Landau-Levich menisci. *Journal of Colloid and Interface Science*, 254:359–363, 2011.
- [65] V.A. Marchenko. *Sturm-Liouville operators and applications*. American Mathematical Society, second edition, 1986.
- [66] E. Mathieu. Mémoire sur le mouvement vibratoire d’une membrane de forme elliptique. *Journal des Mathématiques Pures et Appliquées*, pages 137–203, 1868.

- [67] N.W. McLachlan. *Theory and application of Mathieu functions*. Dover, New York, USA, 1947.
- [68] J. W. Miles and D. M. Henderson. A note on interior vs. boundary-layer damping of surface waves in a circular cylinder. *Journal of Fluid Mechanics*, 364:319–323, 1998.
- [69] J.W. Miles. Surface-wave damping in closed basins. *Proceedings of the Royal Society of London A*, 297:459–475, 1967.
- [70] J.W. Miles. Nonlinear surface waves in closed basins. *Journal of Fluid Mechanics*, 75:419–448, 1976.
- [71] J.W. Miles. Nonlinear Faraday resonance. *Journal of Fluid Mechanics*, 146:285–302, 1984.
- [72] J.W. Miles. A note on surface films and surface waves. *Wave Motion*, 13:303–306, 1991.
- [73] J.W. Miles. On Faraday waves. *Journal of Fluid Mechanics*, 248:671–683, 1993.
- [74] J.W. Miles. On Faraday resonance of a viscous liquid. *Journal of Fluid Mechanics*, 395:321–325, 1999.
- [75] S.T. Milner. Square patterns and secondary instabilities in driven capillary waves. *Journal of Fluid Mechanics*, 225:81–100, 1991.
- [76] G. D. Nadkarni and S. Garoff. An investigation of microscopic aspects of contact angle hysteresis: Pinning of the contact line on a single defect. *Europhysics Letters*, 20:523–528, 1992.
- [77] H.N. Oğuz and A. Prosperetti. Dynamics of bubble growth and detachment from a needle. *Journal of Fluid Mechanics*, 257:111–145, 1993.
- [78] I.R. Peters, D. van der Meer, and J.M. Gordillo. Splash formation and droplet ejection after disc impact on a liquid surface. (under consideration for publication). 2012.
- [79] H. Schlichting. *Boundary-layer theory (orig. Grenzschicht-Theorie, 1951)*. McGraw-Hill, New York, USA, seventh edition, 1979.
- [80] L.E. Scriven. Dynamics of a fluid interface: Equation of motion for Newtonian surface fluids. *Chemical Engineering Science*, 12:98–108, 1960.
- [81] W.T. Shi, C.L. Goodridge, and D.P. Lathrop. Breaking waves: Bifurcations leading to a singular wave state. *Physical review E*, 56:4157–4161, 1997.
- [82] J.H. Snoeijer, J. Ziegler, B. Andreotti, M. Fermigier, and J. Eggers. Thick films of viscous fluid coating a plate withdrawn from a liquid reservoir. *Physical Review Letters*, 100:244502, 2008.
- [83] G. Stokes. On the theory of oscillatory waves. *Transactions of the Cambridge Philosophical Society*, 8:441–455, 1847.

- [84] Y. Tagawa, N. Oudalov, C.W. Visser, I.R. Peters, D. van der Meer, C. Sun, A. Prosperetti, and D. Lohse. Highly focused supersonic microjets. *arXiv:1112.2517v3*, 2012.
- [85] P.H. Taylor. The shape of the Draupner wave of 1 January 1995. 1995.
- [86] J.W. Turkey. An introduction to the calculations of numerical spectrum. *Spectral Analysis of Time Series*, pages 25–46, 1967.
- [87] F.T. Tsveter. Hamilton’s equations of motion for non-conservative systems. *Celestial Mechanics and Dynamical Astronomy*, 60:409–419, 1994.
- [88] Unknown. California geological survey (retrieved March 10, 2012), 2007.
- [89] L. van Wijngaarden. Voortgezette Stromingsleer, 1995.
- [90] D. Vella and L. Mahadevan. The cheerios effect. *American Journal of Physics*, 73:817–825, 2005.
- [91] A.L. Voges. *Free surface waves in a cylinder with a vibrating lateral side*. PhD thesis, Tshwane University of Technology, 2006.
- [92] G. von Winckel. *besselzero*, 2005.
- [93] G.B. Whitham. *Linear and nonlinear waves*. Wiley, New York, USA, 1974.
- [94] V.E. Zakharov. Stability of periodic waves of finite amplitude on the surface of a deep fluid. *Zhurnal Prikladnoi Mekhaniki i Tekhnicheskoi Fiziki*, 9:86–94, 1968.
- [95] B.W. Zeff, B. Kleber, J. Fineberg, and D.P. Lathrop. Singularity dynamics in curvature collapse and jet eruption on a fluid surface. *Nature*, 403:401–404, 2000.